

# Numerical Simulations of Black Hole Binaries with Unequal Masses

DISSERTATION

zur Erlangung des akademischen Grades  
doctor rerum naturalium (Dr. rer. nat.)



---

seit 1558

vorgelegt dem Rat der  
PHYSIKALISCH-ASTRONOMISCHEN FAKULTÄT  
der  
FRIEDRICH-SCHILLER-UNIVERSITÄT JENA

von Dipl.-Phys. Doreen Müller  
geboren am 31.05.1983 in Frankenberg/Sa.

Gutachter:

- 1.: Prof. Dr. Bernd Brüggemann, Friedrich–Schiller–Universität Jena
- 2.: Prof. Dr. Luciano Rezzolla, Albert Einstein Institut Golm
- 3.: Prof. Dr. Kostas Kokkotas, Eberhard Karls Universität Tübingen

Tag der Disputation: 11.07.2011

# Contents

<b>1</b>	<b>Introduction</b>	<b>1</b>
<b>2</b>	<b>Numerical Evolution of Einstein’s Equations</b>	<b>5</b>
2.1	3+1 Split of Einstein’s Equations and ADM Formulation . . . . .	5
2.2	The Evolution System . . . . .	8
2.3	Gauge Conditions . . . . .	10
2.3.1	The Slicing Condition . . . . .	10
2.3.2	The Shift Condition . . . . .	11
2.4	Extraction of Gravitational Waves . . . . .	13
2.4.1	The Newman–Penrose Formalism . . . . .	13
2.4.2	Calculating the Strain Waveform from the Weyl Scalar . . . . .	16
2.5	Physical Parameters of a Simulation . . . . .	20
2.6	Implementation in the BAM Code . . . . .	25
2.7	Convergence and Richardson Extrapolation . . . . .	26
<b>3</b>	<b>Initial Data for Black Hole Binaries</b>	<b>29</b>
3.1	Conformal Decomposition . . . . .	29
3.2	Bowen–York Extrinsic Curvature (Momentum Constraints) . . . . .	30
3.3	Punctures (Hamiltonian Constraint) . . . . .	32
3.4	Initial Data for Lapse and Shift . . . . .	34
3.5	Black Hole Binaries in Quasi–Circular Orbits . . . . .	35
3.5.1	Measuring Eccentricity . . . . .	36
3.5.2	Integrating post–Newtonian Equations of Motion . . . . .	38
3.5.3	Analytical Approach . . . . .	41
3.5.4	Results for non–Spinning Binaries . . . . .	43
3.5.5	Results for Spinning Binaries . . . . .	46

<b>4</b>	<b>Increasing the Mass Ratio in Finite Difference Simulations</b>	<b>51</b>
4.1	Increase in Computational Cost . . . . .	52
4.2	Gamma Driver Revisited . . . . .	53
4.3	Using the Conformal Factor for Dynamical Damping . . . . .	56
4.3.1	Adapted Damping in Single Black Hole Simulations . . . . .	58
4.3.2	Adapted Damping in Binary Simulations . . . . .	59
4.3.3	Behavior in Long-Term Simulations and Ameliorations . . . . .	63
4.4	Using Purely Analytical Formulas for Dynamical Damping . . . . .	66
4.4.1	Mass Ratio 4:1 . . . . .	67
<b>5</b>	<b>Highly Accurate Binary Black Hole Simulations</b>	<b>75</b>
5.1	Accuracy of Wave Extraction . . . . .	75
5.2	Simulations with Vanishing Total Spin . . . . .	80
5.3	Hybrid Waveforms and Phenomenological Templates . . . . .	85
<b>6</b>	<b>Summary and Future Prospects</b>	<b>95</b>
	<b>List of Publications</b>	<b>98</b>
	<b>List of Presentations</b>	<b>100</b>
	<b>Bibliography</b>	<b>103</b>
	<b>Abbreviations and Notation</b>	<b>117</b>
<b>A</b>	<b>Hamiltonian and Flux Function for Initial Data</b>	<b>121</b>
<b>B</b>	<b>Tetrad Construction for Gravitational Wave Extraction</b>	<b>127</b>
<b>C</b>	<b>Gravitational Wave Modes in Bitant Symmetry</b>	<b>129</b>
	<b>Ehrenwörtliche Erklärung</b>	<b>130</b>
	<b>Zusammenfassung</b>	<b>133</b>

# Acknowledgements

I would like to express my sincerest thanks to my advisor, Prof. B. Brügmann, for having given me the opportunity to work on one of the most exciting topics of physics, namely black holes, and for his inspiring support and teaching during the last years. I also want to thank my colleagues in the Numerical Relativity group at the TPI Jena, especially Marcus Thierfelder for sharing Pfannkuchen, many funny moments and deep thoughts, as well as Jason Grigsby, David Hilditch and Sebastiano Bernuzzi for their invaluable advices and an uncountable number of physics discussions, and my office mates Andreas Weyhausen and Roman Gold for giving me a great time.

In addition, I am grateful to Frank Ohme, Mark Hannam, Sascha Husa and Ulrich Sperhake for many discussions and exchanges.

Special thanks for proof reading (parts of) this manuscript go to Jason, David, my parents, my grandmother Monika, Heiko Gerdes, Agnes, Sebastian and Marcus.

I am deeply indebted to my parents, Simone and Steffen Müller, my grandparents and my sister, who endlessly support and encourage me. My beloved husband Sebastian always motivated and lived the ups and downs of this theses with me, and I will always be profoundly grateful for his encouragement.

Meinen Großeltern danke ich dafür, dass sie immer an mich glauben und mich in allem vorbehaltlos unterstützen und ermutigen.



# 1 Introduction

Understanding the processes happening on large scales in our Universe is one of the most exciting topics of theoretical physics today. Albert Einstein's theory of general relativity [1,2] has led to a large number of groundbreaking novel predictions, among them the existence of objects like black holes and the emission of gravitational waves whenever masses are accelerated.

The detection of gravitational waves will unveil a new and complementary source of information about the cosmos. In the case of the beginnings of the Universe, for example, we nowadays only have access to the cosmic microwave background, which provides information about the situation from about  $3 \times 10^5$  years after Big Bang. Nucleosynthesis studies can at least provide information about the situation a few minutes after the event, but with the detection of gravitational waves we could get as close as  $10^{-24}$  s to the Big Bang [3]. As they are not damped when passing through matter, gravitational waves would allow us to look behind clouds of gas right into the heart of a supernova explosion, and they permit to study in detail the merger of black holes and neutron stars.

The actual detection of gravitational waves still poses a variety of technical and theoretical challenges to be met. Since they are extremely weak, a detector's sensitivity needs to be sufficiently high to measure relative length changes of  $10^{-21}$  and below. The Earth based interferometric detectors [4–8] located all over the world have just entered or are on the verge of entering this regime of sensitivity. However, the ground based detectors' output is dominated by different types of noise [3], the most important influence being vibrations of the ground which obscure most of the expected gravitational wave signals. Therefore, theoretical predictions of signals are essential ingredients for the construction of waveform templates. The detector output is compared against these templates in order to extract signals from the noise (matched filtering). The planned space based Laser Interferometer Space Antenna (LISA) [9] and deci-hertz Interferometer Gravitational Wave Observatory (DECIGO) [10] will

not be affected by seismic noise and ground vibrations, but here accurate templates are necessary in order to estimate the parameters of the detected sources.

Among the most likely sources for the first detections are two compact objects orbiting each other, thereby emitting gravitational radiation such that their orbits circularize and shrink until they get very close, merge and form a single compact object which rings down to a stationary state. Such a scenario can, however, only be computed numerically because Einstein's equations are far too complex to be solved analytically, except for a few simple cases.

Inspiral and ringdown phase can be treated with approximation techniques. For large binary separations, the post-Newtonian (PN) approximation holds [11, 12] and the final object can be treated with perturbative methods [13]. The strong field regime during merger, however, has to be treated using means of Numerical Relativity (NR) simulations. The effective one-body method (EOB) [14] is an approach to a fully analytical description even during merger, but a calibration with numerically generated waveforms is still necessary in order to obtain highly accurate results.

NR waveforms are furthermore used to study and confirm the efficiency of existing detector search pipelines and data analysis tools. For the Numerical Injection Analysis (NINJA) project [15, 16], binary black hole (BBH) waveforms were injected into simulated detector noise, and data analysis groups worked on restoring the original NR waveform and estimating the underlying physical parameters. These examples show that numerical relativity has become an integral part of gravitational wave (GW) data analysis of today.

The present thesis focuses on the numerical calculation of gravitational waves emitted during the late inspiral, merger and ringdown of two black holes in vacuum, with particular emphasis on binaries with unequal masses. The first successful simulations of a black hole binary in quasi-circular orbits treated binaries with equal masses and without spins [17–19]. Because of the fact that such simple cases are astrophysically very rare, the range of parameters which can be studied within NR has been extended continuously since then. Regarding the masses, mergers of black holes with a moderate mass ratio  $q$  different from one are likely to occur in our Universe [20–22]. As a consequence, increasing the mass ratio in black hole binary simulations up to about 100:1 (yet higher mass ratios can be treated perturbatively [23, 24]) was one of the most urgent goals of the last few years. The tremendous increase in computational cost and the necessity to cope with a numerical instability arising during the



---

simulations had until recently [25] prevented this problem from being solved. In this thesis an approach to deal with the aforementioned instability is proposed, which additionally shows benefit regarding the computational cost of a simulation.

A brief introduction to the basics of numerical relativity including the set of equations to be solved and techniques of extraction of physically relevant information from black hole binary simulations is given in chapter 2. Some fundamental properties of the computer code BAM which is used in this thesis are also discussed in that chapter.

Dealing with a set of evolution equations, we first need to specify initial data as a starting point for numerical evolutions. Chapter 3 introduces our approach to generating initial parameters for black holes which eventually lead to a quasi-circular inspiral along orbits with only little remaining eccentricity. In this chapter the eccentricity measurement for different mass ratios and spins is carried out in order to demonstrate the fruitfulness of the proposed approach even for cases where the mass ratio is up to 10:1, and we compare to other methods in the literature.

Having initial data for binaries with unequal masses at hand the question how to successfully evolve those is addressed in chapter 4. The implications of increasing the mass ratio for the computational cost are investigated and the equation governing one of the gauge quantities in the theory is examined. Novel formulations for a damping parameter are suggested and analyzed. The method presented in that chapter has meanwhile been seized and developed further by two other groups and their suggestions are discussed briefly as well.

Finally, it is studied in chapter 5 how the accuracy of gravitational waves extracted from numerical codes can be increased by modifications of the grid structure, keeping the computational cost relatively low. Furthermore, the use of such very accurate numerical waveforms in the production of waveform templates for gravitational wave data analysis is discussed. Different physical cases, including spinning binaries, are used to calibrate a phenomenological waveform model, and the usability for gravitational wave detection is demonstrated.

The results are summarized and discussed with regard to future improvements in chapter 6.

Abbreviations used in this thesis are listed on page 119 and an overview over the scientific notation can be found on page 120.



# 2 Numerical Evolution of Einstein's Equations

The following chapter briefly reviews the tools needed for numerical simulations and analysis of black hole binary spacetimes. First, Einstein's equations will be written in a form suitable for numerical evolutions. Furthermore, the process of measuring the gravitational waves which are emitted during evolution will be demonstrated, and the question how to calculate global properties like mass and momentum of a spacetime will be treated. Lastly, some of the most important properties of the code used in this thesis will be summarized.

## 2.1 3+1 Split of Einstein's Equations and ADM Formulation

In general relativity, we are working on a spacetime, i.e. a four dimensional, globally hyperbolic, oriented and time oriented Lorentzian manifold  $\mathcal{M}$ . In particular, this means that we have a two times covariant, non-degenerate, symmetric metric tensor  $g$  with signature  $(-, +, +, +)$ . The field equations relating the geometry of the spacetime to the distribution of mass and energy in it are the Einstein equations,

$$R_{\mu\nu} - \frac{1}{2}g_{\mu\nu}R = 8\pi T_{\mu\nu}. \quad (2.1)$$

Greek indices run from 0 to 3 throughout this thesis and we will use geometric units in which the gravitational constant and the speed of light are set to one,  $G = c = 1$ , unless stated otherwise. In the above equation, the Ricci curvature tensor  $R_{\mu\nu}$  is obtained from the Riemann tensor by contraction,  $R_{\mu\nu} = R^{\lambda}_{\mu\lambda\nu}$ , and we use the Einstein summation convention. The Riemann tensor can be constructed from  $R^{\alpha}_{\beta\mu\nu} = \partial_{\mu}\Gamma^{\alpha}_{\beta\nu} - \partial_{\nu}\Gamma^{\alpha}_{\beta\mu} + \Gamma^{\alpha}_{\rho\mu}\Gamma^{\rho}_{\beta\nu} - \Gamma^{\alpha}_{\rho\nu}\Gamma^{\rho}_{\beta\mu}$  using the Christoffel symbols

$\Gamma_{\mu\nu}^\alpha = \frac{1}{2}g^{\alpha\rho}(\partial_\mu g_{\rho\nu} + \partial_\nu g_{\rho\mu} - \partial_\rho g_{\mu\nu})$ . On the right hand side (RHS) of Eq. (2.1),  $T_{\mu\nu}$  is the stress–energy tensor and vanishes in spacetimes without matter, like those we consider in this thesis. Therefore, for black hole spacetimes, the equations to be solved can be written as

$$R_{\mu\nu} = 0. \quad (2.2)$$

In an arbitrary coordinate system, these are ten coupled, non–linear second order differential equations to be solved for the components of the metric tensor,  $g_{\mu\nu}$ .

Equations (2.2) are written in a fully covariant way. Because we want to study the time evolution of certain systems, we first need to find a way to introduce a time coordinate. Then we want to write Eq. (2.2) as a Cauchy problem. This is done by a foliation of spacetime known as 3+1 split [26, 27].

Spacetime is separated into 3–dimensional slices which are spacelike everywhere. The slices are the level sets of some scalar field  $t$  on  $\mathcal{M}$  ( $t = \text{const.}$  marks one spatial slice). Now it is possible to construct the (timelike) unit normal vector to each spacelike slice,

$$n^\nu = -\alpha\nabla^\nu t, \quad (2.3)$$

with the scale factor  $\alpha = [-(\nabla^\nu t)(\nabla_\nu t)]^{-1/2}$ , known as the lapse function, and the covariant derivative  $\nabla_\mu$  associated with the spacetime metric  $g_{\mu\nu}$ . By the definition just introduced, the lapse is always positive. In numerical simulations, however, it might become negative, but this is problematic since the spatial slices might then intersect themselves and the notion of time becomes non–unique. From the normal vector, we can construct the projection operator  $P^\nu_\mu = \delta^\nu_\mu + n^\nu n_\mu$  and project the spacetime metric onto the spatial slices. Doing this, we obtain the induced metric

$$\gamma_{\mu\nu} = g_{\mu\nu} + n_\mu n_\nu. \quad (2.4)$$

The induced metric now describes the intrinsic geometry of the hypersurface. Furthermore, we can construct the extrinsic curvature of a spatial slice which describes how the slice is embedded in spacetime by looking at how its normal vector changes when it is parallel transported along the slice,

$$K_{\mu\nu} = -P^\alpha_\mu \nabla_\alpha n_\nu. \quad (2.5)$$

Both  $\gamma_{\mu\nu}$  and  $K_{\mu\nu}$  are symmetric tensors. When moving from one hypersurface to

the next one along the normal direction, the spatial coordinates change according to  $x_{t+dt}^i = x_t^i - \beta^i dt$  with the shift vector  $\beta^\mu$ .

In the following, we will only work in coordinate systems adapted to the foliation. That means we will have  $\beta^0 = 0$  and  $\gamma_{0\mu} = 0$ , and we will therefore only consider the spatial parts of these objects. Also, the Lie derivative along the time vector  $t^\mu = \alpha n^\mu + \beta^\mu$  reduces to the partial derivative along time coordinate given by the scalar field  $t$ ,  $\mathcal{L}_{\vec{t}} = \partial_t$ . Finally, we find that the evolution of the induced metric is now related to the spatial components  $K_{ij}$  of the extrinsic curvature through

$$\partial_t \gamma_{ij} - \mathcal{L}_{\vec{\beta}} \gamma_{ij} = -2\alpha K_{ij}. \quad (2.6)$$

$\mathcal{L}_{\vec{\beta}}$  is the Lie derivative along the shift vector. Now, evolution equations for  $K_{ij}$  need to be found, too, but we will not have to consider time components  $K_{0\mu}$  of the extrinsic curvature in the following. The Einstein equations are rewritten in 3+1 form by contracting Eq. (2.2) with the normal vector and projecting onto the spatial hypersurfaces with the projection operator  $P^\nu_\mu$ . This procedure results in evolution equations for the six independent components of the extrinsic curvature,

$$\partial_t K_{ij} - \mathcal{L}_{\vec{\beta}} K_{ij} = -D_i D_j \alpha + \alpha \left( {}^{(3)}R_{ij} + K K_{ij} - 2K_{ik} K^k_j \right), \quad (2.7)$$

known as the Arnowitt–Deser–Misner (ADM) equations. Here, we have used  ${}^{(3)}R_{ij}$  to denote the Ricci tensor constructed from the induced metric  $\gamma_{ij}$ ,  $K = \gamma_{ij} K^{ij}$  is the trace of the extrinsic curvature and  $D_j$  is the 3-dimensional covariant derivative associated with the induced metric  $\gamma_{ij}$ . Furthermore, we obtain four constraint equations which do not contain any time derivatives. The Hamiltonian constraint reads

$${}^{(3)}R + K^2 - K_{ij} K^{ij} = 0 \quad (2.8)$$

with  ${}^{(3)}R = {}^{(3)}R_{ij} \gamma^{ij}$  the trace of the 3-dimensional Ricci tensor. The momentum constraints turn out to be

$$D_j (K^{ij} - \gamma^{ij} K) = 0. \quad (2.9)$$

Equations (2.8) and (2.9) are coupled through the trace of the extrinsic curvature,  $K$ . Analytically, if the constraint equations have been solved once (e.g. on the initial hypersurface  $t = 0$ ), the solution to the evolution equations will be solutions

of the constraints at all times. While this is true in the continuum limit, numerical relativity requires a discretization which negates this property. The BAM code uses a free evolution scheme in which the constraint equations are solved only on the initial hypersurface at  $t = 0$ . During the evolution the constraints are monitored, and based on how much they differ from zero we can judge how well our numerical solution solves the Einstein equations.

At this point, evolution equations for the lapse  $\alpha$  and the shift  $\beta^i$  are still missing. This is due to the coordinate freedom in general relativity. Lapse and shift are four gauge functions that can be chosen freely. For numerical relativity, however, we are interested in an evolution system that leads to stable simulations. For the evolution system Eqns. (2.6) and (2.7), no gauge has yet been found which makes the whole system of evolution equations strongly hyperbolic, and therefore, simulations using the ADM equations are not stable in general.

The next section therefore deals with a reformulation of Eqns. (2.6) and (2.7) which, together with the gauge conditions discussed in Sec. 2.3, form a system of strongly hyperbolic evolution equations. This leads to a well-posed initial value problem, i.e. the solution to the equations depends continuously on the given initial data.

## 2.2 The Evolution System

In the Baumgarte–Shapiro–Shibata–Nakamura (BSSN) reformulation of the evolution equations derived in the last section, a conformal metric  $\tilde{\gamma}_{ij}$  is introduced by rescaling the spatial metric  $\gamma_{ij}$  with a strictly positive scalar density  $\psi$ ,

$$\tilde{\gamma}_{ij} = \psi^{-4} \gamma_{ij}. \quad (2.10)$$

The conformal factor  $\psi$  is chosen such that the conformal metric has unit determinant,

$$\psi = \gamma^{\frac{1}{12}}, \quad (2.11)$$

where  $\gamma$  is the determinant of the 3-metric  $\gamma_{ij}$ .

The trace  $K$  of the extrinsic curvature and its tracefree part  $A_{ij} = K_{ij} - \frac{1}{3}\gamma_{ij}K$  are treated separately. The tracefree part is conformally rescaled, too, and we obtain  $\tilde{A}_{ij} = \psi^{-4}A_{ij}$ . The indices of conformal quantities like  $\tilde{A}_{ij}$  are raised and lowered

using the conformal metric. We therefore have  $\tilde{A}^{ij} = \psi^4 A^{ij}$ .

Now three new variables, the conformal connection functions, can be introduced via

$$\tilde{\Gamma}^i = \tilde{\gamma}^{jk} \tilde{\Gamma}_{jk}^i. \quad (2.12)$$

Here, the Christoffel symbols  $\tilde{\Gamma}_{jk}^i$  are those associated with the conformal metric. Because the determinant of the latter is one, Eq. (2.12) can be written as  $\tilde{\Gamma}^i = -\partial_j \tilde{\gamma}^{ij}$ . The evolution variables now are the conformal factor, the conformal metric, the conformal tracefree part and the trace of the extrinsic curvature, and the conformal connection functions.

In the analytically known Schwarzschild solution the conformal factor has a  $1/r$  singularity near the black hole sitting at  $r = 0$ . For this reason,  $\psi$  is expected to diverge at the positions of black holes in general solutions, too. This knowledge is used in the construction of initial data we employ (see chapter 3), and we will therefore replace the conformal factor  $\psi$  by  $\chi := \psi^{-4}$  as suggested by [18].  $\chi$  vanishes at the position of a black hole. We can thus evolve the full conformal factor  $\chi$  without the need to treat any singular part differently. This is one essential part of the moving puncture method [18, 19] we employ for binary black hole spacetimes.

The following equations are used to evolve the quantities  $\chi$ ,  $\tilde{\gamma}_{ij}$ ,  $\tilde{A}_{ij}$ ,  $K$  and  $\tilde{\Gamma}^i$ . They form the BSSN evolution system in vacuum [28, 29],

$$(\partial_t - \mathcal{L}_{\tilde{\beta}}) \tilde{\gamma}_{ij} = -2\alpha \tilde{A}_{ij}, \quad (2.13)$$

$$(\partial_t - \mathcal{L}_{\tilde{\beta}}) \tilde{A}_{ij} = \chi [-D_i D_j \alpha + \alpha R_{ij}]^{\text{TF}} + \alpha \left( K \tilde{A}_{ij} - 2\tilde{A}_{ik} \tilde{A}^k_j \right), \quad (2.14)$$

$$(\partial_t - \mathcal{L}_{\tilde{\beta}}) K = -D^i D_i \alpha + \alpha (\tilde{A}_{ij} \tilde{A}^{ij} + \frac{1}{3} K^2), \quad (2.15)$$

$$\begin{aligned} (\partial_t - \mathcal{L}_{\tilde{\beta}}) \tilde{\Gamma}^i &= \tilde{\gamma}^{jk} \partial_j \partial_k \beta^i + \frac{1}{3} \tilde{\gamma}^{ij} \partial_j \partial_k \beta^k - 2\tilde{A}^{ij} \partial_j \alpha \\ &+ 2\alpha \left( \tilde{\Gamma}_{jk}^i \tilde{A}^{jk} - \frac{6}{4\chi} \tilde{A}^{ij} \partial_j \chi - \frac{2}{3} \tilde{\gamma}^{ij} \partial_j K \right), \end{aligned} \quad (2.16)$$

$$(\partial_t - \mathcal{L}_{\tilde{\beta}}) \chi = \frac{2}{3} \chi (\alpha K - \partial_j \beta^j). \quad (2.17)$$

The label ‘‘TF’’ refers to the tracefree part of the expression in brackets. Care has to be taken at points where the conformal factor  $\chi$  vanishes in order to avoid divisions by zero in the RHS of Eq. (2.16). In practice,  $\chi$  is replaced by some positive number  $\delta_\chi$  whenever it falls below that value. This way, unphysical negative values in the

conformal factor, which might occur during the course of the numerical calculations, are avoided, too.

The success of the evolution system (2.13) – (2.17) is due to the fact that using the  $\tilde{\Gamma}^i$  as independent variables and substituting the divergence of  $\tilde{A}^{ij}$  by the momentum constraint (Eq. (2.9)) in its evolution equation turns the system into a strongly hyperbolic one when it is used in conjunction with 1+log slicing (Eq. (2.18)) and the Gamma driver condition (Eq. (2.19)) discussed in the next chapter [30,31].

There are many other formulations of the Einstein equations available today, see e.g. [32,33] for the Bona–Massó formulation, [34–37] for the Z4(c) formulation and [38] for an overview over additional formulations using a 3+1 split. An also very successful reformulation which, however, is not based on a 3+1 split, is the Generalized Harmonics Formulation [17,39–41].

## 2.3 Gauge Conditions

Einstein's equations allow us to freely choose a coordinate system. In a 3+1 split this freedom amounts to choosing the lapse function  $\alpha$  as well as the shift vector  $\beta^i$ . Ideally, the coordinate system we pick reflects the underlying symmetry of the physical configuration under consideration and allows us to deal with the physical singularity inside the black hole(s) on the numerical grid.

### 2.3.1 The Slicing Condition

The choice of lapse function  $\alpha$  governs how the spacetime is decomposed into spatial hypersurfaces and how these evolve in (coordinate) time. A first option consists in simply taking  $\alpha = 1$  which is known as geodesic slicing [42]. Unfortunately, in the case of a single Schwarzschild black hole, the slices constructed this way hit the physical singularity in finite coordinate time (after  $t = \pi M$ ) and lead to a failure of the numerical code. For this reason, in general, geodesic slicing cannot be used for stable evolutions of black hole spacetimes. The construction of a slicing condition which avoids the singularity leads to maximal slicing [43]. Here, the extrinsic curvature  $K$  is set to zero, and its time derivative  $\partial_t K$  is required to vanish, too. These conditions lead to an elliptic equation on the lapse which has to be solved at every single time step during the evolution. Much more computer time will thus be spent on the



solution of the slicing condition instead of on solving the evolution equations.

A family of slicing conditions which are computationally cheaper to solve is the Bona–Massó family [32, 33] where  $\partial_0\alpha = -\alpha^2 f(\alpha)K$  with some positive function  $f(\alpha)$  and  $\partial_0 = \partial_t - \beta^i \partial_i$ . Here, instead of an elliptic equation, an evolution equation for the lapse has to be solved. For the simulations presented in this thesis we use  $f(\alpha) = 2/\alpha$ , suggested by [44, 45], which is called 1+log slicing,

$$\partial_0\alpha = -2\alpha K. \quad (2.18)$$

For this choice, the slicing is strongly singularity avoiding, i.e. if a singularity forms in a certain region of spacetime, the lapse collapses to zero in that region a finite coordinate time before the spatial slices reach the singularity. This way, the slices stop advancing around the singularity and never reach it. The wave speed associated with  $\alpha$  from Eq. (2.18) is  $v_\alpha = \sqrt{2\alpha}$ . We will find this speed in the discussion of Sec. 4.3.3.

Numerical simulations of black holes face a problem related to the slicing condition which is known as slice stretching. There are two phenomena in this context. Because of the presence of a black hole, coordinate lines near the horizon are attracted and sucked into the black hole. This leads to a differential infall of grid points into it. The second effect is caused by the choice of a singularity avoiding slicing condition in which the slices stop advancing near a forming singularity (where the lapse is zero) but continue to evolve in the rest of the domain and therefore “wrap” around the region of the singularity, see e.g. [46, 47]. These influences show their effect in large metric gradients near the throat of a black hole. For some time the method of choice to handle slice stretching (and in general problems associated with the singularity inside a black hole horizon) was considered to be excision, where the interior of the black hole was cut out of the numerical domain [48–50], and an appropriate choice of the shift vector. That method was mostly superseded by the method of moving punctures with the use of special shift conditions which will be discussed in the next section.

### 2.3.2 The Shift Condition

In simulations of black hole spacetimes, the three spatial components of the shift vector  $\beta^i$  have to be set properly in order to allow for long term stability. Using a

vanishing shift,  $\beta^i = 0$ , does not work well when evolving black holes. The reason is the development of slice stretching as discussed at the end of the last section. In particular, the differential infall of coordinate observers means that the black hole horizon grows on the numerical grid leaving fewer and fewer grid points in the region outside the hole. To counteract this behavior, a non-vanishing, outwards pointing shift can be used which will drag grid points and prevent them from falling into the black hole.

As in the case of first slicing conditions, the first shift conditions constituted elliptic equations. Examples are the minimal strain and the minimal distortion condition [51, 52] or a modification of the latter, the Gamma freezing condition [53]. The fact that three coupled elliptic equations for the three shift components have to be solved at every time step renders these conditions unattractive for use in numerical simulations.

Inspired by BALAKRISHNA *et al.* who proposed the first minimal distortion driver conditions [54], ALCUBIERRE *et al.* [44, 45, 53] developed the first Gamma-driver condition. The principle is, similar to what has been done for the lapse, to turn the above mentioned elliptic equations into hyperbolic ones and evolve them in coordinate time.

The Gamma-driver version most widely used today in conjunction with the BSSN evolution system Eqns. (2.13)–(2.17) is

$$\partial_0^2 \beta^i = \frac{3}{4} \partial_0 \tilde{\Gamma}^i - \eta \partial_0 \beta^i. \quad (2.19)$$

In this condition,  $\eta$  is the damping term which will be discussed in detail in Sec. 4.2. Generalizations of this equation have been proposed e.g. in [55, 56]. It has been discussed if the advection term  $\beta^i \partial_i$  is necessary in Eq. (2.19) or if it can be dropped. The authors of [57] show analytically (in the context of the BSSN formulation) that modes with propagation speed zero are suppressed when the advection term is included. In [58, 59] it is shown that the BSSN system used with the gauges Eq. (2.18) and Eq. (2.19) is strongly hyperbolic, and we therefore include this term.

The Gamma-driver shift succeeds in what is necessary to avoid the severe implications of singularity avoidance: when the slices start to stretch, the shift vector counteracts by pulling out grid points from the region near the black hole. The gauge conditions (2.18) and (2.19) are also symmetry seeking. If the spacetime pos-

sesses a timelike Killing vector  $\vec{\xi}$ , then the time coordinate  $t$  becomes adapted to it such that the Killing equation  $\mathcal{L}_{\vec{\xi}}g_{\mu\nu} = 0$  reduces to  $\partial_t g_{\mu\nu} = 0$ , and the components of the metric tensor become time independent. This is the case in simulations of orbiting black holes which after coalescence settle down to a single (spinning) black hole producing a stationary spacetime. Therefore the second part of slice stretching related to time marching on outside a black holes but freezing inside does not harm our simulations any more when the metric ceases to depend on time.

## 2.4 Extraction of Gravitational Waves

### 2.4.1 The Newman–Penrose Formalism

Far away from gravitational sources, the metric can be approximated by a perturbation on a flat space background. In this weak field approximation, the metric can be written as

$$g_{\mu\nu} = \eta_{\mu\nu} + h_{\mu\nu} \quad (2.20)$$

with  $\eta_{\mu\nu}$  the metric of Minkowski spacetime and  $h_{\mu\nu}$  a small perturbation,  $|h_{\mu\nu}| \ll 1$  (see e.g. [60] or other standard text books on general relativity). In the following, Cartesian coordinates will be used where  $\eta_{\mu\nu} = \text{diag}(-1, 1, 1, 1)$ . Now, the Einstein equations can be rewritten in terms of the perturbation  $h_{\mu\nu}$ . For vacuum spacetimes and in the Lorentz gauge  $\nabla_{\mu}h^{\mu\nu} = 0$ , this amounts to solving a wave equation on  $h_{\mu\nu}$  in flat space with solution

$$h_{\mu\nu} = a_{\mu\nu} \exp(ik_{\rho}x^{\rho}). \quad (2.21)$$

Here,  $a_{\mu\nu}$  is the amplitude and  $k^{\mu}$  the propagation vector of the gravitational wave. The wave equation itself implies that the propagation vector is null,  $k_{\rho}k^{\rho} = 0$ , and gravitational waves therefore propagate at the speed of light. From the Lorentz gauge we find that the waves are transverse,  $a^{\mu\rho}k_{\rho} = 0$ . Using all the gauge freedom, we adopt the transverse–traceless (TT) gauge and an appropriate Lorentz frame. These choices reduce the number of independent components of  $a_{\mu\nu}$  to only two which we label  $h^{+}$  and  $h^{\times}$ . If the direction of propagation of the wave is the  $z$ -direction, we obtain  $a_{xx} = h^{+}$ ,  $a_{xy} = h^{\times}$ ,  $a_{yx} = a_{xy}$ ,  $a_{yy} = -a_{xx}$  and  $a_{\alpha\beta} = 0$  for all other  $\alpha, \beta$ . It

is common to write the metric perturbation tensor in the gauge described above as

$$h_{ij}^{\text{TT}} = h^+ e_{ij}^+ + h^\times e_{ij}^\times, \quad (2.22)$$

with the polarization tensors  $e_{ij}^{+,\times}$  which obey  $e_{xx}^+ = -e_{yy}^+ = 1$ ,  $e_{xy}^\times = e_{yx}^\times = 1$ , and all other components vanish. In summary, the wave amplitude is purely spatial, perpendicular to the direction of propagation, and there are two independent polarizations,  $h^+$  (when  $h^\times = 0$ ) and  $h^\times$  (when  $h^+ = 0$ ). A gravitational wave passing through two freely falling particles will change their proper distance  $l$ , with the strain  $\Delta l/l$  proportional to the GW amplitude.

The BAM code extracts gravitational waves via the Weyl scalar  $\Psi_4$  computed in the Newman–Penrose formalism. Details of this procedure can be found in [61]. This quantity is defined by

$$\Psi_4 = -C_{\alpha\beta\gamma\delta} k^\alpha \bar{m}^\beta k^\gamma \bar{m}^\delta, \quad (2.23)$$

with  $C_{\alpha\beta\gamma\delta}$  the Weyl tensor and  $k^\mu$  and  $m^\mu$  two vectors of a tetrad of null vectors  $\{l^\mu, k^\mu, m^\mu, \bar{m}^\mu\}$ . In vacuum spacetimes, the Weyl tensor coincides with the Riemann tensor,  $C_{\alpha\beta\gamma\delta} = R_{\alpha\beta\gamma\delta}$ . It can be shown (see e.g. [38]) that in the linearized theory, adapting the TT gauge and when the spatial coordinates are the standard spherical coordinates  $\{r, \theta, \phi\}$ ,  $\Psi_4$  corresponds to an outgoing wave and is related to the GW strain  $h = h^+ - ih^\times$  by a second time derivative,

$$\Psi_4(t) = \frac{d^2}{dt^2} h(t). \quad (2.24)$$

In order to calculate  $\Psi_4$  numerically, we need to express Eq. (2.23) in terms of 3+1 quantities. Using the special null tetrad given in Eqns. (B.1)–(B.4), we obtain

$$\Psi_4 = -\frac{1}{2} (\perp R_{abcd} v^a v^c - 2 \perp R_{abcd} n^\alpha v^c + \perp R_{\alpha b \gamma d} n^\alpha n^\gamma) \bar{m}^b \bar{m}^d \quad (2.25)$$

with

$$\begin{aligned} \perp R_{abcd} &= P_a^\mu P_b^\nu P_c^\gamma P_d^\delta R_{\mu\nu\gamma\delta} = {}^{(3)}R_{abcd} + K_{ac} K_{bd} - K_{ad} K_{bc}, \\ \perp R_{abcd} n^\alpha &= P_b^\beta P_c^\gamma P_d^\delta R_{\alpha\beta\gamma\delta} n^\alpha = D_c K_{db} - D_d K_{cb}, \\ \perp R_{\alpha b \gamma d} n^\alpha n^\gamma &= P_b^\beta P_d^\delta R_{\alpha\beta\gamma\delta} n^\alpha n^\gamma = {}^{(3)}R_{bd} + K K_{bd} - K^\mu{}_d K_{b\mu}. \end{aligned}$$

The spatial vector  $v^i$  is given in Appendix B and  $n^\mu$  is the normal vector to the spatial hypersurfaces as introduced in Eq. (2.3). The code computes expression (2.25) on the entire grid and interpolates its values to certain extraction radii  $R_{\text{ex}}$ . Care has to be taken when using this procedure because  $\Psi_4$  only asymptotically corresponds to outgoing radiation far away from the sources. From the peeling theorem we know that the asymptotic behavior of  $\Psi_4$  at large distances is  $\Psi_4 \sim 1/r$  [62]. For this reason, we can use different extraction radii  $R_{\text{ex},1} \dots R_{\text{ex},k}$  (typically  $k = 5$ ) and extrapolate to infinite extraction radius using a  $1/r$  fit to the computed values. In practice it has been found that the error in  $R_{\text{ex}}\Psi_4$  falls off as  $1/R_{\text{ex}}$  [63], and even the next term proportional to  $1/R_{\text{ex}}^2$  may be significant [64]. The difference in the fits including only the first term or the second term, too, is therefore used to estimate the error in the extrapolation.

Under rotations of the null tetrad which leave  $l^\mu$  and  $k^\mu$  invariant and rotate  $m^\mu$  and  $\bar{m}^\mu$  by some angle  $\theta$ ,  $\Psi_4$  transforms into  $e^{-2i\theta}\Psi_4$  and therefore has spin-weight  $-2$ . We can thus decompose it using spin-weighted spherical harmonics with spin weight  $-2$ ,  ${}_{-2}Y_{lm}$ , as basis functions (see [65] or [38] for a definition) and obtain the multipoles  $\Psi_4^{lm}$  through the scalar product,

$$\Psi_4^{lm}(t) = ({}_{-2}Y_{lm}, \Psi_4) = \int_0^{2\pi} \int_0^\pi \sin\theta \, d\theta \, d\varphi \overline{{}_{-2}Y_{lm}(\theta, \varphi)} \Psi_4(t, \theta, \varphi), \quad (2.26)$$

where  $\Psi_4$  has been calculated at extraction radius  $R_{\text{ex}}$ , and we have  $l \geq |s| = 2$  and  $-l \leq m \leq l$ . We further split  $\Psi_4^{lm}$  into mode amplitude  $A_{lm}$  and phase  $\phi_{lm}$  in order to cleanly separate effects in these components,

$$R_{\text{ex}}\Psi_4^{lm} = A_{lm}e^{i\phi_{lm}}. \quad (2.27)$$

For two black holes in a quasi-circular orbit, the lowest non-vanishing modes are those with  $l = 2, |m| = 2$ . Because of the symmetries of the spin-weighted spherical harmonics and  $\Psi_4$  we find  $\Psi_4^{2,m} = \overline{\Psi_4^{2,-m}}$  (cf. Eq. (C.6)). It is therefore sufficient to consider the  $l = 2, m = 2$  mode when talking about the most dominant modes for the cases studied in this thesis.

The amplitude of a gravitational wave emitted by a black hole binary in quasi-circular orbit increases continuously up to merger. Afterwards it falls down rapidly

as the final black hole rings to a stationary state. We can use this peak in the amplitude as a measure of the merger time in numerical simulations.

### 2.4.2 Calculating the Strain Waveform from the Weyl Scalar

As mentioned before, a gravitational wave detector measures the strain proportional to the relative length change in the detector arms,  $h \sim \Delta l/l$ . As described in the previous section, the numerical code extracts the Weyl scalar  $\psi_4$  which is related to the strain by Eq. (2.24). Analytically, the strain can be obtained from the Weyl scalar from two indefinite integrations in time. In practice, however, we have to deal with a discretely sampled time series of finite length. We therefore numerically compute

$$h_0(t) = \int_0^t dt' \int_0^{t'} dt'' \Psi_4(t'') \quad (2.28)$$

from the numerical data and write the strain as

$$h(t) = h_0(t) + C_1 t + C_0, \quad (2.29)$$

with the constants  $C_0 = h(0)$  and  $C_1 = \frac{dh}{dt}(0)$ . Since our numerically computed  $\psi_4$  does not contain values for  $t < 0$ , we can not estimate the values of  $C_0$  and  $C_1$  from the data. Simply setting them to zero means neglecting the signal at earlier times, which is unphysical. An additional difficulty arises from numerical noise in the data being amplified when the integrals in Eq. (2.28) are performed, as argued by [66]. It has been found empirically that simply calculating the integrals as given in Eq. (2.28), without additional care for the constants  $C_0$  and  $C_1$ , and for the amplification of noise, the resulting components  $h^+$  and  $h^\times$  show non-linear drifts instead of oscillating around zero, an effect which is demonstrated in Fig. 2.1. In the literature, there is an ongoing discussion of methods suitable to produce clean strain waveforms from numerical  $\psi_4$  data. In this section, some of these methods will be revised and compared to each other in order to determine the one which inhibits least ambiguity and gives the cleanest strain waveforms. As an example waveform, the 22-mode of a black hole binary with mass ratio  $q = 4$  and initial separation  $D = 10 M$ , computed at extraction radius  $R_{\text{ex}} = 90 M$  is employed. The resulting components of the strain waveform will be denoted by  $h_{22}^+$  and  $h_{22}^\times$ . All the results shown in the figures of this chapter

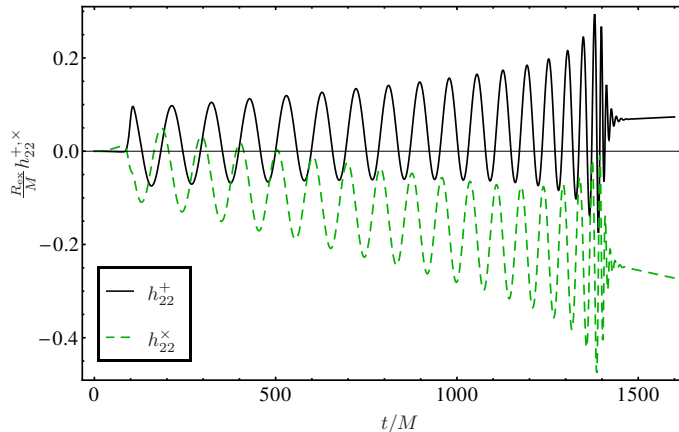


**Figure 2.1:** Real (black line) and (negative of the) imaginary part (green dashed line) of the 22–mode of the strain  $h$  for a binary with mass ratio  $q = 4$  and initial separation  $D = 10 M$  extracted at  $R_{\text{ex}} = 90 M$ . The 22–mode of  $\psi_4$  has been integrated twice in time but no integration constants have been chosen, and the drift of the metric waveform  $h_{22}$  can be clearly seen.

were obtained using this waveform. It was originally presented in [DM4] where a detailed error analysis and comparison to PN models was carried out. In [DM6], this waveform was compared to the result from the independent numerical code LEAN [67], and again compared with PN waveforms, which complements the work in [DM4] by additionally extrapolating the wave to infinite extraction radius, see also Sec. 5.3.

**Integration in time domain:** The waveforms in Fig. 2.1 suggest that the drift we find is exactly what we expect from Eq. (2.28) and subtracting a linear fit to the raw integration data  $h_0$  might result in a clean  $h$  oscillating around zero [68]. The outcome of this procedure is plotted in the left panel of Fig. 2.2. Along with the strain components  $h_{22}^+(t)$  and  $h_{22}^\times(t)$ , the figure shows the amplitude of  $h_{22}(t)$ ,  $|h_{22}| = \sqrt{(h_{22}^+)^2 + (h_{22}^\times)^2}$ , as a green line. From a binary black hole inspiral, we expect to see a monotonically growing amplitude up to merger and an exponential fall-off after it. In practice, we find a small but non-negligible oscillation of the amplitude which moreover does not vanish at later times. If these oscillations were to arise from physical eccentricity in the initial data, they would decrease in amplitude because the binary circularizes during inspiral. Since this is not the case, the oscillations arise from the yet not optimal integration procedure. As a further indication we note that the amplitude does also not fall to zero after ringdown, but seems to slightly increase again after  $t \simeq 1500 M$ , which is a clear sign of unphysical effects. The authors of [66] have shown clearly that high-frequency noise in the numerical data

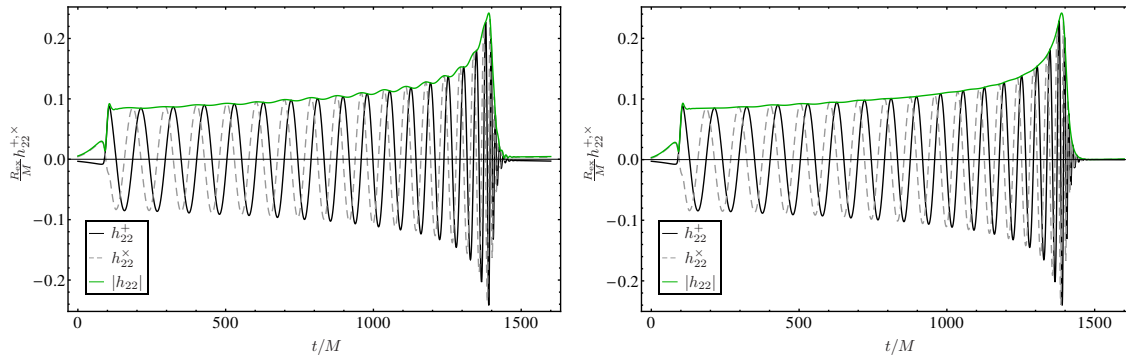


**Figure 2.2:** Real (black line) and (negative of the) imaginary part (gray dashed line) of the 22–mode of the strain  $h$  as well as its amplitude  $|h_{22}| = \sqrt{(h_{22}^+)^2 + (h_{22}^\times)^2}$  (green line) for a binary with mass ratio  $q = 4$  and initial separation  $D = 10 M$  extracted at  $R_{\text{ex}} = 90 M$ .

*Left panel:* The integration constants have been chosen by linear fits to the metric waveform components shown in Fig. 2.1. Now  $h_{22}^+$  and  $h_{22}^\times$  oscillate around zero. The amplitude  $|h_{22}|$  still shows some oscillation at late times, however, indicating that the integration constants are not optimal, yet. *Right panel:* Subtracting a cubic fit from the metric waveforms in Fig. 2.1 results in a much cleaner amplitude of the strain with oscillations reduced to a minimum. Additionally, the amplitude levels off at zero after ringdown as expected after a BBH merger.

can lead to non–linear drifts of the second time integration of  $\psi_4(t)$ . Indeed, instead of subtracting a linear fit from  $h_0(t)$ , we can repeat the procedure with higher order polynomial fits. In the right panel of Fig. 2.2, a cubic polynomial is fit to and subtracted from  $h_0(t)$  and in comparison with the left panel of the same figure, we see a clear improvement in the amplitude of  $h_{22}(t)$  (green line). The oscillations are reduced to a minimum. Subtracting higher order polynomials has been suggested in [69] and e.g. used in [70, 71].

**Integration in frequency domain:** The problems related to choosing the integration constants  $C_0$  and  $C_1$  can be bypassed by an integration in Fourier domain as suggested by [72]. If the Fourier transformation of some function  $f(t)$  is

$$\tilde{f}(\omega) = \frac{1}{\sqrt{2\pi}} \int dt f(t) \exp(-i\omega t), \quad (2.30)$$

where  $\omega$  is the frequency, the double time integral is performed by a division by  $\omega^2$ , and we find

$$\tilde{h}(\omega) = -\frac{\tilde{\Psi}_4(\omega)}{\omega^2}. \quad (2.31)$$

The time domain signal  $h(t)$  can be obtained by a Fourier back–transformation of  $\tilde{h}(\omega)$ . This method is, however, also not trivial because of the finite length of the



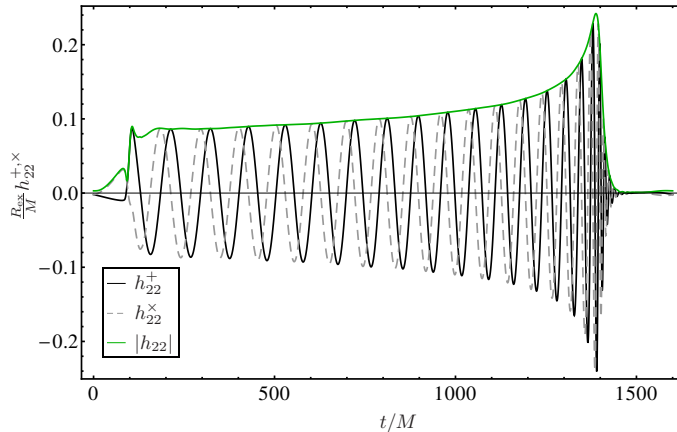


**Figure 2.3:** Metric waveforms  $h_{22}^+$  and  $h_{22}^{\times}$  (black and gray, dashed line, respectively) obtained from  $\Psi_4$  (for  $q = 10$ ,  $D = 10M$ , extracted at  $R_{\text{ex}} = 90M$ ) with FFI where the cutoff frequency is  $\omega_0 = 0.025$ , and their envelope,  $|h_{22}|$  (green line). Except for very early times, the amplitude  $|h_{22}|$  increases monotonically up to merger without any oscillations visible at the scale of the plot, indicating that the integration works well.

signal in time domain. Low frequency components could be amplified by the division by  $\omega$ , as shown in [66], and again lead to drifts in the final signal  $h(t)$ . Therefore, applying a high-pass filter to the data to suppress any modes at frequencies lower than the lowest frequency of the numerical data (which is determined by the initial data) was used in [73] and [DM6] (the methods of these papers differ in the choice of the particular transfer function). The authors of [74] additionally cut off all frequencies higher than four times the ringdown frequency. The authors of [66] argue that this procedure requires a certain amount of tuning of different parameters and is not applicable straightforwardly to different signals  $\Psi_4$  or different  $(l, m)$ -modes. They instead propose to use a fixed frequency integration (FFI) method.

We know that the lowest physical GW frequency  $\omega$  contained in the signal is determined by the initial data, and we can compute it approximately e.g. from the initial orbital frequency  $\Omega_i$ . The lowest GW wave frequency of the 22-mode is approximately given by  $\omega_i = 2\Omega_i$ , but initial eccentricity occurs approximately at the orbital frequency and we do not want to cut it. The authors of [66] showed, however, that the influence of such low-frequency modulations of the amplitude on the resulting signal is marginal. This knowledge guides the choice of a cutoff frequency  $\omega_0$  in the FFI method. The exact value of  $\omega_0$  still has to be adjusted by hand, and lies a little below the lowest physical frequency. All frequencies lower than  $\omega_0$  are now replaced

such that

$$\tilde{h}(\omega) = \begin{cases} -\frac{\tilde{\Psi}_4(\omega)}{\omega_0^2}, & \omega \leq \omega_0 \\ -\frac{\tilde{\Psi}_4(\omega)}{\omega^2}, & \omega > \omega_0. \end{cases} \quad (2.32)$$

Applying this method to the exemplary waveform used before, we find  $h_{22}^+(t)$  and  $h_{22}^\times(t)$  as shown in Fig. 2.3. The lowest GW frequency in the signal is approximately  $\omega = 0.055$  and we used a cutoff frequency of  $\omega_0 = 0.025$  for the plots presented here. On the scale of the plot, only in the very beginning there are visible oscillations in the amplitude of  $h_{22}$  (green line), which quickly decrease, and the influence of unphysical low frequency components has been suppressed effectively. There is still some freedom in the choice of  $\omega_0$  since we do not exactly know the value of the lowest physical frequency, but the choice is clearly guided by the initial orbital frequency and relatively straightforward.

In Fig. 2.4, the three methods discussed so far are compared. The amplitudes  $|h_{22}|$  resulting from time domain integration subtracting a linear (black line) or a cubic (blue dashed line) polynomial and the one obtained with the FFI method (green dashed line) are plotted on top of each other. The FFI method clearly results in the cleanest amplitude of the strain and is therefore superior to the time integration methods. When the appropriate cutoff frequency for the 22-mode is known, this approach can directly be applied to higher modes using cutoff frequencies  $\omega_0^{lm} = m\omega_0^{22}/2$ , which requires no further tuning. For these reasons, the fixed frequency integration method is our method of choice when computing the strain waveform  $h$  from the numerical data for  $\Psi_4$ .

## 2.5 Physical Parameters of a Simulation

The merger of a black hole binary produces one final black hole which, after some time of ringing down to its final state, is stationary or, in case of an asymmetric merger, additionally acquires linear momentum and is recoiled. Therefore, the final black hole can be characterized by its mass, its angular momentum and a recoil velocity.

In general relativity there is, however, no unique measure of a local mass nor (linear or angular) momentum. Nevertheless, global quantities, the Arnowitt–Deser–Misner (ADM) mass and momenta [75–77] can be assigned to the entire spacetime if it is asymptotically flat. In asymptotically Cartesian coordinates the ADM mass of a

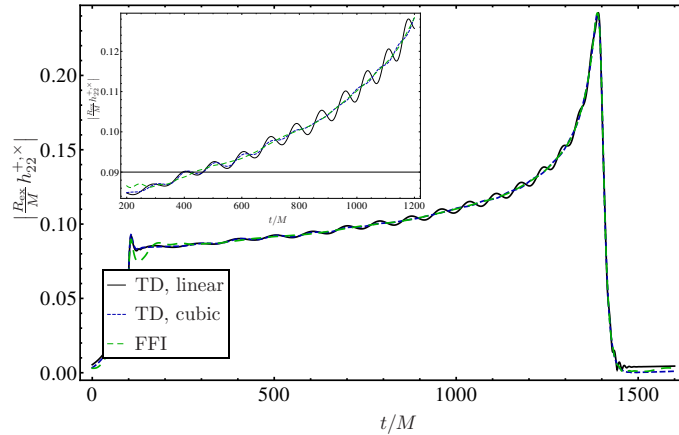


**Figure 2.4:** Comparison of the amplitude of  $h_{22}$  obtained with the time domain (TD) integrations using linear (black line) and cubic fitting (blue, dashed line) and the fixed frequency integration (FFI, green, dashed line) method as shown before in Figs. 2.2 and 2.3, respectively. The FFI method gives the cleanest result for  $h_{22}$  in the sense that its amplitude increases nearly monotonically up to merger without additional oscillations. The inset shows a zoom into the time range from after the passage of the junk radiation up to about  $200 M$  before merger.

spacetime is given by

$$M_{\text{ADM}} = \frac{1}{16\pi} \lim_{r \rightarrow \infty} \oint_{S_r} \gamma^{ij} [\partial_j \gamma_{ik} - \partial_k \gamma_{ij}] \hat{n}^k \, dA, \quad (2.33)$$

with  $\hat{n}^k = x^k/r$  the unit outward-pointing normal vector and  $dA$  the standard surface element. For the linear momenta we have

$$P_{\text{ADM}}^i = \frac{1}{8\pi} \lim_{r \rightarrow \infty} \oint_{S_r} (K^i_j - \delta^i_j K) \hat{n}^j \, dA, \quad (2.34)$$

and the angular momenta are given by

$$S_{\text{ADM}}^i = \frac{1}{8\pi} \lim_{r \rightarrow \infty} \oint_{S_r} \epsilon^{ijk} x_j (K_{kl} - \delta_{kl} K) \hat{n}^l \, dA. \quad (2.35)$$

The above expressions are defined at spatial infinity, in particular the surface integrals should be taken over a sphere  $S_r$  of infinite coordinate radius. In practice, this is not realizable and the integrals are calculated at certain radii as in the case of mode extraction of  $\Psi_4$  in the previous chapter. From the values at different radii, the asymptotic behavior towards infinite radius can be determined, usually by a  $1/r$  or

$1/r^2$  fit to the data. When determined at spatial infinity, the ADM quantities are time independent. They will be of particular importance in the construction of initial data in Chap. 3 because they allow us to determine mass, spin and momentum of the black holes present in the initial data. For the final parameters, we will only need  $M_{\text{ADM}}$ .

In order to determine the mass of the final black hole, we need to subtract the energy radiated away in form of gravitational waves from the total ADM mass of the spacetime. Because the ADM mass is constant in time, its value is determined at the initial time slice given in terms of the initial data discussed in Chap. 3. For this data,  $M_{\text{ADM}}$  can be computed using Eq. (3.13) which can be deduced from Eq. (2.33) in the case of a conformally flat metric. Now we also need to compute the radiated energy. Under the assumption of a weak gravitational field, it is possible to compute the energy lost by an isolated system of gravitating objects using the Weyl scalar  $\Psi_4$ . At a given time and in the limit of large distance from the source, the energy flux is given by [61]

$$\frac{dE}{dt} = \lim_{r \rightarrow \infty} \frac{r^2}{16\pi} \oint_{S_r} \left| \int_{-\infty}^t \Psi_4 dt' \right|^2 d\Omega, \quad (2.36)$$

with  $d\Omega$  being the standard solid angle element. Integrating Eq. (2.36) in time gives the total radiated energy  $E_{\text{rad}}$ . Finally, the mass of the remnant black hole,  $M_{\text{final}}$ , can be computed by subtracting the radiated energy from the ADM mass,  $M_{\text{final}} = M_{\text{ADM}} - E_{\text{rad}}$ .

Equation (2.36) can be used to get information about the importance of different multipoles of  $\Psi_4$ . Plugging Eq. (2.26) into Eq. (2.36), the energy flux in terms of individual modes becomes

$$\frac{dE}{dt} = \lim_{r \rightarrow \infty} \frac{r^2}{16\pi} \left| \int_{-\infty}^t \sum_{l,m} \Psi_4^{lm} dt' \right|^2. \quad (2.37)$$

For an equal mass binary without spins, it thus turns out that more than 98% of the energy radiated away from the system is contained in the  $l = 2, |m| = 2$  modes [69], which is why they are called the most dominant modes. While they remain very important with increasing mass ratio, the influence of higher modes becomes more and more considerable [69]. For example, the authors of [78] state that only about

75% of the total energy is radiated in the most dominant modes for the mass ratio  $q = 10 : 1$ .

Now we turn to determining the spin of the final black hole. When the apparent horizon of a black hole is known, its angular momentum can be calculated from Eq. (25) of [79]. This allows to calculate the angular momentum of the binary components during the simulation and of the final black hole when the evolution has settled to a stationary state. Apparent horizon finding slows down the computational speed, however, and we prefer to use the following method based on the quasi-normal modes emitted by the remnant black hole when it settles down. After merger, the GW signal behaves like  $\exp(-i\omega_{\text{rd}}t)$  and the authors of [80] relate the ringdown frequency  $M_{\text{final}}\omega_{\text{rd}}$  to the final spin  $a_{\text{final}}/M_{\text{final}}$ .  $\omega_{\text{rd}}$  is a complex frequency where the imaginary part,  $\Im(\omega_{\text{rd}})$ , is related to the exponential fall-off of the ringdown waveform and the real part,  $\Re(\omega_{\text{rd}})$ , is its frequency. In [80], the authors give tables containing different multipoles  $(l, m)$  and spins from zero to nearly maximal ( $a/M = 1$ ). In practice, we fit the tabulated data for a specific pair of  $(l, m)$  in order to get continuous data  $a_{\text{fit,real}} = a(\Re(\omega_{\text{rd}}))$  and  $a_{\text{fit,imag}} = a(\Im(\omega_{\text{rd}}))$ . Knowing the final mass in an NR simulation, we can use the amplitude and phase of our  $l = m = 2$  mode computed from  $\Psi_4$  in the ringdown regime and determine its fall-off rate and frequency. These values are finally plugged into the fit formulas  $a_{\text{fit,imag}}$  and  $a_{\text{fit,real}}$ , respectively, which will result in two values for the final spin (which agree in their error ranges). In [DM4] it was found that the method using the ringdown frequency results in lower error bounds.

In order to find analytic expressions for the final spin depending on the initial spins of the binary components, fits to the existing numerical data for initially (anti-)aligned spin vectors have been performed in [81, 82] or in [83] where additional information from the extreme mass ratio limit was used. For generic initial spins, numerical data was fit in [84], and in [85, 86] the fit formulas for initially (anti-)aligned spins were extended using extra assumptions. Analytical approximations to determine the final spin were used in [87, 88]. A combination of both approaches was applied in [89].

Finally, the kick velocity is to be calculated. In binaries with unequal masses and/or spins the net linear momentum radiated during inspiral, merger and ringdown is different from zero and peaks, as the gravitational wave amplitude, at merger. In the center-of-mass frame where the binary was originally at rest, the center-of-mass now acquires linear momentum opposite to the net momentum radiated by the binary.

This effect is known as kick or recoil and for non-spinning binaries is maximal at a mass ratio  $q = 2.8$  with a kick velocity  $v_{\text{kick}} = (175 \pm 11)$  km/s [90]. For binaries with spins originally lying in the orbital plane and pointing to the opposite direction of each other, the kick velocity may even become as large as  $v_{\text{kick}} = 4000$  km/s [91]. For equal mass binaries and equal spins aligned or anti-aligned to the orbital angular momentum, however, there is no overall kick. Only when the spin magnitudes are different, the kick velocity can reach about  $(448 \pm 5)$  km/s in this scenario [92]. In order to calculate the kick velocity, the amount of radiated linear momentum needs to be known. The radiated momentum flux is given in terms of  $\Psi_4$  by [93]

$$\frac{dP_i}{dt} = \lim_{r \rightarrow \infty} \frac{r^2}{16\pi} \oint_{S_r} l_i \left| \int_{-\infty}^t \Psi_4 dt' \right|^2 d\Omega \quad (2.38)$$

with  $l_i = (\sin \theta \cos \phi, \sin \theta \sin \phi, \cos \theta)$ . Integrating Eq. (2.38) over the time of simulation gives the total radiated momentum  $P_i$  in one direction, and the kick velocity follows from  $v_{\text{kick}} = (P_x^2 + P_y^2 + P_z^2)^{1/2} c/M$  with the velocity of light  $c$  and  $M$  the total mass of the system. As the initial data contains junk radiation (see the discussion at the end of Sec. 3.3) leaving the system at early times and carrying momentum with it which is not part of the momentum we wish to measure, the integration of Eq. (2.38) in time is usually started after that burst of radiation has left the system. There are many analytical approaches to determining the final kick velocity. Some authors fit to the existing numerical data, e.g. in [89, 90, 94], others employ analytical approximation techniques, e.g. [95, 96]. The authors of [87, 97] use symmetry arguments to obtain a map between initial and end state. It is remarkable that today even the anti-kick, which arises before the kick velocity settles to its final value, can be understood [98] analytically. An overview over the different methods to predict final spin and kick velocity can be found in the review [99].

In practice, the integrals in Eq. (2.36) and Eq. (2.38) are not calculated at spatial infinity but evaluated at the extraction radii of  $\Psi_4$  and extrapolated to infinity assuming a dependence on the radial coordinate as  $a + b/r$  or  $a + b/r + c/r^2$  [19, 63, 64, 100]. The value of  $a$  then gives the result at infinite distance.

## 2.6 Implementation in the BAM Code

The simulations presented in this thesis were done with the BAM code described in detail in [61, 101, 102]. The code solves the BSSN equations (2.13) – (2.17) with 1+log slicing, Eq. (2.18), and Gamma driver shift, Eq. (2.19), in the moving puncture framework using finite differencing (FD). In addition to solving the evolution equations as given in the previous sections, the code imposes the algebraic constraints  $\det(\tilde{\gamma}_{ij}) = 1$  and  $\text{tr}(A_{ij}) = 0$  at every time step. Furthermore,  $\tilde{\Gamma}^i$  is used as an independent variable only when derivatives of it appear, otherwise  $\tilde{\Gamma}^i = -\partial_j \tilde{\gamma}^{ij}$  is employed.

The cartesian grid is composed of nested boxes with increasing resolution, such that the resolution is highest close to the punctures, and the innermost boxes adaptively follow the puncture motion. The position of the puncture is tracked by integrating  $\partial_t x_{\text{punc}}^i = -\beta^i(x_{\text{punc}}^i)$  which follows from Eq. (2.17) and the fact that the conformal factor  $\chi$  vanishes at a puncture [18]. The spatial resolution, which is equal in all three directions, doubles from one box to the next larger one. Time integration is performed with a fourth order Runge–Kutta time integrator (RK4) and Berger–Olinger type time stepping. The time step  $\Delta t$  is closely related to the spatial resolution  $\Delta x$  through the Courant–Friedrichs–Lewy (CFL) stability condition [103]. In the BAM code, usually a Courant factor of  $C \leq 0.5$  is used, and the time step on each box is computed from  $\Delta t = C\Delta x$  such that it is larger for outer boxes than for inner ones. Spatial derivatives in the bulk are sixth order accurate. BAM adds Kreiss–Olinger dissipation terms to the right hand sides of the evolution equations. Unless stated otherwise, the order of dissipation is six, the same as used in [101]. In principle, the order of dissipation must be two orders higher than that of the FD scheme in order to not affect the overall accuracy. Eighth order dissipation is available now and is used in the most recent results, but in simulations which are compared to older runs, the same order of dissipation is used unless the subject of comparison is the dissipation itself.

The actual grid configuration used for a specific simulation is labelled by

$$\chi[l_1 \times N : l_2 \times 2N : buf : M/h_{\text{min}} : C]. \quad (2.39)$$

The appearance of  $\chi$  in the above expression emphasizes that we use the conformal factor  $\chi$ , the  $l_1$  innermost boxes contain  $N$  points in each direction, and  $l_2$  outer

boxes contain twice the number of points in one direction,  $2N$ . This way, the outer boundary can be pushed far away while the computational cost remains relatively low.  $buf$  is the number of mesh refinement buffer points around one box. The finest resolution of the grid is  $h_{\min}$ , and  $C$  is the Courant factor.

## 2.7 Convergence and Richardson Extrapolation

The waveforms we compute for GW detection purposes are needed to be very accurate. Inherently to the method, the accuracy of a numerical result is limited, for example by the finite, not at all infinitesimal resolution of the numerical grid or the time step size. Again, we can gain a certain amount of accuracy by post-processing the data obtained from a numerical solution, like in Sec. 2.4.1 where the results computed at finite extraction radii were extrapolated to infinite radius. Having two numerical solutions to a problem, computed at two different spatial resolutions  $h_1$  and  $h_2$ , at hand, and knowing the order at which the results converge, it is possible to perform a Richardson extrapolation to obtain a more accurate result.

Assume that we can write the numerical solution  $f$  as a function of spatial resolution  $h$  as

$$f(h) = c_0 + c_1 h^p + \mathcal{O}(h^{p'}), \quad (2.40)$$

with  $c_0 = f(0)$  the exact result (at infinite resolution),  $c_1$  a constant,  $p$  the (known) order to which the numerical solution is exact and  $p' > p$ . For two solutions  $f(h_1)$  and  $f(h_2)$  computed at resolutions  $h_1 \neq h_2$  we find after some algebra the exact result as

$$c_0 = \frac{Q^{-p} f(h_1) - f(h_2)}{Q^{-p} - 1} + \mathcal{O}(h^{p'}), \quad (2.41)$$

with  $Q = h_2/h_1$ . Both solutions  $f(h_1)$  and  $f(h_2)$  were exact to the order  $p$ , but the Richardson approximation

$$f_{\text{Rich}}(h_1, h_2) = \frac{Q^{-p} f(h_1) - f(h_2)}{Q^{-p} - 1} \quad (2.42)$$

has the smaller error term  $\mathcal{O}(h^{p'})$ , and hence we obtained a result which is closer to the exact solution.

In the literature, this method is frequently applied to the Weyl scalar  $\Psi_4(t)$  in order to produce a very accurate gravitational wave signal. That means that the Richardson



extrapolation is computed at all instants of time  $t$ , and the final signal is given by the combination of these,  $\Psi_{4,\text{Rich}}(t)$ . The additional extrapolation to infinite extraction radius is usually done before the Richardson extrapolation.

Although the FD order of the BAM code is six, there are various lower order components like the implementation of the outer boundary conditions or the interpolation of box boundary values in Berger–Oliger substeps. Therefore, the order at which the result converges is not clear a priori. A convergence analysis will give us information about the order of the dominant error term in our solution. For three simulations with  $N_1$ ,  $N_2$  and  $N_3$  points in one dimension and per box, respectively, the convergence factor for a certain convergence order  $p$  can be computed from

$$\text{cf}(p) = \frac{1/N_1^p - 1/N_2^p}{1/N_2^p - 1/N_3^p}. \quad (2.43)$$

If the relation  $f(N_1) - f(N_2) = \text{cf}(p) (f(N_2) - f(N_3))$  holds, we say that the result converges at order  $p$ . This is a result of the representation (2.40) of the solution  $f$ , with the resolution  $h$  replaced by the number of points  $N$  as  $h = B/N$ , and the box size  $B$  is kept constant for different resolutions.



# 3 Initial Data for Black Hole Binaries

There are many different approaches to solving the initial data problem. Here, only the methods used in the BAM code will be discussed in detail. For an overview over methods in use today, see e.g. [104].

We want to specify initial data on the spatial metric  $\gamma_{ij}$  and the extrinsic curvature  $K_{ij}$  and use those as initial conditions of the evolution equations (2.13) – (2.17). Because of the symmetry of  $\gamma_{ij}$  and  $K_{ij}$ , there are 12 independent degrees of freedom to be specified. As mentioned in Sec. 2.1, the constraint equations, Eqns. (2.8) and (2.9), have to be solved on the initial hypersurface,  $t = 0$ . They provide us with four equations on 12 unknowns, and it is a priori not clear which quantities are to be left freely specifiable and which we want to fix by solving the constraints. The York–Lichnerowicz conformal decomposition [43, 105, 106] followed by the transverse traceless decomposition aide picking four of the unknowns to be determined by the constraints. The remainig eight quantities will be freely specifiable.

## 3.1 Conformal Decomposition

Instead of arbitrarily picking one of the metric components to be determined by the Hamiltonian constraint, it might be more reasonable to constrain an overall scale factor such that we do not introduce some doubtful asymmetry between the different components. Therefore, a conformal decomposition of the spatial metric is performed,

$$\gamma_{ij} = \psi_0^4 \bar{\gamma}_{ij}. \tag{3.1}$$

Using the decomposition of the extrinsic curvature into its trace  $K$  and trace-free part  $A^{ij}$  given in Sec. 2.2, and conformally decomposing  $A^{ij}$  according to

$$A^{ij} = \psi_0^{-10} \bar{A}^{ij}, \tag{3.2}$$

[27] we can express the Hamiltonian constraint, Eq. (2.8), in terms of the conformal quantities. It then becomes a differential equation on the conformal factor,

$$8\bar{D}^2\psi_0 - \bar{R}\psi_0 + \psi_0^{-7}\bar{A}_{ij}\bar{A}^{ij} - \frac{2}{3}\psi_0^5K^2 = 0. \quad (3.3)$$

Here,  $\bar{D}^2$  is the Laplace operator,  $\bar{D}^2 = \bar{\gamma}^{ij}\bar{D}_i\bar{D}_j$ , and  $\bar{R}$  is the Ricci scalar, both associated with the conformal metric. We raise and lower indices of conformal quantities with the conformal metric. It turns out that the conformal decompositions we performed, especially the one of the conformal metric, lead to the transformation of the Hamiltonian constraint into an equation which, for physically interesting choices of the extrinsic curvature, is elliptic. In addition to the considerations about how to choose the free variables, this finding in retrospect supports the ansatz using conformal decomposition.

The momentum constraints Eq. (2.9) are rewritten as well and we obtain

$$\bar{D}_j\bar{A}^{ij} - \frac{2}{3}\psi_0^6\bar{\gamma}^{ij}\bar{D}_jK = 0. \quad (3.4)$$

With the conformal decomposition (3.1) and the rewriting (3.3) of the Hamiltonian constraint as an equation on  $\psi_0$ , the components of the conformal metric  $\bar{\gamma}_{ij}$  are left as freely specifiable and we choose conformal flatness,  $\bar{\gamma}_{ij} = \delta_{ij}$ . Because Eqns. (3.3) and (3.4) are coupled through the trace  $K$  of the extrinsic curvature, it is convenient to choose  $K = 0$ . Having made these choices, the momentum constraints are to be solved for  $\bar{A}^{ij}$ . Only then can we solve Eq. (3.3).

## 3.2 Bowen–York Extrinsic Curvature (Momentum Constraints)

In case of maximal slicing we set  $K = 0$  and the momentum constraints, Eq. (3.4), reduce to

$$\bar{D}_j\bar{A}^{ij} = 0. \quad (3.5)$$

In order to rewrite Eq. (3.5) as three equations for three unknowns without arbitrarily introducing an asymmetry between the components of  $\bar{A}^{ij}$ ,  $\bar{A}^{ij}$  is further split into a transverse and a longitudinal part following the conformal transverse–traceless

(CTT) decomposition [107]. Because this split moves two degrees of freedom into the transverse and three into the longitudinal part, the transverse part is chosen as freely specifiable and is assumed to vanish. Three equations for the three degrees in the longitudinal part are left to be solved for. This way, BOWEN and YORK found an analytical solution to the momentum constraints which corresponds to a black hole with momentum and spin. The Bowen–York (conformal) extrinsic curvature for a black hole at the origin  $r = 0$  reads [108]

$$\bar{A}^{ij} = \frac{3}{2r^2} (\hat{n}^i P^j + \hat{n}^j P^i - \hat{n}_k P^k (\hat{n}^i \hat{n}^j - \delta^{ij})) + \frac{3}{r^3} (\hat{n}^i \epsilon^{jkl} + \hat{n}^j \epsilon^{ikl}) S_k \hat{n}_l. \quad (3.6)$$

Here we assume Cartesian coordinates,  $r$  is the coordinate distance to the center of the black hole,  $\hat{n}^i = x^i/r$  is the unit outward–pointing normal vector, and  $\epsilon^{ijk}$  is the contravariant Levi–Civita tensor in three dimensions (in our convention  $\epsilon^{123} = 1$ ).  $P^i$  and  $S^i$  are constant vectors which will be discussed below. We obtain the extrinsic curvature itself by plugging the solutions above into Eq. (3.2) which after solving the Hamiltonian constraint for  $\psi_0$  gives us  $K^{ij}$ , as we take  $K = 0$ .

In a region far away from any black holes, where we expect the conformal factor to tend to one, we can calculate the ADM integrals (2.34) and (2.35) using the solution (3.6) and  $K^{ij} \simeq \bar{A}^{ij}$ , and we obtain  $P_{\text{ADM}}^i = P^i$  and  $S_{\text{ADM}}^i = S^i$ . The Bowen–York parameters  $P^i$  and  $S^i$  are the components of the ADM momentum and spin and therefore have a clear physical meaning. This allows us to specify initial data for black holes with momentum and spin through Eq. (3.6). Our method to determine useful values for  $P^i$  and  $S^i$  will be discussed in Sec. 3.5.

The linearity of Eq. (3.5) permits to add solutions of type (3.6) and obtain new solutions which correspond to spacetimes with more than one black hole. In each extra term we add,  $r$  denotes the coordinate distance to the individual black hole sitting at  $\vec{r}_a$ ,  $r = |x^i - r_a^i|$ , and the normal vector becomes  $\hat{n}^i = (x^i - r_a^i)/r$ . The momenta  $P^i$  and spins  $S^i$  also differ for each extra black hole term. We find that the momentum of the entire spacetime is the sum of the momenta we plug into each extra Bowen–York term,  $P_{\text{ADM,total}}^i = \sum_a P_a^i$ . The  $P_a^i$  are the momenta of the  $a^{\text{th}}$  black hole in the limit of infinite separation of the binary. The same is true for the spin parameters.

### 3.3 Punctures (Hamiltonian Constraint)

Having found the solution (3.6) to the momentum constraints, we can plug it into the equation for the Hamiltonian constraint and solve for the conformal factor  $\psi_0$ . From the discussion in the previous chapter, we know  $\bar{\gamma}_{ij} = \delta_{ij}$ , and  $K = 0$  and Eq. (3.3) reduces to

$$8\Delta\psi_0 + \psi_0^{-7}\bar{A}_{ij}\bar{A}^{ij} = 0. \quad (3.7)$$

$\Delta$  is the Laplacian in flat space. No analytical solution to this equation has been found when the extrinsic curvature does not vanish, which is the case if  $P^i \neq 0$  or  $S^i \neq 0$  in Eq. (3.6), and numerical techniques have to be used.

Solving Eq. (3.7) numerically requires the usage of proper boundary conditions. At the outer boundary, we assume the spacetime to be asymptotically flat. Near the black holes, we can expect the conformal factor to become singular, and appropriate treatment becomes necessary. The widely used method today that we will adopt here is the puncture approach introduced by BRANDT and BRÜGMANN which removes the necessity of complicated inner boundary conditions as was obligatory in the former method of images [107, 109]. In [110], the authors adapt an approach of MISNER and WHEELER [111] as well as BRILL and LINDQUIST [112] who solved Eq. (3.7) for vanishing extrinsic curvature,  $K^{ij} = 0$ , analytically, which results in initial data for non-moving, non-spinning black holes. In this case, the conformal factor for  $N$  black holes was found to be

$$\psi_0^{\text{BL}} = 1 + \sum_{i=1}^N \frac{m_i}{2|\vec{r} - \vec{r}_i|}, \quad (3.8)$$

and it is defined on  $\mathbb{R}^3$  with the points  $\vec{r}_i$  removed, which is called a ‘‘punctured’’  $\mathbb{R}^3$ . BRANDT and BRÜGMANN use this knowledge and split the conformal factor according to

$$\psi_0 = \frac{1}{\kappa} + u \quad \text{with} \quad \frac{1}{\kappa} = \sum_{i=1}^N \frac{m_i}{2|\vec{r} - \vec{r}_i|}. \quad (3.9)$$

Now the Hamiltonian constraint is rewritten in terms of  $u$ ,

$$\Delta u + \lambda(1 + \kappa u)^{-7} = 0, \quad (3.10)$$

with  $\lambda = \frac{1}{8}\kappa^7\bar{A}_{ij}\bar{A}^{ij}$  and  $\bar{A}^{ij}$  the sum of Bowen–York solutions (3.6) corresponding to multiple black holes. This leaves an elliptic equation on the correction term  $u$ .

Asymptotic flatness requires  $u - 1 = \mathcal{O}(r^{-1})$ . The key idea now is to integrate Eq. (3.10) on  $\mathbb{R}^3$  without any points removed. Because the singular terms have been moved into  $\kappa$ ,  $u$  is expected to stay regular across the punctures, and it turns out that this is indeed the case. For this reason, no inner boundary condition is needed, which greatly simplifies the method. In [110], the authors show existence and uniqueness of a solution to Eq. (3.10) which is  $\mathcal{C}^2$  everywhere, including the punctures. They furthermore show that the resulting topology is that of  $N + 1$  asymptotically flat ends where  $N$  of them have been compactified. Approaching the punctures, the metric becomes asymptotically flat again, as it does far away from the punctures.

The ADM mass of each single puncture can be estimated by going to the other asymptotically flat end (the one near the puncture). It is then given by

$$M_i = m_i \left( u(\vec{r}_i) + \sum_{\substack{j=1 \\ j \neq i}}^N \frac{m_j}{2|\vec{r}_i - \vec{r}_j|} \right), \quad (3.11)$$

and the  $m_i$  are the bare mass parameters from  $\kappa$  in Eq. (3.9). For non-spinning binaries, the results obtained with this formula agree very well with the horizon mass of a black hole given by

$$M^2 = M_{\text{irr}}^2 + \frac{S^2}{4M_{\text{irr}}^2}, \quad (3.12)$$

with  $M_{\text{irr}}^2 = A_{\text{H}}/(16\pi)$  and  $A_{\text{H}}$  the area of the apparent horizon. When spins are involved, the agreement diminishes with increasing spin magnitude as shown in [DM4].

In puncture data, the ADM mass of the entire spacetime can be calculated from the bare masses  $m_i$  and the correction to the conformal factor,  $u$ . In case of a conformally flat metric as we use here, the expression for the ADM mass, Eq. (2.33), can be transformed into an equation using the conformal factor, only. With Eq. (3.9), the ADM mass of a spacetime containing  $N$  punctures can thus be calculated by [113]

$$M_{\text{ADM}} = -\frac{1}{2\pi} \lim_{r \rightarrow \infty} \oint \partial_i \psi s^i dA = \sum_{i=1}^N m_i + \lim_{r \rightarrow \infty} 2ru. \quad (3.13)$$

The BAM code solves Eq. (3.10) using a spectral solver [113]. The initial values we specify are the puncture masses  $M_i$ , the momenta  $P_a^i$ , the spins  $S_a^i$  and the positions  $\vec{r}_a^i$  of the punctures. The solver calculates the correction term  $u$ , the bare mass

parameters  $m_i$  from Eq. (3.11) as well as the ADM mass of the entire spacetime through Eq. (3.13).

The initial data for the 3-metric  $\gamma_{ij}$  and the extrinsic curvature  $K_{ij}$  just obtained are subject to various ongoing improvements. Due to the assumption of flatness of the conformal metric  $\bar{\gamma}_{ij}$ , the data does contain spurious radiation which during an evolution leaves the system in an unphysical initial burst, the junk radiation. Attempts to move away from conformal flatness were e.g. made in [114–116]. As found by [117], the puncture geometry of our initial data changes at the beginning of a simulation, and the stationary states are described better by slices which do not contain the second asymptotically flat end presented by the puncture. Such data has been constructed e.g. in [118–120]. Finally, the slicing condition  $K = 0$  is different from 1+log slicing, Eq. (2.18), used during evolution and leads to rapid gauge adjustments at the beginning of simulations. Giving up maximal slicing in the initial data means, however, that the constraints do not decouple, and we can not use the analytically given Bowen–York extrinsic curvature. For binaries, first attempts in this direction have been made in [121].

### 3.4 Initial Data for Lapse and Shift

We use the gauge conditions Eq. (2.18) and Eq. (2.19) which are evolution equations on the lapse and shift vector and therefore, we need to specify initial data for these quantities, too. In early NR simulations, the initial lapse was taken to be one uniformly on the grid. Using 1+log slicing for the evolution, the lapse collapsed to zero at the black hole throat but stayed one at the puncture. On the numerical grid, this leads to steep gradients in the region between throat and puncture. We therefore use a pre-collapsed lapse in the initial time slice,

$$\alpha(t = 0) = \psi_0^{-n}, \quad (3.14)$$

with  $\psi_0$  the conformal factor given in last section and  $n > 0$ , a number typically set to  $n = 2$ . This guarantees that the lapse vanishes at the puncture and avoids the development of large gradients. For the shift vector,  $\beta^i(t = 0) = 0$  is used.



### 3.5 Black Hole Binaries in Quasi-Circular Orbits

The specification of initial data for numerical simulations of black hole binaries is not finished until we choose the momentum and spin parameters,  $P^i$  and  $S^i$ , respectively, in the Bowen–York solution to the momentum constraints. Only after that can we solve the Hamiltonian constraint. We could simply choose six arbitrary numbers and perform numerical simulations to find out what kind of physical situation these numbers imply. This is, however, not very useful and we prefer to do systematic studies of the parameter space.

Insight is provided by calculations for two point particles orbiting each other on elliptic orbits with a certain initial eccentricity. In the limit where the velocities of the particles are much smaller than the velocity of light (Keplerian orbits) and the radiation effects are small such that the quadrupole formula for the energy carried away by gravitational waves is valid, the eccentricity of the orbit decreases [122–124]. The orbit not only decays but in addition is circularized by emission of gravitational waves. This happens on a time scale which is much smaller than the time it takes the binary to merge [122, 124]. For this reason, we can expect most of the astrophysically relevant binary systems to have circularized by the time they reach a separation  $D$  at which a numerical simulation would be started, which is typically  $D \simeq 10 M$  (with  $M$  the total mass of the system). Given this knowledge, we want to specify values of  $P^i$  which lead to quasi-circular trajectories with minimal residual eccentricity. Black hole binaries on eccentric orbits are discussed e.g. in [125–129].

For GW detection with matched filtering, eccentricity plays a non-negligible role, too. Any residual eccentricity will be visible in the gravitational waves extracted from the simulation and will therefore affect the templates built from them. Mainly, eccentricity has an impact on the phase accuracy of a waveform, which in turn alters the mismatch [130] determining whether a signal can be detected with a given template bank or not. There are parameter estimation studies proposing that LISA will be able to distinguish eccentricities down to  $10^{-4}$  for non-spinning binaries [131] and  $10^{-3}$  for spinning ones [132].

The first method for producing quasi-circular orbit parameters was based on Newtonian physics and minimized the effective potential energy of the system [133]. These data have to be translated for use in the puncture framework [134, 135]. Another approach is to rely on an approximate helical Killing vector [136–138]. A sequence

of quasi-circular parameters using this method has been computed in [139]. The authors of [140] have refined this quasi-equilibrium method in order to allow for a non-zero radial momentum parameter. In particular, they perform numerical simulations of a few orbits (one to two), measure the resulting eccentricity and vary their initial parameters until the measured eccentricity is minimal.

The simulations in this thesis are based on the usage of initial parameters resulting from PN or EOB methods in which the black holes are represented as point particles. In what follows we will work in center-of-mass coordinates where the total linear momentum is zero, and we have  $\vec{P}_1 = -\vec{P}_2$ . We choose the orbital angular momentum vector  $\vec{L}$  to point in  $z$ -direction such that  $z = 0$  is the (initial) orbital plane. What is left to be specified is the parameter  $P_t$  describing the momentum tangential to the orbital trajectory as well as  $P_r$  which is the momentum in radial direction, pointing towards the center-of-mass. The separation of the two particles will be described by the orbital radius  $R$  or the orbital distance  $D$ .

### 3.5.1 Measuring Eccentricity

In order to quantify the differences between various methods for determining initial parameters on momentum and spin, we need a measure of eccentricity of the binary's orbit. The most widely used methods employ the coordinate distance  $D(t)$  of the punctures during the simulation or the orbital frequency  $\omega(t)$  [63, 140–142].

Using the orbital distance, we compare the curve  $D(t)$  with an ideal, quasi-circular curve  $D_c(t)$ . If the inspiral contains a (small) eccentricity, this shows in the  $D(t)$  curve by small oscillations which decrease in time, see Fig. 3.1 for an example. The ideal curve is obtained by averaging out these oscillations through a fit to the data given by  $D_c(t) = \sum_{i=1}^4 a_i (t_m - t)^{i/2}$ . The parameter  $t_m$  is the merger time which in our case is a fitting parameter. Figure 3.1 exemplifies this averaging process in a simulation with very high eccentricity. The eccentricity is computed from [142]

$$e_D(t) = \frac{D(t) - D_c(t)}{D_c(t)}. \quad (3.15)$$

Due to the gauge adjustments at the beginning of a simulation, the coordinate distance can only be used after about one orbit. Later on, when the binary components are too close, the fit function approaches zero and at merger time, Eq. (3.15) can not

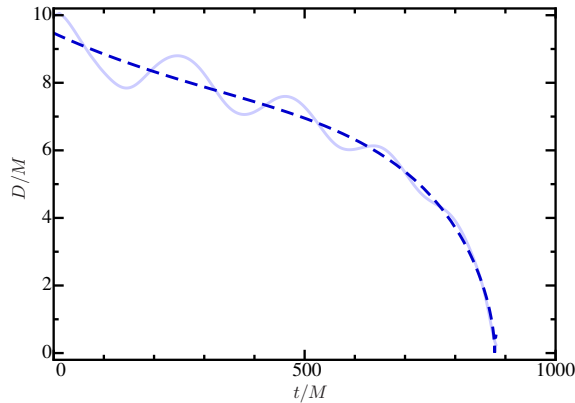


**Figure 3.1:** Illustration of the averaging procedure when measuring eccentricity with Eq. (3.15). Plotted is the puncture distance in time for two spinning black holes with equal masses. The solid line shows the distance measured during the simulation and reveals large oscillations due to relatively high eccentricity. The dashed line is the fit  $D_c(t)$  averaging out the oscillations.

be used any more. Anyhow, the coordinate tracks cease to describe the black hole motion reliably near merger, and we stop the eccentricity measurement. In the end, eccentricity is measured in a time interval during the inspiral as shown by the dashed line in Fig. 3.2. We call the global extremum of the resulting  $e_D(t)$  curve, usually located at early times, “eccentricity of the simulation”. For the orbital frequency  $\omega(t)$  the same procedure can be applied with a fit function following  $\omega_c(t) = \sum_{i=0}^4 b_i t^i$  [143]. In this case, the eccentricity is calculated via  $e_\omega(t) = [\omega(t) - \omega_c(t)]/2\omega_c(t)$ .

In a different method [140], some functional dependence is fit to the oscillations themselves. We used this method for comparison in [DM1], but since it works well only in a small time frame (over about one period of oscillation), the results rather have snapshot character and we do not use them for general eccentricity estimates. As done in [DM1] we give eccentricity values based on  $e_D$ , with conservative error estimate  $\Delta e = \pm 0.001$  based on the variations in the extrema of  $e_D$ .

Recently, the authors of [144] proposed a way to measure eccentricity in a coordinate independent way using the GW signal given in terms of  $\Psi_4$ . This definition is, however, sensitive to initial junk radiation, and in the beginning of a simulation, where the eccentricity is largest, the signal is rather weak and noisy. The authors of that method find that their new definition agrees quite well with the definitions based on the orbital distance or orbital frequency and therefore continue to use the measurement based on orbital distance.

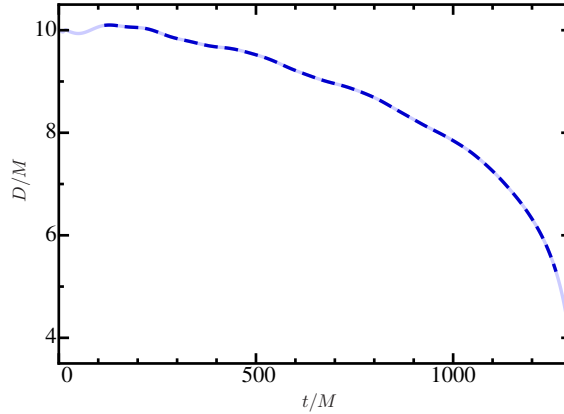


**Figure 3.2:** Puncture distance in time for non-spinning black holes with mass ratio  $q = 4$  for measuring eccentricity with Eq. (3.15). The solid line is the distance as measured during the entire simulation. The dashed line shows the time range in which the distance can be used for eccentricity measurements.

### 3.5.2 Integrating post-Newtonian Equations of Motion

In [61], a formula for the tangential momentum at 3PN order is derived for non-spinning binaries,

$$\begin{aligned} \frac{P_t}{\mu} = & \sqrt{\frac{M}{D}} + 3 \left( \frac{M}{D} \right)^{3/2} + \frac{1}{16} (42 - 43\nu) \left( \frac{M}{D} \right)^{5/2} \\ & + \frac{1}{128} [480 + (163\pi^2 - 4556)\nu + 104\nu^2] \left( \frac{M}{D} \right)^{7/2}. \end{aligned} \quad (3.16)$$

Here, the reduced mass is  $\mu = M_1 M_2 / M$  and  $\nu = \mu / M$ . If spin is to be included, a 2PN accurate formula for the tangential momentum is given in [145] (derived from [146]). Together with setting  $P_r = 0$ , Eq. (3.16) and the 2PN accurate version were used in a number of puncture simulations. Their clear drawback is the vanishing radial momentum which is contradictory to a decrease of the orbital radius expected when gravitational waves are emitted. This leads to rather high eccentricities of e.g.  $e = 0.012$  for an equal mass binary with initial separation  $D = 11M$  when the 2PN formula is used (with spins set to zero) [142] or  $e = 0.007$  [DM1] when Eq. (3.16) is used for the same configuration.

The above approaches lack the radial momentum because radiation reaction effects are neglected. Therefore, a natural step to improve the data is to include radiation reaction. The price to pay is that the momenta can no longer be given in closed form.

$q$	$S_i/M_i^2$	$D/M$	$e$	$D/M$	$e$	$e_{2\text{PN}/3\text{PN}}$
1	-0.85	13.0	0.009 (0.0025)			
1	-0.75	13.0	0.008 (0.0016)			
1	-0.50	12.5	0.0045 (0.0029)			
1	-0.25	12.0	0.004 (0.0025)	12.0	0.005	
1	0	12.0	0.0018	11.0	0.002	0.007
1	0.25	12.0	0.0061	12.0	0.0015	0.009
1	0.50	11.0	0.0061	11.0	0.005	
1	0.75	10.0	0.0060			
1	0.85	10.0	0.0050	10.0	0.014 (0.007)	
2	0	10.0	0.0023	10.0	0.002	
2	{0.6, -0.15}			10.0	0.002	
3	0	10.0	0.0016			
4	0	10.0	0.0038	10.0	0.003	0.006
10	0			10.0	0.002	0.004

**Table 3.1:** Summary of eccentricities calculated with different initial parameters according to the methods described in the text. The first column is the mass ratio  $q = M_2/M_1$ , the second one gives the dimensionless spin parameter where a positive (negative) sign means the spins point in positive (negative)  $z$ -direction.  $D/M$  is the coordinate distance between the punctures and  $e$  is the eccentricity measured using Eq. (3.15). The third and fourth column refer to simulations presented in [DM4]. The values in brackets were obtained using the PN iteration method described in the text (cf. Sec. 3.5.2), the other values result from using the PN evolution method of [142] including NLO terms. The uncertainties in these results are estimated to  $\Delta e = \pm 0.0005$ . Columns five and six summarize the results found with the method of [DM1] (described in Sec. 3.5.3). Here, the value in brackets was obtained when including spin-spin coupling. Only the minimum of the eccentricities we obtained using either TH or EH data is listed. The error estimate here is  $\Delta e = \pm 0.001$ . The last column indicates the eccentricity obtained when using the 3PN accurate Eq. (3.16) for simulations without spins and the 2PN accurate formula of [146] for the  $\chi_i = 0.25$  case.

In [142] the PN equations of motion for two point particles (cf. Eqns. (A.1)–(A.3)) are therefore integrated numerically, starting at a relatively large binary separation (e.g.  $D = 40 M$ ) with initial data from Eq. (3.16) and  $P_r = 0$ . At the separation where the numerical simulation is supposed to start ( $D \simeq 10 M$ ), the PN evolution is stopped and the values of  $P_t$  and  $P_r$  are read off. With this method, the eccentricity of the above example could be reduced down to  $e = 0.002$ . Low eccentricity using this method was also reported e.g. in [74, 130]. In the presence of non-zero spins, the method had to be refined which was done in [DM4]. The inclusion of next-to-leading order (NLO) spin-orbit (SO) coupling terms [147–149] in the Hamiltonian and the radiation flux was necessary in order to reduce the eccentricity to the order of  $\sim 10^{-3}$  for spins aligned or anti-aligned to the orbital angular momentum (see Tab. III in [DM4] or Tab. 3.1). Still, for spins anti-aligned with the orbital angular momentum, the eccentricities remained relatively high. The authors therefore

incorporated one additional step inspired by the iteration method of [140] mentioned above. Note that in simulations with puncture initial data, it is not practical to use the method exactly as presented in [140]. There, the initial data is specified using the conformal thin sandwich approach where the coordinate motion is known through the specification of the correct shift vector in the initial data. In the simulations presented in this work, this is not the case. Further, the gauge of the initial data and the evolution is not the same (maximal vs 1+log slicing and vanishing vs Gamma driver shift) and it takes roughly one orbit to adjust. Only then a motion corresponding to quasi-circular inspiral starts, and we would need much more than one orbit in order to measure eccentricity reliably. As a result, iterating many times would be computationally expensive. The authors of [144] recently suggested to use this type of iteration method but with relatively low resolution in the numerical setup in order to reduce the computational cost.

In [DM4], the iteration is done using PN evolutions instead of numerical ones, which takes much less time. The procedure is as follows. As an example system, we use an equal mass binary with spins pointing to the opposite direction of the total angular momentum vector,  $\vec{L}$ . The spin magnitudes are  $\chi_i = |\vec{S}_i|/M_i^2 = 0.5$ . As described above, the authors perform a PN evolution starting at a relatively high initial separation and evolve until the orbital distance has decreased to where the numerical simulation is supposed to start, in this example  $D = 12M$ . With the momenta obtained this way, a numerical simulation is performed to read off the resulting eccentricity which is  $e = 0.004$ . If the PN evolution had continued down to e.g.  $D' = 9M$ , the eccentricity of the PN orbit measured between  $D$  and  $D'$  would be extremely low because in the PN evolution, the system has circularized. Continuing the PN evolution down to  $D'$  is equivalent to starting a PN evolution at  $D$  with initial momenta as those just obtained. The authors now ask for how much the parameters have to vary in order to produce an eccentricity in the PN evolution starting at  $D$  which is as high as the one found in the NR simulation. The (rather ad hoc) assumption is that a variation in the parameters that produces eccentricity in the PN evolution, decreases it in the numerical simulation. Now two more numerical runs are necessary: one where the parameters are decreased by the amount found in the PN iteration, and another where they are increased. In the example run, a change of 0.15% was found to produce  $e = 0.004$  in the PN evolution from  $D$  to  $D'$ , so the parameters were increased and decreased by this amount, and the two additional

numerical simulations were started. The increase by 0.15% was successful and led to  $e = 0.003$ . An additional iteration step like the one just described did not lead to further improvement. This method was used for all anti-aligned spin configurations in [DM4] and succeeded in decreasing the eccentricities by factors of 1.5 up to 5 (see the fourth column of Tab. 3.1).

### 3.5.3 Analytical Approach

In [DM1], we pursued yet another approach which was first proposed in [150]. In that work, the initial parameter algorithm was used for analytical models, only, and not tested within numerical simulations. Furthermore, it was written in kinematical quantities instead of dynamical ones, which is less convenient for use in numerical evolutions. The underlying idea is to first calculate a sequence of spherical orbits from a Hamiltonian system of equations of motion for two point particles (cf. Eqns. (A.1)–(A.3)) ignoring radiation reaction and then include radiation reaction to obtain the rate at which the orbital radius decreases.

The full Hamiltonian is composed of orbital and spin parts,  $H = H^0 + H_{\text{SO}} + H_{\text{SS}}$ . In the literature, different versions of the orbital Hamiltonian  $H^0$  are derived. In [DM1], we use two of them for comparison purposes. We follow the choice of [150] and use either a 3PN accurate Taylor expanded Hamiltonian or an EOB one. For convenience of the reader, the expressions can be found in Eqns. (A.4)–(A.8) and (A.9)–(A.12), respectively. Spin contributions are added through  $H_{\text{SO}}$  given in Eq. (A.13). This part of the Hamiltonian only accounts for leading-order spin-orbit coupling terms. For completeness, the spin-spin (SS) coupling Hamiltonian  $H_{\text{SS}}$  is given by Eq. (A.14) although we will neglect it in the following. The reason is that in the formulation of [150], the conservative equations (where radiation reaction is not present) allow for solutions with constant radius  $R$  in the absence of spin-spin coupling, only. That is, if the Hamiltonian considered only comprises orbital motion and spin-orbit coupling,

$$H(R, P_r, P_t, \vec{S}_1, \vec{S}_2) = H^0(R, P_r, P_t) + H_{\text{SO}}(R, P_r, P_t, \vec{S}_1, \vec{S}_2). \quad (3.17)$$

In particular, the full Hamiltonian does not depend on any other spatial coordinate than the orbital radius  $R$  when  $H_{\text{SS}}$  is neglected. In most cases, the spin-spin coupling term is much smaller than the spin-orbit term anyhow.

In the absence of radiation reaction, asking for spherical orbits means  $[P_r]_0 = 0$  and

$$0 \stackrel{!}{=} [\dot{P}_r]_0 = - \left[ \frac{\partial H}{\partial R} \right]_0, \quad (3.18)$$

which we want to solve for the tangential momentum  $P_t$ . The subscript “0” emphasizes the fact that the values are meant to be taken at the initial time slice, and a dot represents a derivative with respect to the time variable  $t$ . As a starting value for an iterative solution to Eq. (3.18), Eq. (3.16) is employed. In a second step, radiation reaction is not ignored any more, and the non-conservative equations of motion are solved for the radial momentum  $P_r$  using  $[P_t]_0$  just obtained. Under the assumption of adiabatic inspiral, the change in orbital radius is given by

$$[\dot{R}]_0 = \frac{[dE/dt]_0}{[(dE/dR)_{\text{sph}}]_0}, \quad (3.19)$$

and the radial momentum can be computed from

$$[P_r]_0 = \frac{[\dot{R}]_0}{2 \left[ \frac{\partial H}{\partial (P_r^2)} \right]_0}. \quad (3.20)$$

The Taylor expanded energy flux  $dE/dt$  is given in Eq. (A.16), and the energy difference between adjacent spherical orbits,  $[(dE/dR)_{\text{sph}}]_0$ , can be found in Eq. (A.18). For the energy flux, a Padé resummation of Eq. (A.16) is also frequently used.

There is one subtlety involved when using the EOB Hamiltonian. While the PN formalism uses Arnowitt–Deser–Misner transverse traceless (ADM TT) coordinates [151] which are found to agree at least up to 1.5PN order with the conformally flat Bowen–York puncture initial data we employ for numerical evolutions (cf. Secs. 3.2 and 3.3), the EOB formalism uses different coordinates. Because the EOB coordinates are not expected to be close to our numerical coordinates, a transformation to ADM TT coordinates has to be performed. The 3PN accurate transformation is outlined in Eq. (A.25). In principle, the coordinate transformation should be employed in the full Hamiltonian (3.17), including the spin parts. Following [150], we for simplicity continued to use ADM TT coordinates in  $H_{\text{SO}}$  and  $H_{\text{SS}}$  since the corrections are supposed to be of higher PN order in these terms.

Starting from given values of  $M_1$ ,  $M_2$ ,  $S_1$ ,  $S_2$  and the distance  $D$ , we obtained the



$q$	$M_1/h_{\min}$	$h_{\max}/M$	$r_{\text{out}}/M$	$(l_1, l_2)$
1	21.33	12	774	(5,5)
2	18.67	36.6	2067	(4/5,7)
$2_{\text{NRAR}}$	31.98	21.35	2060	(4/5,7)
4	24.0	17.1	1237	(3/5,7)
10	26.81	13.96	1124	(6,7)

**Table 3.2:** Grid setups of the different types of numerical simulations used for testing EHPF and THTF initial data. The total mass of the system is  $M = M_1 + M_2$ . The resolution of the finest grid covering the smaller black hole is  $h_{\min}$ .  $r_{\text{out}}$  is the position of the outer boundary. The number of moving boxes around the punctures is given by  $l_1$  and in some cases, we put more boxes around the smaller black hole than around the larger one, indicated by a “/” between these numbers. The number of outer, non-moving boxes is given by  $l_2$ . All results in Secs. 3.5.4 and 3.5.5 corresponding to the same mass ratio (but e.g. different initial separations or spins) were obtained with the setups given here, except for the spinning simulation with mass ratio  $q = 2$ , which is listed here as  $q = 2_{\text{NRAR}}$ .

tangential momentum from Eq. (3.18) and the radial one from Eq. (3.20). With those plugged into the Bowen–York extrinsic curvature Eq. (3.6), the Hamiltonian constraint Eq. (3.10) can be solved and the construction of initial data is complete. We tested the performance of our method in several numerical simulations in [DM1], and some of the results, including two new cases, will be presented in the following two sections.

### 3.5.4 Results for non–Spinning Binaries

In this section, different equal and unequal mass binary configurations with vanishing initial spins are analyzed for their eccentricity when the initial data construction described in the previous sections are used. The grid configurations for the simulations are summarized in Tab. 3.2. When comparing different methods, we will use the following naming convention: Initial data obtained from Eq. (3.16) will be called “3PN circular”, those obtained in [142] and briefly discussed in Sec. 3.5.2 are labelled “PN evolved”. The data obtained by the PN iteration method of [DM4], also discussed in Sec. 3.5.2, will be named “PN iterated”. Finally, the methods described in Sec. 3.5.3 are labelled according to their Hamiltonian (Taylor expanded or EOB) and their flux function (Taylor expanded or Padé resummed). The four possible combinations are THTF (Taylor Hamiltonian with Taylor flux), THPF (Taylor Hamiltonian with Padé flux), EHTF (EOB Hamiltonian with Taylor flux) and EHPF (EOB Hamiltonian with Padé flux). In testing our initial data, we found that using Taylor expanded

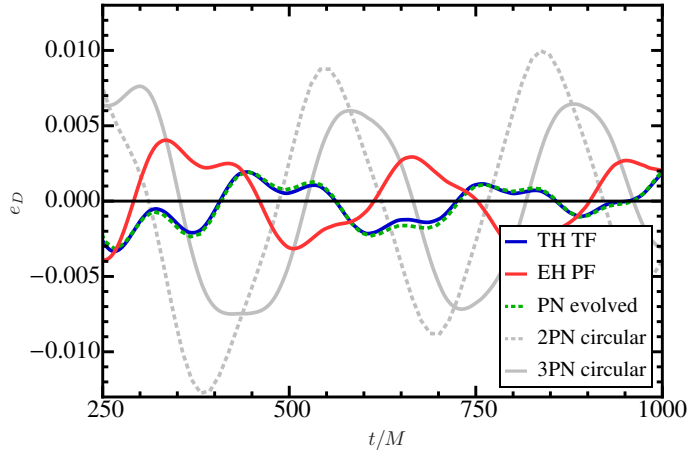


**Figure 3.3:** Measured eccentricities for initial data obtained with different methods for an equal mass, non-spinning binary initially at  $D = 11 M$ . The different initial data types THTF, EHPF, PN evolved and 3PN circular are described in the text. 2PN circular (dashed gray line) refers to the formula for  $P_t$  given in [145]. THTF and PN evolved initial data give the lowest eccentricities for this configuration.

or Padé flux gives the same results for eccentricity on the level of our measurement accuracy. From the pure numerical point of view, both flux functions are equally well suited for the production of initial data. For this reason, in the following we will only show results of the combination of one Hamiltonian with one type of flux function. At the given accuracy, the second combination gives the same result. The results (those that give the lowest eccentricities) are summarized and compared to the PN integration and PN iteration method in Tab. 3.1.

Figure 3.3 shows the results for an equal mass binary with initial separation  $D = 11 M$ . This system has been chosen in order to allow for direct comparison with the PN evolved results of [142]. We find good agreement between the eccentricity from the PN evolution method (dashed green line) and our THTF data (solid blue line). This is a good verification of our implementation since both methods use the same Hamiltonian as well as the same flux function and therefore we expect the agreement of the data. Uniquely for this system, we compare to the 2PN accurate formula for  $P_t$  [145]. A clear improvement from this data to the 3PN accurate formula (solid gray line) can be seen. The lowest eccentricity of  $e = 0.002$  is achieved by the PN evolution method or equivalently our THTF initial parameters which result in about three times lower values than the 3PN accurate formula. The EOB Hamiltonian (solid red line) does not perform as well as the Taylor Hamiltonian in this case. We

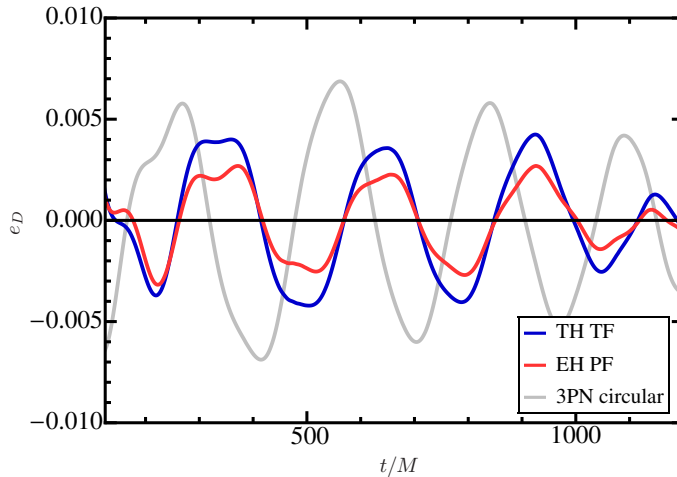


**Figure 3.4:** Eccentricities, measured using Eq. (3.15), for mass ratio 4 : 1 ( $D = 10 M$ , no spin) using initial data obtained with three different methods. The initial data types THTF, EHPF and 3PN circular are described in the text. EHPF initial data result in the lowest eccentricities.

tested our data also in a simulation with mass ratio  $q = M_1/M_2 = 2$  ( $D = 10 M$ ) and found similarly low eccentricities of  $e = 0.002$  for THTF and  $e = 0.003$  for EHTF. This is consistent with the results in [DM4] who found  $e = 0.0023$  with PN evolved initial parameters. Here, too, the variant using the Taylor Hamiltonian turns out to be superior to the EOB Hamiltonian.

This behavior is turned around in the case of mass ratio  $q = 4$ . We plot the results in Fig. 3.4. Again, we compare our two methods using Taylor or EOB Hamiltonian to the 3PN accurate formula (solid gray line) and find that both Hamiltonians succeed in reducing the eccentricity. Here, the EH data is superior to the TH one and results in an eccentricity as low as  $e = 0.003$ . This is somewhat lower than  $e = 0.0038$  found by the PN evolution method in [DM4] for the same configuration, but the values agree inside the error bounds of both results. This tendency carries over to mass ratio  $q = 10$  for which the results are displayed in Fig. 3.5. The THPF parameters here result in even higher eccentricity than the simple 3PN formula and are not plotted, while the EOB parameters produce an eccentricity of  $e = 0.002$ . This result now reinforces what in [DM1] was only a strong belief because of the lack of simulations with mass ratios larger than  $q = 4$ . The EH parameters show a clear trend to work better than TH data for increasing mass ratios. As the EOB method was originally designed in the test particle limit, it is not surprising to find that it works better for higher mass ratios than for lower ones. Another aspect is the accuracy of the

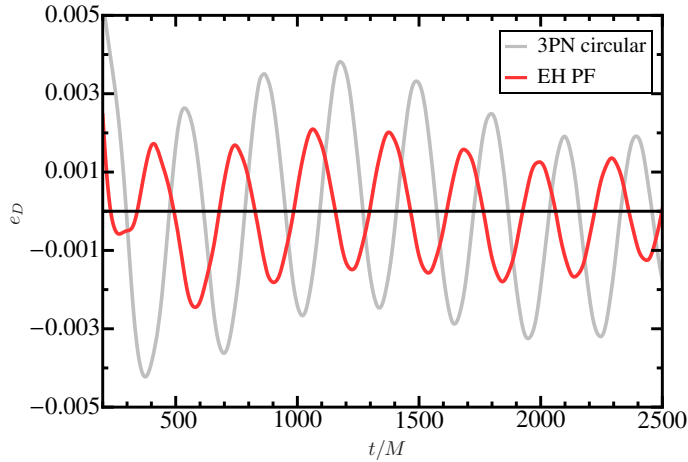


**Figure 3.5:** Eccentricity of a binary with mass ratio 10 : 1 and initial separation  $D = 10 M$  for 3PN circular (gray solid line) as well as EP initial parameters (red solid line). Equation (3.15) was used to measure the eccentricities. The 3PN circular data result in approximately two times higher eccentricity than the EHPF data.

transformation from EOB to ADMTT coordinates which becomes more accurate when the mass ratio increases [DM1], which improves the performance of the EH data, too.

### 3.5.5 Results for Spinning Binaries

In general scenarios with spins, spin–spin interaction generates physical eccentricity in the orbital motion. We saw this in the construction of our initial data in Sec. 3.5.3 where the spin–spin Hamiltonian had to be neglected in order to find truly circular orbits in the first step. As a result, we can, in general, only aim to minimize the eccentricity to the physical level when spins are present.

Adding spin to the parameter space increases the number of parameters to be studied by six. In [DM1] we therefore validated our algorithm in the subclass of binaries with equal masses and spins aligned or anti-aligned with the orbital angular momentum and equal magnitudes, only. We analyzed one example with random spin directions and magnitudes but will not draw general conclusions from this test. Still, these are astrophysically very interesting constellations because according to [152,153], isolated binary evolution and gas-rich galactic mergers are expected to lead to (anti-)aligned spins.

The amount of spurious radiation contained in our conformally flat Bowen–York

puncture initial data increases with increasing magnitude of the momentum or spin parameters in Eq. (3.6). For this reason, the physical black-hole spin which can be achieved using these data is limited to  $\chi = |\vec{S}|/M^2 = 0.929$  [120, 154, 155]. Since junk radiation affects the accuracy of the extracted waveforms by introducing noise [63], the maximum spin magnitude treated in [DM1] and [DM4] is  $\chi_i = |\vec{S}_i|/M_i^2 = 0.85$ .

As before, the configurations we tested are summarized in Tab. 3.1. We varied the spin magnitudes from  $\chi = -0.25$  to  $\chi = 0.85$  (the minus sign shows that the spins are anti-aligned with the orbital angular momentum). In all cases we found that the EOB data produce much lower eccentricity than the Taylor data. As an example, Fig. 3.6 shows the comparison between THPF (blue solid line) and EHPF (red solid line) data for  $\chi = 0.85$ . The THPF parameters result in about five times higher eccentricity than EHPF parameters. The same holds for the other spin cases we tested, and plots similar to Fig. 3.6 can be found in Fig. 7 of [DM1]. As can be seen from Tab. 3.1, our results compare quite well to the results found in [DM4] for the spinning configurations when the PN evolved data are used. Only in the case where the spin magnitude is highest,  $\chi = 0.85$ , the eccentricity of our method is three times larger than the one from PN evolved parameters. We can compare to the PN iterated data only in the case where  $\chi = -0.25$ . They result in an improvement of a factor of two compared to our data.

In the cases studied here, with spins parallel to the orbital angular momentum, the spin-spin Hamiltonian  $H_{SS}$  (Eq. (A.14)) reduces to a spherically symmetric one,  $H_{SS} = \text{const} \cdot R^{-3}$ , and spin precession is absent. Therefore, for the cases we studied it is still possible to find spherical orbits in the solution of Eq. (3.18) even when  $H_{SS}$  is included [156]. We explored the consequences on the eccentricity when including this term for the case where  $\chi = 0.85$ . The results are shown as dashed lines in Fig. 3.6. While the result does not much improve for the TH data, the eccentricity is reduced by a factor of two down to  $e = 0.007$  for the EH data and becomes comparable to the result from the PN evolved method.

In the scope of the Numerical Relativity and Analytical Relativity (NRAR) collaboration [157], we simulated a configuration of unequal mass black holes with spins pointing along the orbital angular momentum but opposite to each other, such that the total spin  $\vec{S} = \vec{S}_1 + \vec{S}_2$  vanishes. The mass ratio was  $q = 2$  and the initial separation was chosen to be  $D = 10M$ , the  $z$ -components of the spins were  $S_{z,i} = \pm 0.067M^2$ . The grid configuration is given in the third line of Tab. 3.2, la-

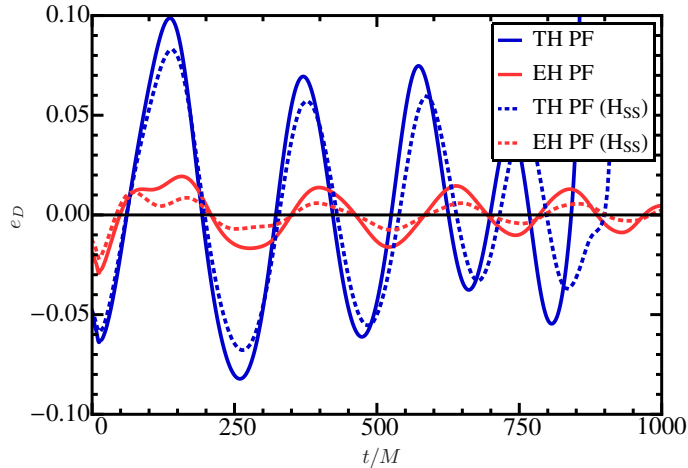


**Figure 3.6:** Eccentricity for an equal mass binary with equal spins ( $\chi = 0.85$ ) which are aligned to the orbital angular momentum. Compared are TH (blue solid) and EH (red solid) data as well as the same including spin–spin coupling (dashed lines). EHPF data with spin–spin coupling minimize the eccentricity.

belled as  $q = 2_{\text{NRAR}}$ . More properties of this special configuration are summarized in Sec. 5.2. This gives us the possibility to verify our initial parameters in a more general situation than those presented in [DM1]. The resulting eccentricity as a function of coordinate time using EHPF initial data is shown in Fig. 3.7. The eccentricity of this configuration is  $e = 0.002$  and is as low as the value we obtained for  $q = 2$  when the black holes were not spinning. The data therefore works also well in this case.

Given all the simplifications we applied, the EOB data performs remarkably well in most of the cases we have studied. We had to do a coordinate transformation from EOB to ADMTT coordinates, which is only known to 3PN order. Furthermore, we applied the transformation only to the orbital Hamiltonian and not to the spin part. For the spin cases, we omitted the spin–spin coupling terms (regardless of the orbital Hamiltonian we employed) except for one configuration. Another point, which is a valid objection also when using the Taylor expanded Hamiltonian, is the difference between ADMTT and the numerical coordinates in the initial slice. In a recent work [144] the authors even argue that due to this difference, all reduction in eccentricity obtained with the above TH, EH or PN integration method are by chance, and one can use much simpler methods to reduce the eccentricity. They, for example, start with 2PN exact values of  $P_t$  and  $P_r$  in harmonic gauge [146] and refine  $P_t$  using low resolution numerical simulations of the first orbits. The amount

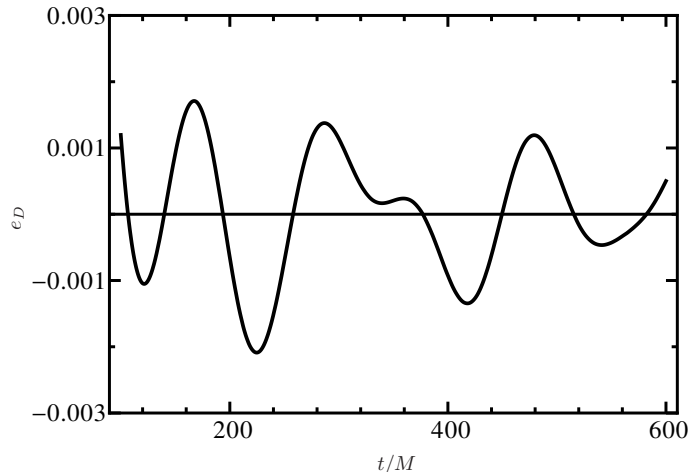


**Figure 3.7:** Eccentricity over coordinate time for a binary with mass ratio 2 : 1 and vanishing total spin,  $S_{z,i} = \pm 0.067M^2$ . The initial separation is  $D = 10M$ . The eccentricity shown here is obtained with EHPF data.

of change in  $P_{\dot{t}}$  in each iteration step is determined by a simple fitting formula. This way, the authors of [144] are able to obtain low eccentricity initial parameters for spinning and non-spinning configurations, too. We believe, however, that the use of more theoretically motivated initial parameters is a legitimate approach although the method inherits certain simplifications. The points mentioned above leave some room for development, and as the example with  $H_{\text{SS}}$  included shows, the data can be improved, and we do not believe this to happen by accident.

The method could be further improved by using more sophisticated Hamiltonians. As discussed in [DM4], including NLO spin terms improves the results. For the EOB version of the algorithm, the latest and, according to the authors, most accurate orbital Hamiltonian can be found in [158] and could give lower eccentricities. Additionally, there are methods to include spin in the EOB formalism [156] which are potentially more correct but where spin-orbit and spin-spin coupling terms are mixed such that we could not easily neglect spin-spin terms for the sake of finding circular orbits in the first step of our algorithm. Recently, a different method to reduce eccentricity in precessing spin configurations has been proposed in [159].





## 4 Increasing the Mass Ratio in Finite Difference Simulations

While initial simulations covered the parameter space of binaries with equal masses, a key part of studying black holes in quasi-circular orbits is to simulate binaries with intermediate mass ratios. This is because unequal mass black hole binary mergers are expected to be very common events in our universe. Studies show that the mass ratio at which supermassive black hole mergers are most likely to occur lie between  $3 \leq q \leq 100$  [20–22]. We therefore expect to find at least a few of those events per year to be detected by GW detectors.

The event rate of detecting signals from intermediate mass black hole binary mergers with intermediate mass ratio will probably be less than one per year for the Advanced Laser Interferometer Gravitational Wave Observatory (LIGO), but the Einstein Telescope should see a few events per year [160]. Depending on the cosmological model used, the event rates of unequal mass supermassive black hole mergers in the Universe varies between less than one to about ten per year [161]. For LISA, we therefore expect a few events per year [162] with a very high signal-to-noise ratio (even for pessimistic assumptions we should still see a few events during the lifetime of the LISA mission). Whereas for ground-based detectors, templates of unequal mass binaries will be needed for detection via matched filtering, for LISA we mainly need accurate templates for parameter estimation purposes, since the signal will be much stronger than the noise [3]. In order to build such templates, accurate simulations of the merger phase are needed.

In principle, the mass ratio does not have to be arbitrarily high. Very high mass ratios can be treated approximately, for example using the results from self-force and perturbative calculations (see [23, 24] for reviews and references therein) solving Teukolsky’s equation [163–165]. The predictions of approximative methods need to be compared to numerical results, and in order to make clear statements about

their agreement or disagreement, we again need the numerical waveform to be highly accurate.

The present chapter deals with the complications a mass ratio different from one introduces in puncture simulations. First, the computational cost increases dramatically and secondly, we have to deal with an instability.

## 4.1 Increase in Computational Cost

When calculating equal mass binaries in quasi-circular orbits, we need to simulate only one quadrant of the whole domain and obtain the missing parts by symmetry. For unequal masses, this is no longer true. Here, half of the domain has to be evaluated (bitant symmetry). Therefore, unequal mass simulations naturally are more expensive than equal mass ones if the same accuracy is to be achieved. Additionally, the computational cost increases with mass ratio, which will be seen by the following estimate. In finite difference methods the time step  $\Delta t$  is connected to the spatial resolution  $\Delta x$  by the Courant factor  $C$ ,  $\Delta t = C\Delta x$ . In the BAM code,  $C \leq 0.5$  is used. The smaller black hole with mass  $M_1$  determines which spatial resolution  $\Delta x$  is needed. Basically, the resolution needs to be sufficiently high in order to resolve the small black hole appropriately. The time step  $\Delta t$  is therefore determined by the smaller mass. The coordinate time to complete one orbit is, however, connected to the total mass  $M$  of the system. A rough estimate for the dependence of the number of time steps needed to complete one orbit on the mass ratio  $q$  can be obtained by the following considerations. Through the distance  $D$ ,  $M$  determines the orbital time,  $T \sim M$ . On the other hand, one orbit is completed after  $k$  time steps,  $T = k\Delta t$ . The number of time steps to complete one orbit can therefore be estimated to  $k = T/\Delta t \sim M/M_1 = 1 + q$ . See for example [166] for the difference in time to complete a simulation with  $q = 10$  and  $q = 15$ .

Additionally, the spatial grid configuration, and especially the outer boundary, is supposed to not change in terms of  $M$  in order to achieve the same accuracy for different  $M$ . As in the previous considerations about the number of time steps, the spatial resolution is determined by  $M_1$ , but the box size is given in  $M$ . Given three spatial dimensions, the number of points needed depends on the mass ratio as  $N \sim (1 + q)^3$ . This means that not only the simulation takes longer because it has to perform more time steps, but it also becomes slower because more points have to

be evaluated for increasing mass ratio.

Another aspect slows down high mass ratio simulations if the accuracy is not to be reduced compared to smaller mass ratios. Because of the longer computation, the phase accuracy has to be maintained over a longer amount of time. This can only be achieved by reducing the spatial resolution  $\Delta x$  (in terms of  $M$ ) because the phase error continues to add up over the course of a simulation. In summary, simulations do not become computationally more expensive linearly with increasing mass ratios. To maintain a certain level of accuracy, the increase in computational cost is roughly proportional to at least  $(1 + q)^4$ . In practice, runs with mass ratio  $q = 4$  are already expensive enough that their accuracy does not reach the one of equal mass simulations, yet.

## 4.2 Gamma Driver Revisited

Increasing the mass ratio not only increases the computational cost of a numerical simulation, but also faces us with a stability problem. In the publication of the first simulations of mass ratio  $q = 10$  [78], the authors explicitly noted that the stability of the simulation is sensitive to the damping factor,  $\eta$ , used in the gamma driver condition Eq. (2.19). Because this equation forms the basis of the investigations following in this chapter, we recall it here,

$$\partial_0^2 \beta^i = \frac{3}{4} \partial_0 \tilde{\Gamma}^i - \eta \partial_0 \beta^i. \quad (4.1)$$

In the first proposition for a gamma driver shift condition [53], the second term on the RHS of Eq. (4.1) was absent. In [44], the damping term was added in order to reduce oscillations in the shift vector. Adjusting the magnitude of the damping coefficient  $\eta$  was found to allow for freezing of the evolution at late times in [45] and to avoid drifts in metric variables in [61]. Furthermore, the coordinate location of the apparent horizon, related to the effective resolution of the black hole on the numerical grid, showed a dependence on the value of  $\eta$  in [61, 167]. These findings reveal how important the choice of the damping value is if one wants to resolve the black hole properly while still driving the coordinates to a frame where they are stationary when the physical situation is stationary and hence obtain a long term stable evolution. If the damping parameter is either too small or too large, unwanted oscillations disturb

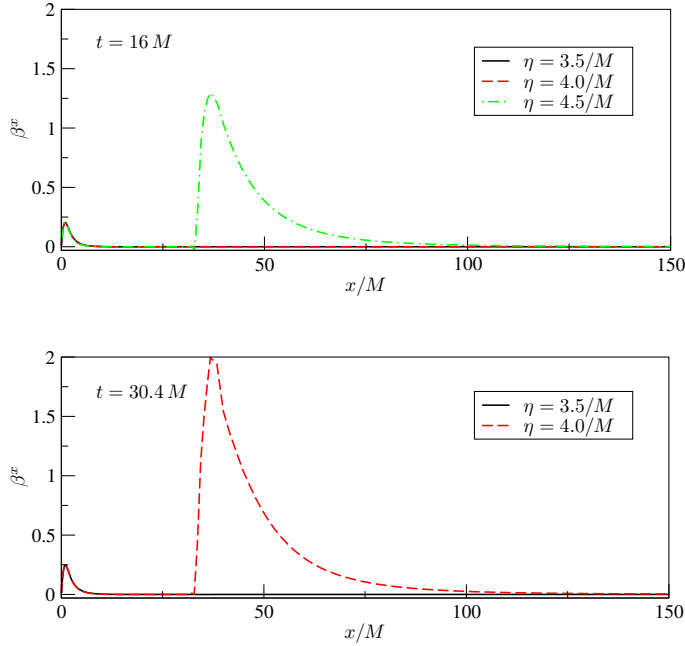


**Figure 4.1:** The  $x$ -component of the shift vector in  $x$ -direction for a single non-spinning puncture of mass  $M$  at times  $t = 16.0 M$  and  $t = 30.4 M$ . The three different lines mark three values of the damping constant  $\eta$ . The solid line (black) is for  $\eta = 3.5/M$ , the dashed line (red) for  $\eta = 4.0/M$  and the dotted-dashed line (green) for  $\eta = 4.5/M$ . At  $t = 16 M$ , the simulation using  $\eta = 4.5/M$  develops an instability in the shift vector and fails soon afterward, the same happens for  $\eta = 4.0/M$  at  $t = 30.4 M$ . In the simulation using  $\eta = 3.5$ , no such instability develops.

the simulation or a coordinate instability causes it to fail, respectively.

The standard choice is to set  $\eta$  to some constant on the entire numerical grid. As can be seen from Eq. (4.1), it has units of inverse mass,  $1/M$ . The interval of suitable values for  $\eta$  can be explored with simulations of a single black hole with mass  $M$ . Damping of a coordinate wave in the shift vector is very efficient and can be obtained with values of the damping coefficient on the order of one. The effect of increasing its magnitude is shown in Fig. 4.1 where the  $x$ -component of the shift vector is plotted in  $x$ -direction at two different times during the evolution of a single, non-spinning puncture. The different colors and line types stand for different values of  $\eta$ . The higher its magnitude, the earlier an instability grows and spoils the result. For  $\eta = 4.5/M$  (green dotted-dashed line), the simulation fails after a time  $t = 16 M$  and for  $\eta = 4.0/M$  (red dashed line), this is the case after about  $t = 30 M$ . For  $\eta = 3.5/M$ , no such instability develops and the simulation is stable for hundreds of  $M$ . By itself, this observation is not new, see e.g. [57, 61, 67, 168]. This leads to the empirical result that  $0 < \eta \lesssim 3.5/M$  is necessary for stable simulations of a single

puncture with a courant factor of 0.5 and the typical box configurations used in BAM.

Based on the conclusions for a single puncture, in binary simulations a typical choice is  $\eta \simeq 2/M$ , with  $M = M_1 + M_2$  the total mass of the system. This works well even for the most demanding simulations as long as the mass ratio is sufficiently close to unity. This choice, however, leads to the aforementioned instability for the mass ratio 10 : 1 simulation in [78]. Stability was obtained for  $\eta = 1.375/M$  in this simulation.

The key issue for unequal masses is that a constant  $\eta$  cannot equally well accommodate both black holes. A constant damping parameter implies that the effective damping near each black hole (in terms of the individual black hole mass) is asymmetric. Ideally,  $\eta$  should be  $\approx 1/M_i$  for a puncture with mass  $M_i$ , which cannot be accomplished simultaneously for unequal masses using a constant value of  $\eta = 2/M$ . For high mass ratios, this asymmetry in the grid can be large enough to lead to a failure of the simulations because the damping may become too large or too small for one of the black holes. To cure this problem, we use a position-dependent damping parameter that adapts to the local mass. In particular, we want it to vary such that, in the vicinity of the  $i^{\text{th}}$  puncture with mass  $M_i$ , its value approaches  $1/M_i$ .

A position-dependent  $\eta$  was already considered when the Gamma driver condition was introduced [45, 78, 169–171], but such constructions were not pursued further because for moderate mass ratios a constant  $\eta$  works well. In [169] a position-dependent formula was introduced for head-on collisions of black holes, which to our knowledge was only used in one other publication [170], prior to the moving puncture framework.

An attempt to explain the origin of the instability described above was made recently in [168] and is summarized in the following. In a homogeneous spacetime,  $\tilde{\Gamma}^i = -\partial_j \tilde{\gamma}^{ij} = 0$  and therefore, Eq. (4.1) reduces to  $\partial_0^2 \beta^i = -\eta \partial_0 \beta^i$  or  $\partial_0 \beta^i = -\eta \beta^i$  (because we set  $\beta^i(t=0) = 0$ ). Because of the stiffness of this equation, we obtain a necessary condition on  $\eta$  and the numerical timestep  $\Delta t$  for stability of a Runge–Kutta method with a stability region containing the semi circle  $\mathcal{B}_{\bar{Q}} = \{\xi \in \mathbb{C}^- : |\xi| \leq Q\}$ ,

$$\Delta t < \frac{Q}{\eta}. \quad (4.2)$$

$Q$  is a constant depending on the numerical method used for evolution and  $Q = 2.615$  for our RK4 (see e.g. [172]). This is a stability condition which, other than the CFL condition (which needs to be satisfied as well), does not depend on the spatial

resolution  $\Delta x$ . In simulations with mesh refinement and Berger–Olinger time stepping where the time step increases towards outer regions it can happen that condition (4.2) is not satisfied everywhere on the numerical grid. In the outer boxes,  $\Delta t$  might be too large for certain box configurations. This explanation is supported by the finding of e.g. [61] that turning off Berger–Olinger time stepping on the outer boxes or by [67] that halving the value of  $\eta$  there cures the instability. Furthermore, decreasing the courant factor (which globally decreases  $\Delta t$ ) in the simulations used to produce Fig. 4.1 showed that we can also obtain stable simulations for some of the values of  $\eta$  which failed previously. Care has to be taken on the fact that a homogeneous spacetime is assumed for the derivation of the preceding argument. Therefore, it can only hold approximately and very far away from the black holes, and Eq. (4.2) is to be regarded as a rather vague criterion for stability. However, the conclusion the author of [168] draws from these considerations is the same as ours, namely, that a position–dependent damping parameter  $\eta$  is needed which accounts for the variations in the time step on the grid.

In the following sections, our ideas on how to construct a dynamical damping parameter will be presented and it will be discussed how they perform in numerical simulations. We were the first to use a position–dependent damping parameter in black hole binary simulations in quasi–circular orbits and, as we will see, one of our constructions paved the way for simulations of mass ratios larger than  $q = 10$ .

### 4.3 Using the Conformal Factor for Dynamical Damping

We ask for a definition of  $\eta$  which asymptotes to specifiable values at the location of the punctures and at infinity. As stated before, typical values are  $\eta = 1/M_i$  at the  $i^{\text{th}}$  black hole and  $\eta = 2/M$  at large distances.

Since we use the BSSN system of Einstein’s equations (see Sec. 2.2), a first idea is to construct an  $\eta$  which depends only on the BSSN variables. In order to preserve the strong hyperbolicity of the BSSN system in conjunction with 1+log slicing and the Gamma driver shift, we have to construct the formula in a way that does not change the principal part of the differential operators.

Because we need information about the position and masses of the punctures, the

conformal factor  $\psi$  lends itself for a construction of  $\eta$  with the requirements described above.

In [DM2] we therefore set up

$$\eta(\vec{r}) = \hat{R}_0 \frac{\sqrt{\tilde{\gamma}^{ij} \partial_i \psi^{-2} \partial_j \psi^{-2}}}{(1 - \psi^{-2})^2}, \quad (4.3)$$

with  $\tilde{\gamma}^{ij}$  the inverse of the conformal 3-metric and  $\hat{R}_0$  a dimensionless constant. While  $\psi$ ,  $\tilde{\gamma}^{ij}$ , and  $\hat{R}_0$  are dimensionless, the partial derivative introduces the appropriate dependence on the mass since  $\partial_i \sim 1/M$  and hence  $\eta(\vec{r}) \sim 1/M$ . Equation (4.3) does not affect the principal part of Eq. (4.1) and therefore the whole system remains strongly hyperbolic, same as for  $\eta = \text{const.}$  according to [58, 59].

We can now check the limits of Eq. (4.3) near the puncture and near the outer boundary of the grid. For a single puncture and to leading order, the asymptotic behavior of the conformal factor near the puncture ( $r \rightarrow 0$ ) is

$$\psi^{-2} \simeq p_1 r, \quad (4.4)$$

with  $\frac{1}{p_1} = R_0 = \lim_{r \rightarrow 0} \psi^2 r = \hat{R}_0 M$  and the numerical result  $\hat{R}_0 \approx 1.31$  [117]. The next to leading order behavior is less simple [173]. Because the inverse of the conformal metric behaves like  $\tilde{\gamma}^{ij} \simeq \delta^{ij}$  for small radii, we have

$$\sqrt{\tilde{\gamma}^{ij} \partial_i \psi^{-2} \partial_j \psi^{-2}} \simeq p_1 = \frac{1}{\hat{R}_0 M} \quad (4.5)$$

and

$$(1 - \psi^{-2})^2 \simeq (1 - p_1 r)^2 \simeq 1 - 2p_1 r \quad (4.6)$$

when keeping only leading order terms in  $r$ . Using Eqns. (4.5) and (4.6) in  $\eta(\vec{r})$  leads to

$$\eta(r = 0) = 1/M. \quad (4.7)$$

A similar analysis can be done for large radii. In this case, the conformal factor asymptotes to

$$\psi^{-2} \simeq \left(1 + \frac{M}{2r}\right)^{-2} \simeq 1 - \frac{M}{r}, \quad (4.8)$$

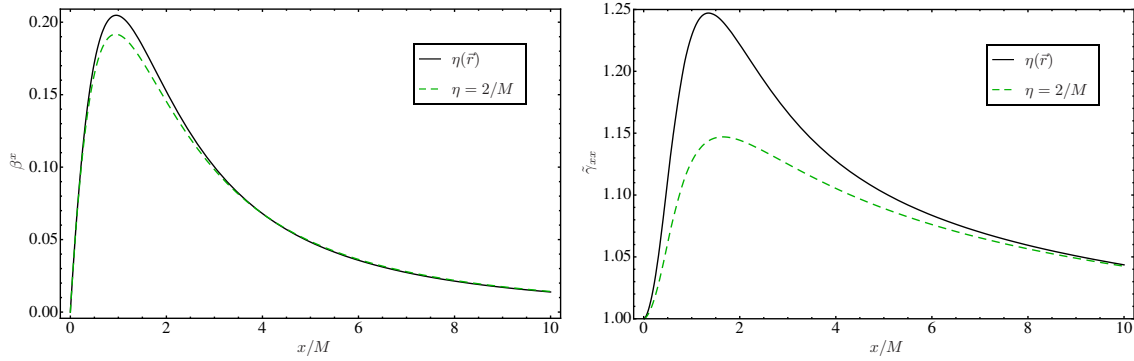


**Figure 4.2:**  $x$ -component of the shift vector (left plot) and  $xx$ -component of the conformal 3-metric (right plot) in  $x$ -direction for a single, non-spinning puncture at time  $t = 100M$ , where the simulations have reached a stationary state. The solid black curves use dynamical damping, Eq. (4.3), the dashed green ones use  $\eta = 2.0/M$  in the shift condition Eq. (4.1).

resulting in

$$\sqrt{\tilde{\gamma}^{ij}\partial_i\psi^{-2}\partial_j\psi^{-2}} \simeq \frac{M}{r^2}, \quad (4.9)$$

and

$$\eta(r \rightarrow \infty) \simeq \hat{R}_0 \frac{M/r^2}{(M/r)^2} = \frac{\hat{R}_0}{M}. \quad (4.10)$$

Equation (4.3) thus shows the desired limits near the puncture and at large distance from the puncture. The factor of  $\hat{R}_0$  can be tolerated without difficulty.

### 4.3.1 Adapted Damping in Single Black Hole Simulations

Because using Eq. (4.3) instead of  $\eta = 2/M$  alters the shift condition Eq. (4.1), the shift itself will look different. The resulting  $x$ -components of the shift vector for using  $\eta = 2.0/M$  or  $\eta(\vec{r})$  are compared in the left plot of Fig. 4.2 for a single, non-spinning puncture. Also, we will see a change in coordinate dependent quantities because a modified shift leads to a modification in the coordinates. As an example, the  $xx$ -component of the conformal 3-metric,  $\tilde{\gamma}_{xx}$ , is compared for  $\eta = 2.0/M$  and  $\eta(\vec{r})$  in the right panel of Fig. 4.2. Both plots show the results at time  $t = 100M$ , when the simulations have reached a stationary state.

As the shift vector is a gauge function, its changes are supposed to introduce only coordinate changes. While this is true analytically, it has to be verified for the numerical results. Figure 4.3 shows the lapse  $\alpha$  as a function of the trace of the extrinsic curvature,  $K$ . Both quantities are scalars and should see the same coordinate



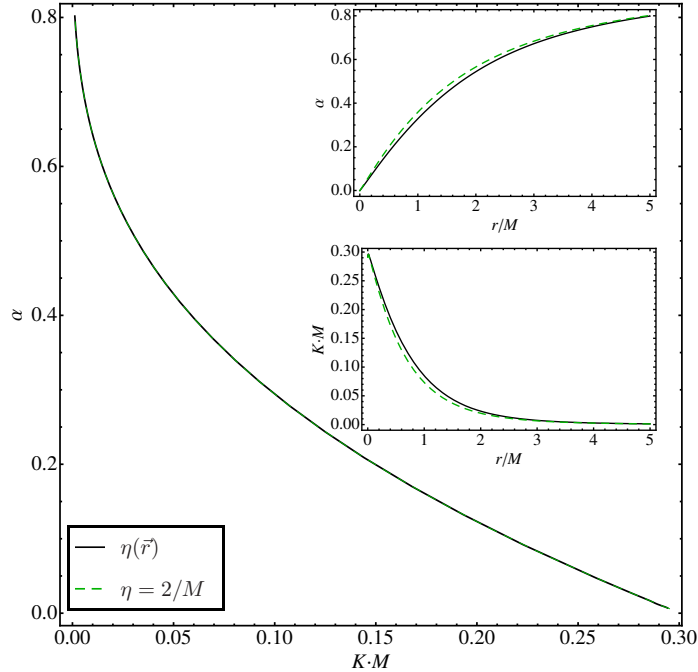


**Figure 4.3:** The lapse function  $\alpha$  as a function of the trace of the extrinsic curvature  $K$  for a single, non-spinning and non-moving puncture after a time  $t = 50 M$ . We compare using  $\eta(\vec{r})$  (black, solid line) and  $\eta = 2.0/M$  (green, dashed line). The two curves  $\alpha(K)$  for the different methods lie almost exactly on top of each other. The insets show lapse (upper panel) and extrinsic curvature (lower panel) as functions of radial distance  $r$  from the puncture, revealing some differences for the two methods due to differences in the radial coordinate.

drifts. Therefore, we expect the function  $\alpha(K)$  to be invariant of the shift vector if it indeed only alters the coordinates. Figure 4.3 confirms this expectation. The two curves for  $\eta = 2.0/M$  (dashed green curve) and  $\eta(\vec{r})$  (solid black curve) lie, for the scale of the plot, almost exactly on top of each other. We therefore confidently believe that using the dynamical damping introduces only coordinate changes in our puncture simulations.

### 4.3.2 Adapted Damping in Binary Simulations

For data analysis purposes, we are mainly interested in the properties of the emitted gravitational waves of the black hole binary systems under study. Hence, it is important to check how the changes in the gauge alter the extracted gravitational waves. Since  $\Psi_4$  is only first-order gauge invariant and we furthermore extract waves at a finite, fixed coordinate radius, it is a priori an open question how much the changes in the shift affect the waveforms. Although the last point can be partly

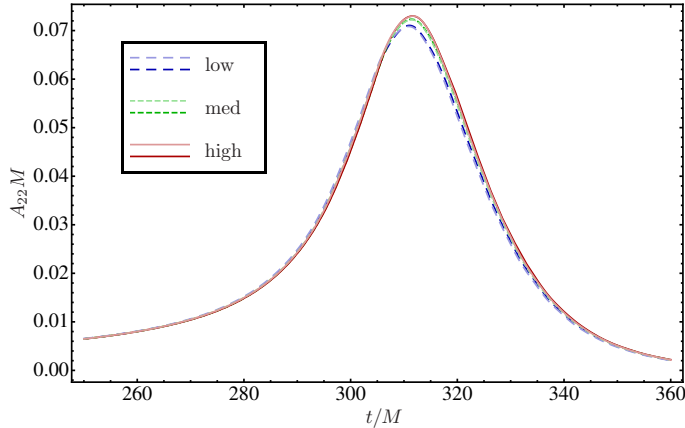


**Figure 4.4:** Comparison between the amplitudes of the 22–mode of  $\Psi_4$  for  $q = 1$  and  $D = 7M$  in three different resolutions (low, medium and high, see text in Sec. 4.3.2) using either Eq. (4.3) (vivid colors) or  $\eta = 2/M$  (pale colors). The difference between runs with different versions of  $\eta$  but the same resolution is nearly invisible.

addressed by extrapolation of  $R_{\text{ex}} \rightarrow \infty$ , it is not clear how much a change of coordinates affects the gravitational waves. Furthermore, a change of coordinates implies an effective change of the numerical resolution, and for practical purposes we have to ask how much waveforms differ at a given finite resolution. To this end, we look at the 22–mode of  $\Psi_4$  in a simulation of an equal mass binary without initial spins and at initial separation  $D = 7M$  so that the binary completes about three orbits prior to merger. We use three grid configurations with increasing resolution so that we can see how  $\Psi_4$  behaves in a convergence analysis. The grid configurations are  $\phi[5 \times N : 5 \times 2N : 6 : 48N/72 : 0.5]$  with  $N \in \{56, 64, 72\}$  ( $N = 56$  labelled “low”,  $N = 64$  labelled “med” and  $N = 72$  labelled “high”). See Sec. 2.6 for an explanation of the notation for the grid configurations.

We get a first impression of the results from Fig. 4.4 showing the amplitudes of the 22–mode of  $\Psi_4$  extracted at  $R_{\text{ex}} = 90M$ . In light colors, the results for  $\eta = 2/M$  are plotted, dark colors are used for the results obtained with Eq. (4.3). Different line types show different resolutions. The results from different gauges are very close to each other. These differences will be quantified in the following. In the left panel of Fig. 4.5, the relative difference in amplitudes (of the 22–mode of  $\Psi_4$ ) between using  $\eta = 2/M$  and Eq. (4.3) is plotted. There are three curves, each one corresponds to one of the different resolutions. For comparison, in the right panel of this figure we keep the gauge fixed and plot the relative difference between the amplitudes in

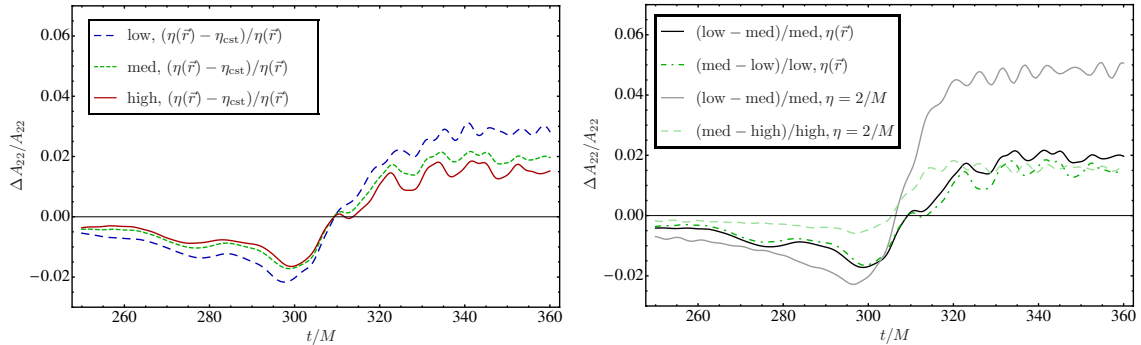


**Figure 4.5:** Relative amplitude error of the 22–mode for  $q = 1$ ,  $D = 7M$ . The left panel shows the relative deviation between the amplitude in the standard ( $\eta_{\text{cst.}} = 2.0/M$ ) and in the dynamical gauge (Eq. (4.3)). Each curve shows a different resolution, see text in Sec. 4.3.2 for the labelling. The differences decrease with increasing resolution. For comparison, in the right panel we fix the gauge and compute the relative errors between low and medium (solid black and dot–dashed green) as well as medium and high (solid gray and dashed light green) resolutions.

low and medium and medium and high resolution. In the left panel, we observe a non–vanishing difference between the gauge choices which, however, decreases with increase in resolution. The comparison with the plot on the right hand side gives insight on the size of the differences. Changing from  $\eta = 2/M$  to dynamical damping, Eq. (4.3), varies the amplitude at the size of the changes we introduce by varying the numerical resolution. The phase error  $\Delta\phi$  is analyzed accordingly in Fig. 4.6. Again, the left plot shows the differences in phase between the results obtained with  $\eta = 2/M$  and Eq. (4.3) for fixed resolutions. As for the amplitudes, the phase differences decrease with increasing resolution. The plot on the right hand side of Fig. 4.6 compares the phase errors between resolutions for the two types of  $\eta$  we use. The phase error between low and medium resolution is continuously lower for  $\eta(\vec{r})$  than for the constant  $\eta$  case (compare the solid black line for Eq. (4.3) and the solid gray line for  $\eta = 2/M$ ). This is also true for the differences between medium and high resolution (the dashed dark green for Eq. (4.3) and the dashed light green line for  $\eta = 2/M$ ). Comparing the left plot to the right one, we see that the phase deviations introduced by using the different dampings is on the size of the ones we get by changing the resolution.

The analysis affirms that differences in the waveforms for the equal mass binary are small and, most importantly, vanish with increase in resolution. In [DM2] we found that the same is true for a binary with mass ratio  $q = 4$  and initial separation  $D = 5M$  where we used the grid configurations  $\phi[5 \times N : 7 \times 2N : 6 : 120N/72 : 0.5]$

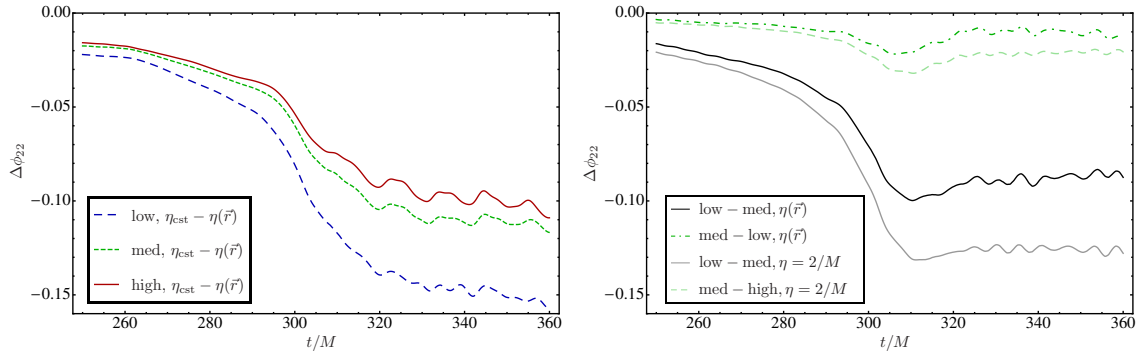


**Figure 4.6:** Phase error of the 22-mode for  $q = 1$ ,  $D = 7M$ . In the left panel, we plot the differences between the runs using constant damping ( $\eta_{\text{cst.}} = 2.0/M$ ) and adapted damping (Eq. (4.3)) for three resolutions described in the text of Sec. 4.3.2. Again, the differences decrease with increasing resolution. The right panel shows the phase differences between low and medium (solid gray and dashed light green lines) and medium and high (solid black and dot-dashed dark green lines) resolutions when the gauge (either dynamical or constant damping) is fixed.

with  $N \in \{72, 80\}$ .

An interesting question in this context is how Eq. (4.3) behaves for two punctures with different masses. The analytic limits Eqns. (4.7) and (4.10) were deduced for a single, non-moving, stationary puncture. Now we are using it for two moving punctures, which are during most of the simulations far from having reached a stationary state globally, but which are approximately stationary locally at the punctures. Figure 4.7 illustrates the distribution of  $\eta(\vec{r})$  along a straight coordinate line through both punctures. To indicate the puncture locations, the conformal factor  $\phi = \ln \psi$ , which has maxima (the divergences are not resolved) approximately at the positions of the punctures, is also plotted. The snapshot is taken at time  $t = 22.2M$  during the simulation when the punctures are still separate, but the gauge has evolved from the initial data to the moving puncture gauge that we want to study. Following Eq. (4.7), we expect to find  $\eta(\vec{r}) \simeq 1/M_1 = 5/M$  near the puncture with mass  $M_1 = 0.2M$  and  $\eta(\vec{r}) \simeq 1/M_2 = 1.25/M$  in the vicinity of the second puncture with  $M_2 = 0.8M$ . Near the outer boundary,  $\eta(\vec{r})$  is supposed to take the value  $1.31/(M_1 + M_2) = 1.31/M$  according to Eq. (4.10). Figure 4.7 confirms that we do obtain the expected values, although they are not reached exactly. The latter is not a problem as simulations work nicely as long as  $\eta(\vec{r})$  is in the right range for each black hole. For this reason, Fig. 4.7 confirms that the limits of Eq. (4.3) also work for two punctures with unequal masses.

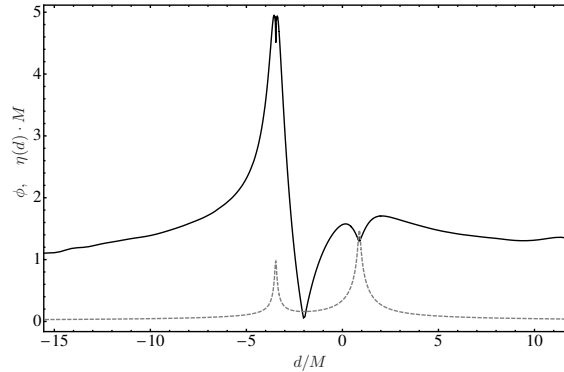


**Figure 4.7:** Distribution of  $\eta(\vec{r})$ , Eq. (4.3), (black, solid line) for two punctures of bare masses  $M_1 = 0.2M$  and  $M_2 = 0.8M$ , and the conformal factor  $\phi$  (gray, dashed line), whose maxima show the current positions of the punctures, plotted along the straight coordinate line  $d$  through both punctures. The snapshot is taken after an evolution time of  $22M$ . The mass ratio is  $q = 4$  in this simulation with initial separation  $D = 5M$ . The smaller black hole is at position  $d = -3.6M$ , the larger one at position  $d = 1.2M$ .  $\eta(\vec{r})$  approximately takes the expected values  $1/M_i$  at the  $i^{\text{th}}$  puncture and approaches  $1/M$  away from the punctures.

### 4.3.3 Behavior in Long-Term Simulations and Ameliorations

Despite all the positive findings of the precedent paragraphs, Eq. (4.3) provides reason for concern. Looking at the long-term behavior of  $\eta(\vec{r})$  we find strong distortions. Representative for all runs, those are plotted in one coordinate direction in Fig. 4.8 for the equal mass simulation of last section.

As can be seen, noise travels out from the origin as time progresses. This leaves steady features on the form of  $\eta$  which could spike to higher and lower values than the range determined before. Additionally, they may lead to unpredictable coordinate drifts and could, in some cases, affect the long-term stability of the simulation although the oscillations in  $\eta(\vec{r})$  do not translate to oscillations in the shift vector.

To illuminate the origin of the disturbances in  $\eta(\vec{r})$ , in [DM3] we looked at the development of  $\eta(\vec{r})$  in simulations of a single, non-spinning puncture, and a single, spinning puncture with spin magnitude  $S_z/M^2 = 0.25$ . The result for the spinning case is plotted in Fig. 4.9 at two different times over the  $x$ -axis. In both cases, we see the outwards traveling pulse moving at speed 1.39 (in our geometric units where  $c = G = 1$ ). In the single puncture simulations, the pulse does not leave much noise on the grid as it does for the binary in Fig. 4.8. The superluminal speed we found indicates that the pulse is related to the gauge modes traveling at speed  $v_{\alpha \simeq 1} = \sqrt{2}$  in the asymptotic region where the lapse  $\alpha \simeq 1$ , see [59] and [45] for a discussion

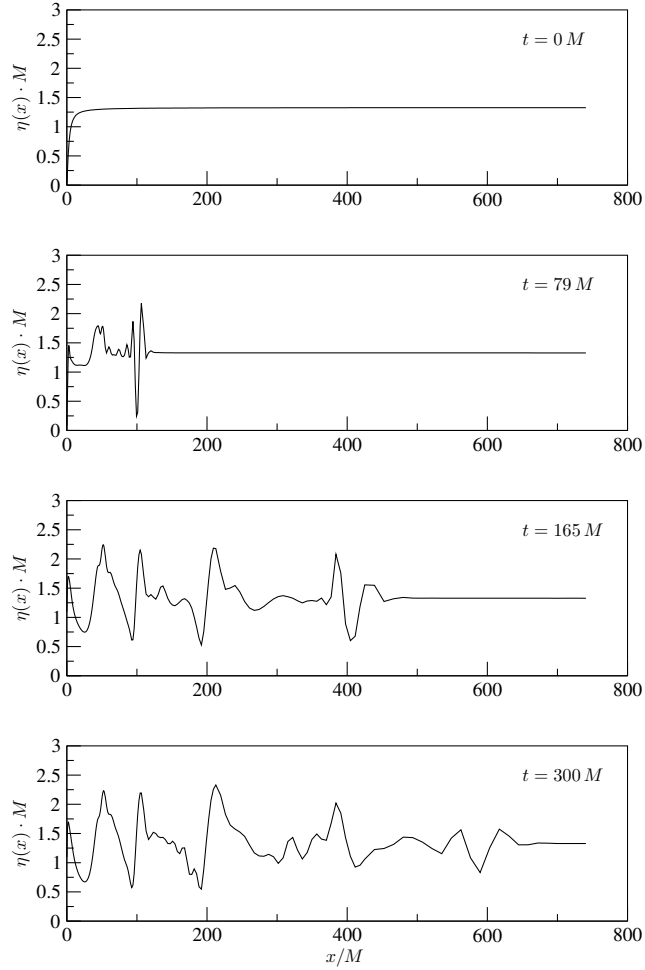


**Figure 4.8:** Damping factor,  $\eta(x)$ , along the  $x$ -axis using Eq. (4.3). The simulated configuration is an equal mass binary with initial separation  $D = 7 M$  and orbits lying in the  $(x, y)$ -plane. Shown are four different times during the simulation. With time, noise travels outwards, leaving steady disturbances on the grid.

of gauge speeds and Sec. 2.3.1. In contrast to gauge pulses in the lapse,  $\alpha$ , or shift vector,  $\beta^i$ , the pulse in  $\eta(x)$  is amplified as it walks out. We believe the reason for this behavior is that as the distance to the puncture increases, the conformal factor,  $\psi$ , gets closer to unity. Therefore, the denominator in Eq. (4.3) approaches zero, and the gauge disturbances in the derivatives of  $\psi$  are magnified. We further observed reflections at the refinement boundaries as this pulse passes through them. This may explain the fluctuations in  $\eta(x)$  shown in Fig. 4.8.

While we turned in a different direction to determine the form of the damping parameter (see Sec. 4.4), the authors of [25, 166, 174] continued to fine-tune our

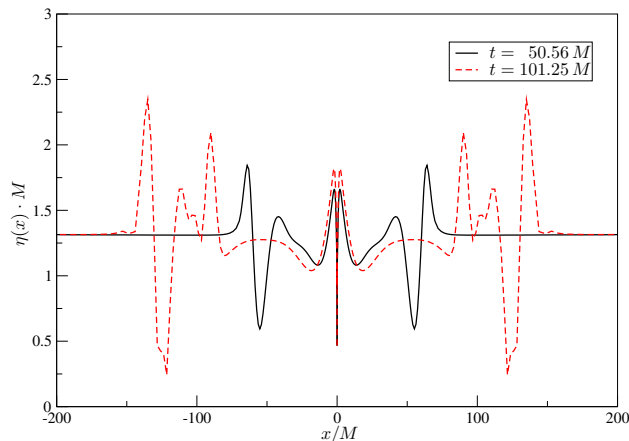


**Figure 4.9:** Form of  $\eta(\vec{r})$  for a single spinning puncture sitting at  $x = 0$  using Eq. (4.3) after simulation time  $t = 50.56 M$  (solid black line) and  $t = 101.25 M$  (dashed red line) in  $x$ -direction. An outward traveling pulse, which is amplified, can be seen.

Eq. (4.3) to deal with these problems. In our notation they used

$$\eta(\vec{r}, t) = \hat{R}_0 \frac{\sqrt{\tilde{\gamma}^{ij} \partial_i \psi^{-2} \partial_j \psi^{-2}}}{(1 - \psi^{-2a})^b}. \quad (4.11)$$

For  $a = 1$  and  $b = 2$ , we recover Eq. (4.3), but they used  $a = 2$  and  $b = 2$  which, according to [175], leads to a minimum of noise in  $\eta(\vec{r})$ . With this choice, the asymptotic value of Eq. (4.11) near the puncture is  $\eta(r \rightarrow 0) \simeq \frac{1}{M} \left(1 + 2r^2 / (\hat{R}_0 M)^2\right)$ , and we get  $\eta(r \rightarrow \infty) \simeq \hat{R}_0 / (4M)$  near infinity. It was this choice of parameters that was used to produce the first fully non-linear, 3D simulation of two orbits of a binary with mass ratio  $q = 100$  in [25]. In [175], Eq. (4.11) was furthermore validated for a highly spinning equal mass system with equal but opposite spins lying in the orbital plane and spin parameter  $\chi_i = S_i / M = \pm 0.92$  ( $i \in \{1, 2\}$ ).

The authors of [176] used Eq. (4.3) as well as a modification of it as initial value for an evolution equation on  $\eta(\vec{r})$ . We did not consider this option because the stability properties of the whole system have to be reevaluated when a new equation is added to the BSSN system, which we have not done, yet. However, the authors obtained stable evolutions in tests for mass ratios up to  $q = 4$ . Additionally, as they made Eq. (4.3) fall to zero for large  $r$  by multiplication with an appropriate fall-off function, the aforementioned gauge pulses in  $\eta(\vec{r})$  were significantly reduced in amplitude, and the method is very promising. Evolved gauge drivers have also proven success in the generalized harmonic formulation in [56], and for a range of parameters, the authors

there show that the hyperbolicity of the overall system can be maintained, which might also be true in the context of the BSSN formulation.

## 4.4 Using Purely Analytical Formulas for Dynamical Damping

While several other authors explored and enhanced our proposition, Eq. (4.3), we considered the gauge waves in  $\eta(\vec{r})$  being amplified as they travel outwards and producing noise at mesh refinement boundaries to be severe enough to not pursue this approach further.

Since we always know the location of a puncture, and we know its associated mass, we instead chose a form of damping that uses this local information throughout the domain. In [DM3], we therefore used the purely analytical expressions

$$\eta(\vec{r}) = A + \frac{C_1}{1 + w_1 (\hat{r}_1^2)^n} + \frac{C_2}{1 + w_2 (\hat{r}_2^2)^n} \quad (4.12)$$

and

$$\eta(\vec{r}) = A + C_1 e^{-w_1 (\hat{r}_1^2)^n} + C_2 e^{-w_2 (\hat{r}_2^2)^n}. \quad (4.13)$$

The positive, unitless parameters  $w_1$  and  $w_2$  can be chosen to change the width of the functions. The power  $n$  is a positive integer which determines the fall-off rate. The constants  $A$ ,  $C_1$ , and  $C_2$  are then chosen to provide the desired values of  $\eta(\vec{r})$  at the punctures and at infinity. Lastly,  $\hat{r}_1$  and  $\hat{r}_2$  are defined as  $\hat{r}_i = \frac{|\vec{r}_i - \vec{r}|}{|\vec{r}_1 - \vec{r}_2|}$ , where  $i \in \{1, 2\}$ , and  $\vec{r}_i$  is the position of the  $i^{\text{th}}$  black hole. The definition of  $\hat{r}_i$  is chosen to naturally scale the fall-off of Eqns. (4.12) and (4.13) to the separation of the black holes. In order to give the damping factor units of inverse mass, we choose  $A = 2/M$ , where  $M = M_1 + M_2$  is defined as the sum of the irreducible masses. We then take  $C_i = 1/M_i - A$ . In the equal mass case, the  $C_i$  vanish and both Eqns. (4.12) and (4.13) will give a constant value of  $\eta = 2/M$ . After the formation of a common apparent horizon, when the punctures are very close to each other, we switch back to using a constant value of  $\eta(\vec{r}) = 2/M$  on the whole grid in order to avoid singularities in Eqns. (4.12) and (4.13) when  $\vec{r}_1 \approx \vec{r}_2$ .

We designed the two formulas for  $\eta$  in order to test the value of using fundamentally different functions. In our simulations, we found little noticeable difference in the



application of one compared to the other. In the absence of such a difference, it becomes more beneficial to use Eq. (4.12), as Gaussian functions are more expensive to compute numerically than rational functions are. It should be pointed out that Eq. (4.12) is very similar to Eq. (13) suggested in [168], and we believe the following results are very similar to what would be found using that form for the damping.

As for the dynamical damping following Eq. (4.3), the impact of using Eq. (4.12) on the resulting waves is to be quantified. Here, using the formula for a single puncture or for an equal mass binary is identical to using  $\eta = 2/M$ , therefore such tests are dispensable. We immediately compare the results for unequal mass binaries.

#### 4.4.1 Mass Ratio 4:1

Again, we use the mass ratio  $q = 4$  for comparison of simulations using  $\eta = 2/M$  and Eq. (4.12). In [DM3], the test simulations started at  $D = 5M$ . and the binary components had no spins. The lowest resolution used 64 points in the boxes centered around the black holes, the medium one used 72 and for the finest resolution, 80 points were employed. The grid configurations are  $\chi[5 \times N : 7 \times 2N : 6 : 120N/72 : 0.5]$  with  $N \in \{64, 72, 80\}$ , and again we label the results by “low” ( $N = 64$ ), “med” ( $N = 72$ ) and “high” ( $N = 80$ ). We used  $n = 1$  and  $w_i = 12$  in Eq. (4.12). The influence of these parameters will be discussed later in this section. We compare gravitational waves extracted at a radius  $R_{\text{ex}} = 90M$ . Similarly to the results found in Sec. 4.3.2, the relative amplitude errors and the phase error were found to be considerably lower for the dynamical damping than for the standard choice  $\eta = 2/M$ . Figure 4.10 shows the relative amplitude error for both choices of  $\eta$ , and in Fig. 4.11 the phase error is plotted. In the runs with  $\eta = 2/M$ , the maximum relative amplitude error between low and medium resolution is about 12% (the solid green line) and about 7% between medium and high resolution (the dashed green line). Using Eq. (4.12), we see that the relative amplitude error is at most 4% between low and medium (solid black line) and 3% between the medium and high resolution runs (dot-dashed black line). For the maximum phase error, we obtain 0.32 rad and 0.2 rad between low and medium (solid green line) and medium and high (dashed green line) resolution for  $\eta = 2/M$ , respectively. For the dynamical damping, Eq. (4.12), the values are about 0.2 rad between low and medium (solid black line) and 0.1 rad between medium and high resolution (dot-dashed black line). The most remarkable fact from these plots is that

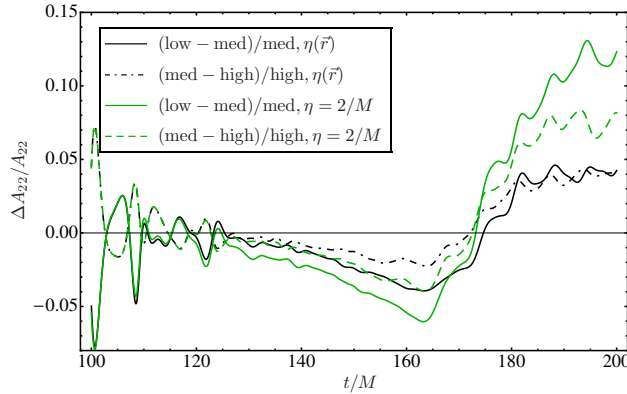


**Figure 4.10:** Relative amplitude differences of the 22-mode of  $\Psi_4$  (for  $q = 4, D = 5M$ ) between low and medium (green solid curve) as well as medium and high (green dashed curve) resolution when using  $\eta = 2/M$ . The same for  $\eta(\vec{r})$  (Eq. (4.12)) between low and medium (black solid curve) and medium and high resolutions (black dot-dashed curve). See text in Sec. 4.4.1 for the grid configurations. The maximum differences are above 10%, comparing low and medium resolution of the constant  $\eta$  simulations (green solid line). In contrast, the differences using dynamical damping are 4% at maximum.

in the series with varying  $\eta$ , even the error between coarse and medium resolution (the solid black line) is below the error between medium and fine resolution in the constant  $\eta$  case (the dashed green line). These results for amplitude and phase error suggest that we can achieve the same accuracy with less computational resources using a position-dependent  $\eta(\vec{r})$  through Eq. (4.12), or a higher accuracy spending the same amount of computational resources.

The parameters  $n$ ,  $w_1$  and  $w_2$  can be used to vary the falloff of  $\eta(\vec{r})$  around the punctures. When using mesh refinement and different time step sizes on each box, we can use these parameters to make sure that condition (4.2) is met everywhere on the grid. A side effect is that the size of the apparent horizons of the black holes varies on the grid when these parameters are changed. In [61, 167] it was noticed that the damping coefficient affects the coordinate location of the apparent horizon, and therefore the resolution of the black hole on the numerical grid. Fig. 4.12 plots the ratio of the grid-area of the larger apparent horizon to the smaller apparent horizon as a function of time for  $w$ -values of 0.1 (solid black), 0.5 (dotted black), 12 (dot-dot-dashed blue) and for 200 (dashed red), all with  $n = 1$ . Also plotted is the relative coordinate size for the same binaries using a constant  $\eta = 2/M$  (dot-dot-dashed orange line), and for using Eq. (4.3) (dashed-dotted green line). All the evolutions show an immediate dip, and then increase in the grid-area ratio during the course of

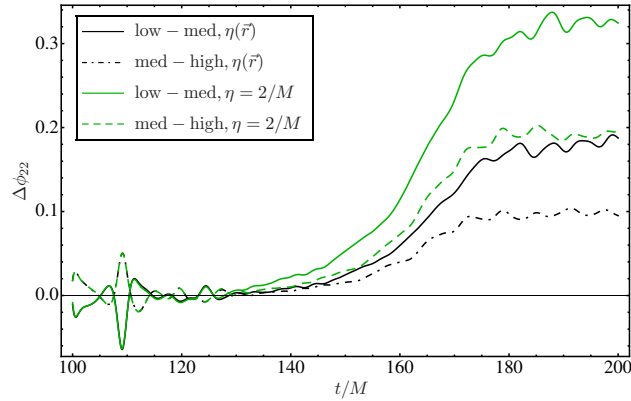


**Figure 4.11:** Phase differences of the 22-mode between lowest and medium resolution for the series using  $\eta = 2/M$  (solid green line) and  $\eta(\vec{r})$  (Eq. (4.12)) (solid black line) as well as between medium and high resolution for  $\eta = 2/M$  (dashed green line) and for  $\eta(\vec{r})$  (Eq. (4.12)) (dot-dashed black line). The physical situation is the same as in Fig. 4.10 ( $q = 4, D = 5M$ ). The phase errors between low and medium resolution with dynamical damping are lower than those between high and medium resolution for constant damping.

the evolution. While a very low ratio was found using Eq. (4.3), the orange dotted line was later found for the choices of  $n = 3$  with  $w_1 = 0.01$  and  $w_2 = 0.0001$  in Eq. (4.12). Due to this freedom in the implementation of our explicit formula for the damping, it may be possible to further reduce the relative grid size of the black holes.

In addition to these relatively short test runs, we now also have simulations with initial separation  $D = 10M$  available where Eq. (4.12) is employed. Here, 16 GW cycles are completed, which corresponds to about eight black hole orbits. For the  $\eta = 2/M$  case, the results of this configuration were presented in [DM4]. There, we found that the waves seem to exhibit 2<sup>nd</sup> order convergence. This, however, is not the true order of convergence, but the runs only start to enter the convergent regime, and the errors are still very high. The grid configurations for this convergence series are  $\chi[3/5 \times N : 7 \times 2N : 6]$  with  $N \in \{80, 88, 96\}$ . Around the smaller black hole, we use two more boxes than around the larger one so as to obtain the same effective resolution for both holes. This works because the mass of the larger black hole is four times the mass of the smaller one, and the resolutions double from box to box.

In [DM4], the waveform errors are assessed through Richardson extrapolation to infinitely high resolution. The error is then computed from the difference between the best resolved run and the Richardson extrapolated result. The extraction radius is again  $R_{\text{ex}} = 90M$ . Assuming 2<sup>nd</sup> order convergence, we obtain a conservative phase

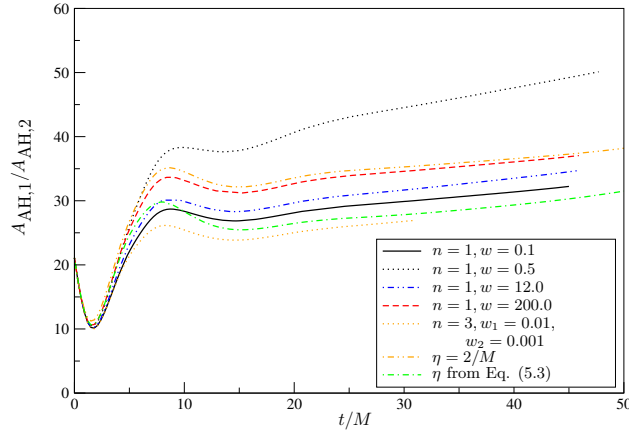


**Figure 4.12:** Shown is the time dependence of the ratio between the coordinate areas of the apparent horizons of both black holes in a simulation with mass ratio  $q = 4$  and initial separation  $D = 5M$ . The black, blue and red lines use  $\eta(\vec{r})$ , Eq. (4.12) with varying values of the width parameter  $w$ . The orange line (dash-dot-dot) uses the constant damping,  $\eta = 2/M$ , and the green (dash-dot) one refers to the result of [DM2] with Eq. (4.3). Using Eq. (4.12), the coordinate areas can be varied with respect to each other depending on the choice of  $w$ . A ratio of 1 means the black holes have the same size on the numerical grid.

error of 6.7 rad in the 22-mode. The amplitude error is more difficult to assess. The amplitude is treated as a function of gravitational wave frequency because otherwise a non-zero phase error also affects the amplitude error. Because the frequency is too noisy to be used directly for a parameterization of the amplitude, a fit has to be employed. The paper states that this fit is far from ideal and therefore not useful for a convergence analysis, which also makes a Richardson extrapolation quite difficult. The resulting maximum amplitude error between medium and high resolution is 4%.

We can now determine how these error estimates change when using dynamical damping. Figure 4.13 shows the amplitudes for all three resolutions in a time range around merger. The results with constant  $\eta$  are plotted in pale colors and those for  $\eta(\vec{r})$  in vivid colors. This plot already indicates that the results with dynamical damping are much closer to each other for different resolutions than the constant damping results. This will be quantified in the following. Convergence plots for the phase as a function of time are shown in Fig. 4.14. The difference between low and medium resolution is plotted in black for  $\eta(\vec{r})$  (Eq. (4.12)) and gray for  $\eta = 2/M$ . The differences between medium and high resolution, scaled to second order convergence, are plotted in dashed dark green for Eq. (4.12) and light green for  $\eta = 2/M$ . Although the results for dynamical damping still seem to exhibit 2<sup>nd</sup> order convergence, it is

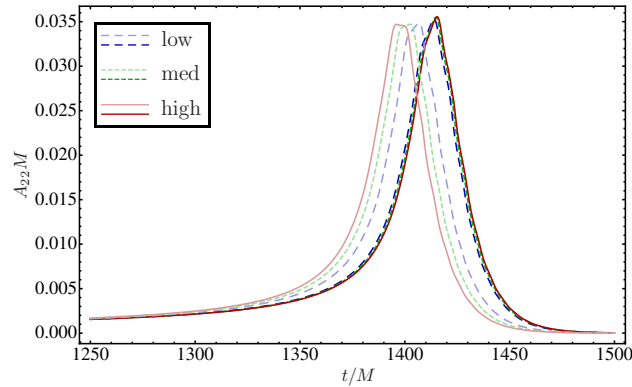


**Figure 4.13:** Comparison between the amplitudes of the 22-mode of  $\Psi_4$  for  $q = 4$  and  $D = 10 M$ , extracted at  $R_{\text{ex}} = 90 M$ , in three different resolutions (low, medium and high, see text in Sec. 4.4.1) using either Eq. (4.12) (vivid colors) or  $\eta = 2/M$  (pale colors). The results for different resolutions are very close to each other in the case where  $\eta(\vec{r})$  is used and can hardly be distinguished.

apparent that the differences between resolutions decrease by about a factor of four when using the dynamical damping. As done in [DM4], we quantify the phase error using Richardson extrapolation in Fig. 4.15. Here, we are conservative and perform the Richardson extrapolation assuming  $2^{\text{nd}}$  order convergence. We then compute the difference of the Richardson extrapolated phase to the result from the highest resolution. This recovers the error of 6.7 rad found in [DM4] for the  $\eta = 2/M$  case (gray solid line). The phase error in the case of dynamical damping amounts to only about 1.5 rad.

For a convergence plot of the gravitational wave amplitude in Fig. 4.16, we use the amplitude as a function of time because of the difficulties in assessing the frequency discussed before. The amplitude also seems to exhibit  $2^{\text{nd}}$  order convergence in the constant damping case (displayed in gray and light green) whereas for the dynamical damping, the amplitude differences scale best to third order convergence (the black and dark green lines). As for the phase, we find that the amplitude differences between resolutions decrease when dynamical damping is used. A lower amplitude error could be due to the lower phase error which certainly translates to the amplitude as well. In order to separate the amplitude from the phase error, we now use amplitude as a function of phase,  $A(\phi) = A(t(\phi))$ . We do not use the frequency  $\omega$ , as in [DM4], because this introduces additional errors through the differentiation  $\omega = -d\phi/dt$ . The phase itself is noisy, especially in the beginning of the simulations when the signal is very weak, but for a conservative error estimate, we believe it to be sufficiently

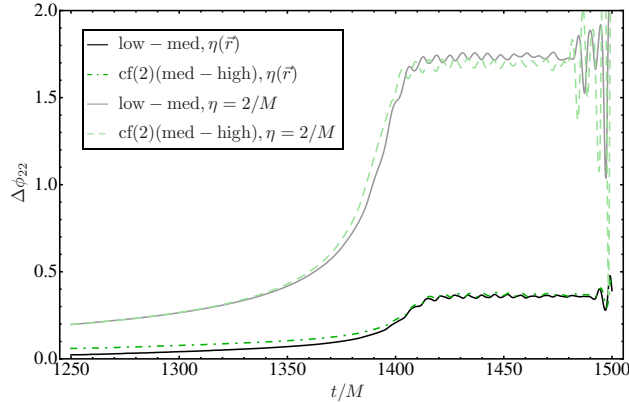


**Figure 4.14:** Convergence plots of the phase of the 22-mode of  $\Psi_4$  for  $q = 4$ ,  $D = 10 M$ . Compared is a series of simulations using  $\eta(\vec{r})$  according to Eq. (4.12) (plotted in vivid colors) and one series using  $\eta = 2/M$  (plotted in pale colors). The black and gray lines show the differences between low and medium resolutions (see text for details on the resolutions). The green and light green lines show the differences between medium and high resolution results, scaled with the factor  $\text{cf}(2)$  (Eq. (2.43)) for second order convergence. While the absolute error in the phase is lower by a factor of about 5, the second order convergence is not as clear in the simulations with  $\eta(\vec{r})$  as in the ones using a constant  $\eta$ , at least up to merger at  $t \simeq 1410 M$ .

accurate. The result is plotted in Fig. 4.17. The merger takes place when the phase has reached approximately  $-100$  rad and the lower the value of the phase, the later the time during the simulation. The range  $\phi = -70 \dots -135$  rad we use in the plot covers the time frame  $t = 1250 \dots 1500 M$  we used in Figs. 4.13 to 4.16 before. We recover the relative amplitude error of 4% for  $\eta = 2/M$  between medium and high resolution (gray line) stated in [DM4]. For the dynamical damping, Eq. (4.12), the relative error decreases to below 1% (black line). For the amplitude, we can also perform a Richardson extrapolation to obtain another error estimate. In this case, however, the procedure is more difficult. As discussed before, the  $A(t)$  curves are affected by the phase error and the  $A(\phi)$  ones by an in the beginning noisy phase function. Richardson extrapolating the amplitude as a function of phase and computing the difference from this to the highest resolution result gives us relative errors of about 20% for  $\eta = 2/M$  and 4% when Eq. (4.12) is used.

Altogether we find that the errors are reduced by a factor of four in amplitude and phase, independent of the kind of error estimate we employ. Given the improved accuracy of the runs with dynamical damping, we estimate how this translates to the physical parameters of the final black hole. We compare final mass, final spin and kick velocity between runs using constant damping and those using Eq. (4.12) in

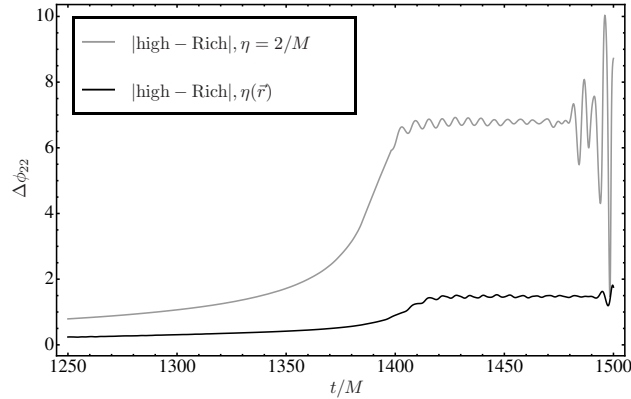


**Figure 4.15:** Error between highest resolution and Richardson extrapolated phase of the 22–mode for  $q = 4$ ,  $D = 10M$ . The gray line shows the result for constant damping,  $\eta = 2/M$ , whereas the black line shows the same for dynamical damping, Eq. (4.12). For the Richardson extrapolation, 2<sup>nd</sup> order convergence is assumed and the result gives a conservative estimate on the error.

Tab. 4.1. We estimate the final mass as described in Sec. 2.5. The results at extraction radii  $R_{\text{ex}} \in \{40, 50, 60, 80, 90\}M$  are used to extrapolate the radiated energy flux, as given in Eq. (2.36), to infinite extraction radius. Afterwards, the results for different resolutions are Richardson extrapolated assuming fourth order convergence, as in [DM4]. The final mass is the same as for the  $\eta = 2/M$  simulation,  $M_{\text{final}}/M = 0.978 \pm 5 \times 10^{-4}$ . We estimate the final spin using the ringdown frequency of the 22–mode and applying the quasi–normal modes method of Sec. 2.5. As in the case with constant damping, we find  $a_{\text{final}}/M_{\text{final}} = 0.471$  with an uncertainty of 1%. The reduced phase error carries over to the result for the kick velocity where we find an improvement over the  $\eta = 2/M$  data. We estimate the kick velocity to  $v_{\text{kick}} = (138 \pm 4)$  km/s which compares very well to the result  $v_{\text{kick,fit}} = (135 \pm 7)$  km/s given by the fit formula in [94]. In both cases, the integration of Eq. (2.38) was started at  $t = 120M$  after the initial junk radiation has passed.

$\eta$	$M_{\text{final}}/M$	$a_{\text{final}}/M_{\text{final}}$	$v_{\text{kick}}$ (km/s)
$2/M$	0.978	0.471	$145 \pm 10$
Eq. (4.12)	0.978	0.471	$138 \pm 4$

**Table 4.1:** Final mass  $M_{\text{final}}$ , final spin  $a_{\text{final}}$  and kick velocity  $v_{\text{kick}}$  for mass ratio  $q = 4$  compared between the simulations using constant damping,  $\eta = 2/M$ , and dynamical damping following Eq. (4.12). The results for constant damping (first line) were presented in [DM4]. All values agree inside their error bounds, but the kick velocity can be estimated with lower error when dynamical damping is used.

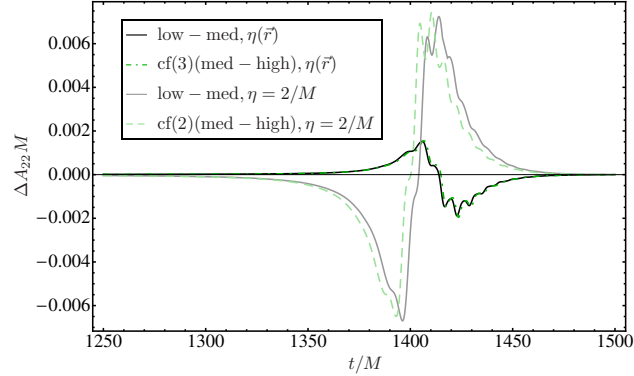


**Figure 4.16:** Convergence plots of the amplitude of the 22-mode of  $\Psi_4$  for  $q = 4$ ,  $D = 10 M$ . Compared are a series of three simulations with low, medium and high resolution (see text) using  $\eta(\vec{r})$  according to Eq. (4.12) (plotted in vivid colors) and one series (with the same resolutions as the first one) using  $\eta = 2/M$  (plotted in pale colors). The black and gray lines show the differences between low and medium resolutions. The green and light green lines show the differences between medium and high resolution results, scaled to a certain order of convergence. Here,  $\text{cf}(2)$  is the factor for second order convergence and  $\text{cf}(3)$  the one representing third order convergence (see Eq. (2.43)).

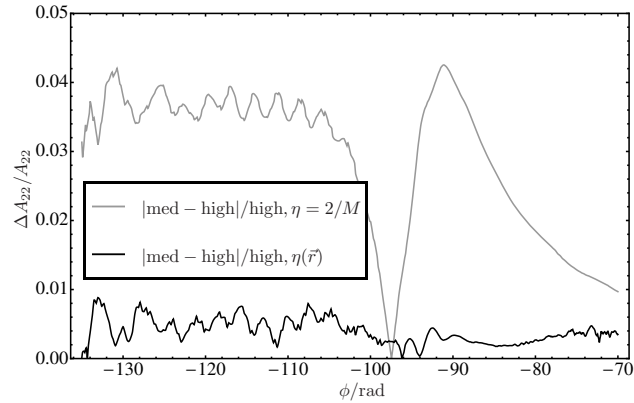


**Figure 4.17:** Error estimate of the gravitational wave amplitude as a function of gravitational wave phase for  $q = 4$ ,  $D = 10 M$  between medium and high resolution results (see text in Sec. 4.4.1 for the resolutions). Compared are a convergence series with constant damping (gray line) and with dynamical damping following Eq. (4.12) (black line). The merger takes place around  $\phi = -100$  rad.



# 5 Highly Accurate Binary Black Hole Simulations

In this chapter, numerical simulations including spins will be used to assess the accuracy of gravitational wave extraction from our code and the question how it can be improved will be addressed. Further on, simulations of spinning black holes with a mass ratio above one and vanishing total spin, which have been computed in the course of the Numerical Relativity Analytical Relativity (NRAR) project, will be discussed. Finally, we will concisely review the construction of phenomenological waveform templates for black hole binaries including spins and unequal masses, which will hopefully be used in detector analysis pipelines in the future.

## 5.1 Accuracy of Wave Extraction

Accurately extracting gravitational waves from a numerical simulation is the basis for any further analysis, be it astrophysical studies, the calibration of analytical waveform models or final parameters, gravitational wave detection or parameter estimation. We therefore study how the grid setup in the wave zone influences the accuracy of the extracted waves. As a test system we choose an equal mass binary with spins aligned with the orbital angular momentum and equal in size,  $\chi_i = |S_{z,i}|/M_i^2 = 0.5$ , and initial distance  $D = 6M$ . The small initial distance leads to short runs, and the gravitational wave from merger reaches the largest extraction radius after about  $290M$ . The configuration is simple enough to exhibit a high degree of symmetry (we only need to simulate one quadrant of the whole space) while the spins introduce a certain amount of difficulty for the wave extraction. Altogether, the simulations run fast while the wave extraction is demanding enough to allow for an accuracy study.

We use a certain standard grid setup, which we will call “Rbasic” in the following, and analyze the convergence behavior and error of the amplitude and phase of the

Setup	Rbasic/Rboundary			Rreso		
	$N$	64	72	80	64	72
$h_{60,70}$	$1.5 M$	$1.33 M$	$1.2 M$	$0.75 M$	$0.67 M$	$0.6 M$
$h_{80,90}$	$1.5 M$	$1.33 M$	$1.2 M$	$1.5 M$	$1.33 M$	$1.2 M$

**Table 5.1:** Resolution  $h$  in the wave zone for the three grid setups Rbasic, Rboundary and Rreso for the low ( $N = 64$ ), medium ( $N = 72$ ) and high resolution ( $N = 80$ ). The subscript to  $h$  indicates at which extraction radii (in terms of  $M$ ) the resolution is given.

22-mode of the Weyl scalar  $\Psi_4$ , which is extracted at  $R_{\text{ex}} \in \{(60, 70, 80, 90) M\}$ . Now we vary the size of the five non-moving boxes in the grid. In a second configuration, called ‘‘Rboundary’’ in the following, the waves are resolved with the same accuracy as in the Rbasic runs, but the four outermost boxes are made larger so as to push the outer boundary farther away from the punctures. The first non-moving box is not changed in this setup in order to keep the resolution of the gravitational waves the same as in Rbasic. For the third configuration, labelled ‘‘Rreso’’, we additionally increase the size of the first non-moving box, such that the first two extraction radii now lie on a level with twice the resolution compared to Rbasic and Rboundary. The extraction radii  $80 M$  and  $90 M$  still lie on the same level as before, but the waves reaching these radii have propagated at higher resolution for a larger distance. The grid resolutions at the different extraction radii are summarized in Tab. 5.1 for the three setups Rbasic, Rboundary and Rreso.

For all setups, the number of inner, moving boxes is  $l_1 = 5$ , and we use three different resolutions in each setup. The low resolution has  $N = 64$  points in the inner boxes and a finest resolution of  $h_{\text{min}}/M = 0.023$ , for the medium resolution, we have  $N = 72$  with  $h_{\text{min}}/M = 0.021$ , and the high resolution has  $N = 80$  points in the inner boxes and a finest resolution of  $h_{\text{min}}/M = 0.019$ . Around these moving boxes, we put  $l_2 = 5$  non-moving boxes with different sizes which are listed in Tab. 5.2 together with the according number of grid points in a box.

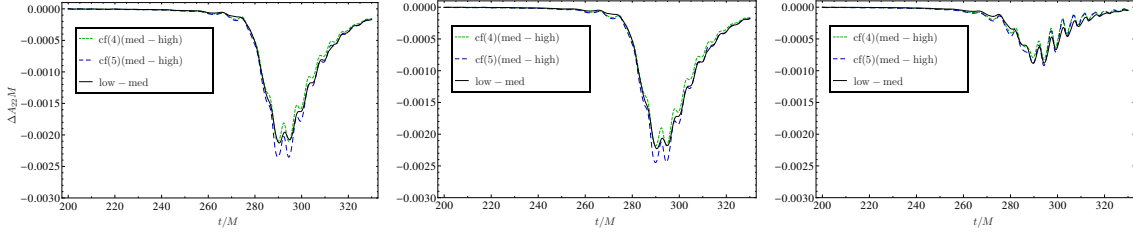
The convergence of the amplitude of the 22-mode, extracted at  $R_{\text{ex}} = 90 M$ , is studied in Fig. 5.1 for the three different grid setups. We plot the difference between the low ( $N = 64$ ) and medium ( $N = 72$ ) resolution as a black, solid line and the difference between medium and high ( $N = 80$ ) resolution, scaled to different convergence orders as indicated by the plot legends, as dashed lines. The left panel shows that the amplitude is between 4<sup>th</sup> and 5<sup>th</sup> order convergent for Rbasic. The situation does not change much in the Rboundary setup, as can be seen in the middle panel of that

Level	Rbasic <sub>64</sub>		Rboundary <sub>64</sub>		Rreso <sub>64</sub>	
	$N_l$	$r_l/M$	$N_l$	$r_l/M$	$N_l$	$r_l/M$
0	128	768	192	1158	192	1158
1	128	430	192	609	192	621
2	128	215	192	305	192	311
3	128	107	192	152	192	155
4	128	54	128	52	192	78

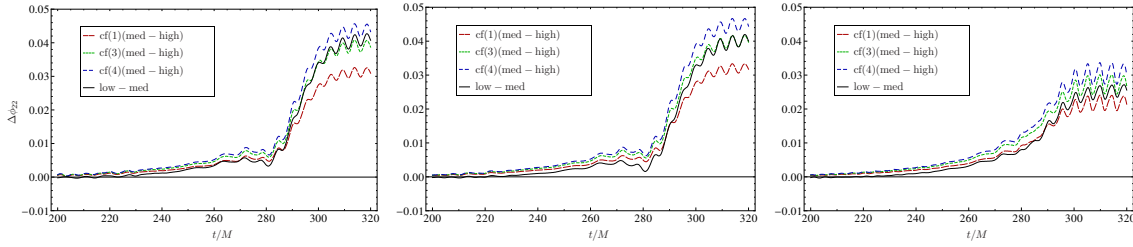
**Table 5.2:** Number of points in the non-moving levels for the setups Rbasic, Rboundary and Rreso for the lowest resolution with  $N = 64$  points in the inner levels. Level  $l$  then has a total size of  $2r_l$  in each spatial direction. The values are taken from the code, e.g. they include mesh refinement buffer points. For the higher resolution runs (with  $N = 72$  and  $N = 80$  points in the inner levels) the number of points in each level can be obtained by multiplying the values for  $N_l$  given here with  $72/64$  for  $N = 72$  and  $80/64$  for  $N = 80$ . The position of the outer boundary in a setup is given by  $r_l$  for  $l = 0$ .

figure. For the setup Rreso, displayed in the right panel of Fig. 5.1, however, we see that the amplitudes still converge to between 4<sup>th</sup> and 5<sup>th</sup> order, but the differences between different resolutions decreased by a factor about 2.5 compared to Rbasic and Rboundary. A similar behavior is found for the phase, as shown in Fig. 5.2. Here the convergence is less clean than for the amplitude, but the phase differences are very small. There is nearly no visible difference between the convergence plots for Rbasic (left panel) and Rboundary (middle panel), but in the plot for Rreso (right panel) we find that the phase error between resolutions decreased by a factor of 2 compared to the other two setups. We thus conclude that the influence of the outer boundary on the accuracy of the extracted waves is minor, if not negligible, in the setups used here, since it is causally disconnected from the extraction radii during the whole simulation already in the Rbasic setup. We might have seen an influence of the location of the box boundaries in the wave zone, but this is also not the case. However, increasing the resolution in part of the wave zone has a major impact, even though we do not actually extract the waves at a higher resolution (for  $R_{\text{ex}} = 90M$  the waves are always resolved equally as can be seen in Tab. 5.1).

The extraction of higher order modes (i.e. those with multipole order  $l \geq 3$  in Eq. (2.26)) is an important topic for physical systems which exhibit less symmetry than the equal mass, non-spinning configuration. In particular, for systems with unequal masses, higher multipoles become important since they contribute significantly to the total radiated energy, see e.g. [69, 78]. Since these modes have a much lower amplitude than the dominant  $l = 2$  modes, extracting them in a numerical simulation is difficult as numerical noise dominates these modes. We can use the grid



**Figure 5.1:** Convergence of the amplitudes of the 22–modes for equal mass,  $D = 6 M$  simulations with initial spins  $\chi_i = 0.5$  pointing along the orbital angular momentum, extracted at  $R_{\text{ex}} = 90 M$ . Each panel shows the convergence in one of the grid setups given in Tab. 5.1 (from left to right: Rbasic, Rboundary and Rreso). In each panel, the black line is the difference between low and medium resolution. The difference between medium and high resolution has been scaled for 4<sup>th</sup> order convergence (green, dashed line) and for 5<sup>th</sup> order convergence (blue dashed line). There are only minor changes in the results for Rbasic and Rboundary, but in the Rreso runs, the amplitude differences decrease by a factor of 2.5 compared to the other two grid setups.



**Figure 5.2:** Convergence plots for the phase of the 22–mode for the equal mass,  $\chi_i = 0.5$  simulations with initial separation  $D = 6 M$ . The different panels show the results for the three different grid setups given in Tab. 5.1 (from left to right: Rbasic, Rboundary and Rreso). The black line is always the difference between low and medium resolution. The other curves show the difference between medium and high resolution, scaled to 1<sup>st</sup> (red solid line), 3<sup>rd</sup> (green dashed line) and 4<sup>th</sup> order convergence. As for the amplitude, we see little difference between the setup Rbasic and Rboundary, but the phase differences decrease by about a factor of 2 in the Rreso setup.

setups Rbasic and Rreso to determine the amount of resolution needed for the second most dominant modes in the physical system we study in this section, which are the  $l = |m| = 4$  modes. Since spins are present, a small fraction of the total energy is radiated in higher modes, although none of these contributes more than 1% to the total energy, as shown in [DM4].

With the grid Rbasic, we extract the 44–mode at a resolution  $h = 1.5 M$ , as indicated in Tab. 5.1. In the setup Rreso, we can extract it at twice this resolution, if we consider the second extraction radius,  $R_{\text{ex}} = 70 M$ . Figure 5.3 shows the amplitude of the 44–mode extracted at this radius in both setups, each with the three different

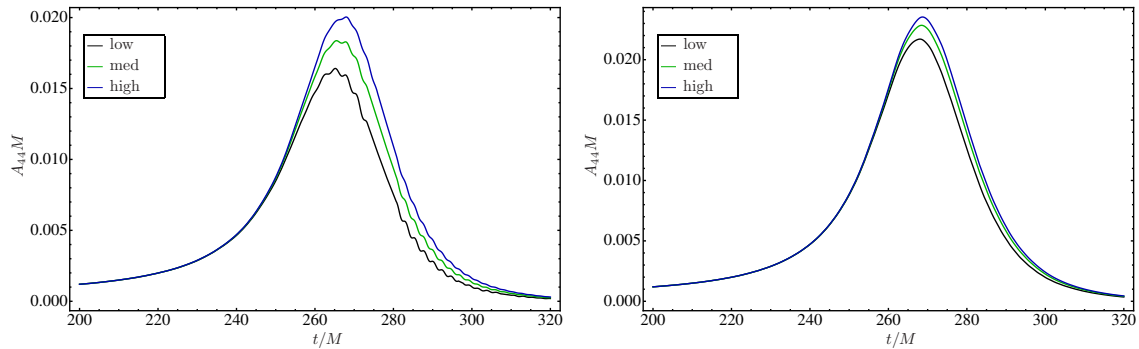


**Figure 5.3:** Amplitude of the 44–mode for the equal mass,  $\chi_i = 0.5$ ,  $D = 6M$  simulation with the Rbasic grid setup (left panel) and the Rreso setup (right panel), extracted at  $R_{\text{ex}} = 70M$ . Each plot includes all three resolutions of the convergence series, labelled “low” ( $N = 64$ ), “med” ( $N = 72$ ) and “high” ( $N = 80$ ). The waves in the right panel are extracted with twice the resolution compared to the left panel, and the amplitudes are much cleaner.

resolutions of the convergence series. The improvement for the doubled resolution is striking. The amplitudes are very clean in the right panel of the figure, where Rreso is used, in contrast to the left panel where the grid setup is Rbasic. This fact is reflected in the amplitude convergence, too. Figure 5.4 opposes the convergence in the Rbasic setup in the left panel to the one obtained with Rreso in the right panel. Whereas the amplitudes converge only to first order when extracted at a resolution of  $1.5M$ , we obtain very clean fourth order convergence when we extract at  $0.75M$ . For comparison, scaling of the amplitudes to second and fifth order of convergence is shown, too. A second observation from this figure is that the amplitude error is about a factor of two lower in the Rreso setup. This example shows that amplitude of the 44–mode can be cleanly extracted with twice the resolution necessary for the 22–mode. Contrary to what we found for the 22–mode, we do not see this much of an improvement if we extract the 44–mode at extraction radius  $90M$ , which has a resolution of  $1.5M$  in both grid setups. Propagating the wave for a longer distance is not enough, here, we also have to actually extract the wave in the region where the resolution is doubled. For the phase, the differences between Rbasic and Rreso are not as pronounced as for the amplitude. The phase convergence changes from 1<sup>st</sup> to nearly 3<sup>rd</sup> order from Rbasic to Rreso.

Increasing the resolution in the wave zone is computationally much less expensive than increasing the overall resolution, which would include the boxes moving with the black holes. The example shown here demonstrates that a careful choice of

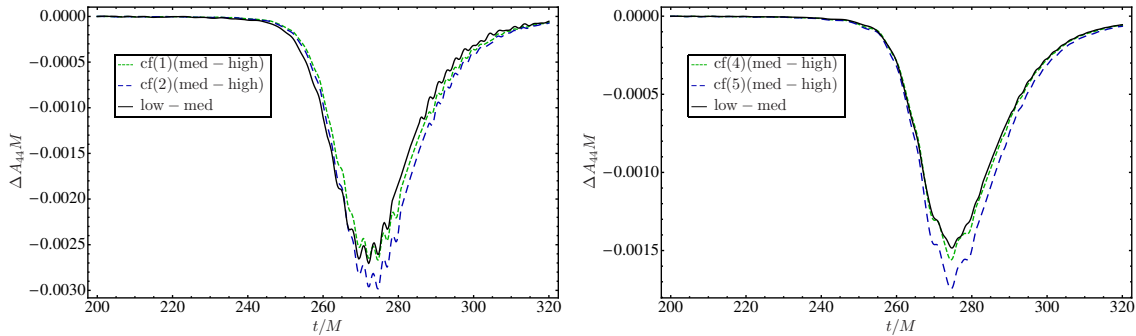


**Figure 5.4:** Convergence plots for the amplitude of the 44-mode for the equal mass,  $\chi_i = 0.5$ ,  $D = 6M$  simulation with the Rbasic grid setup (left panel) and the Rreso setup (right panel), extracted at  $R_{\text{ex}} = 70M$ . In each panel, the black line is the difference between low ( $N = 64$ ) and medium ( $N = 72$ ) resolution. The green and blue dashed lines are the difference between medium and high ( $N = 80$ ) resolution results, scaled to different orders of convergence, as indicated by the plot legends. The amplitude converges only to 1<sup>st</sup> order in the Rbasic setup, but to clean 4<sup>th</sup> order when they are extracted at twice the resolution, which is done in the Rreso setup. It can also be seen that the differences between resolutions decrease by nearly a factor of two when comparing Rbasic on the left and Rreso on the right.

grid setup can lead to significant ameliorations concerning convergence and purity of subdominant modes as well as errors in the dominant mode.

## 5.2 Simulations with Vanishing Total Spin

The most extensively studied subclass of binaries with spins consists of equal mass black holes with spins either aligned or anti-aligned with the orbital angular momentum and with equal magnitudes [154, 177–180]. Generic spin configurations with different mass ratios have been used to calibrate analytic formulas for the final parameters in [89, 94, 181–183]. Within the NRAR project, we take the step to a different subclass in which the black holes have unequal masses and where spins are chosen such that the total spin of the system,  $\vec{S} = \vec{S}_1 + \vec{S}_2$ , vanishes. We reported on the eccentricity of these runs in Sec. 3.5.5, showing that our initial data works well in this special configuration, see Fig. 3.7. Here, we want to summarize the basic properties of these simulations.

We simulate a black hole binary with mass ratio  $q = 2$  with spins (anti-)aligned with the orbital angular momentum ( $z$ -direction),  $S_{z,i} = \pm 0.067M^2$ . The individual black hole spin magnitudes can also be written as  $\chi_1 = |\vec{S}_1|/M_1^2 = 0.6$  and

$\chi_2 = -|\vec{S}_2|/M_2^2 = -0.15$ , where the minus sign indicates that the second spin points opposite to the orbital angular momentum. The initial separation of the black holes is  $D = 10 M$ , and we perform a series of runs with increasing resolution. This is one convergence series in a sequence of runs with vanishing total spin provided to NRAR by different groups, and the whole set of simulations will have to be investigated in the future.

The grid configurations of the three highest resolution runs performed are  $\chi[(4/5) \times 80 : 7 \times 160 : 6 : 79.95 : 0.5]$ ,  $\chi[(4/5) \times 88 : 7 \times 176 : 6 : 87.94 : 0.5]$  and  $\chi[(4/5) \times 96 : 7 \times 192 : 6 : 95.94 : 0.5]$  in the notation introduced in Eq. (2.39). Here we have used a different number of refinement levels around the smaller and the larger black hole, which is why we give two values for  $l_1$ , separated by a slash. Because the mass of the larger puncture is twice the mass of the smaller one, and because the resolution doubles from one level to the next one, this means that both punctures have the same finest resolution in terms of their individual masses. The grid configurations are also summarized in Tab. 5.3 We extract gravitational waves at seven different extraction radii,  $R_{\text{ex}} \in \{(62, 70, 78, 86, 94, 100, 120)M\}$ .

The NRAR community has set up an accuracy requirement for the phase of the  $(l = 2, m = 2)$ -mode of  $\Delta\phi < 0.05$  rad at GW frequency  $M\omega = 0.2$  and an amplitude accuracy of 1% at  $M\omega = 0.2$ . The analysis presented here has been done at extraction radius  $R_{\text{ex}} = 120 M$  for the  $(l = m = 2)$ -mode, and we decompose  $\Psi_4$  into amplitude and phase. A convergence plot for the phase is shown in Fig. 5.5, and Fig. 5.6 provides the relative amplitude errors between different resolutions. We find that our two highest resolutions are just entering the convergent regime, and clean overall convergence for the three highest resolutions can not be found.

The accumulated phase difference between the two highest resolutions is 0.012 rad

Label	$l_1$	$l_2$	$N$	$h_{\text{min}}/M_i$	$h_{\text{max}}/M$	$r_{\text{out}}/M$
low	4/5	7	80	0.0375	25.62	2050
med	4/5	7	88	0.0341	23.29	2050
high	4/5	7	96	0.0313	21.35	2050

**Table 5.3:** Grid configurations of the runs in the NRAR convergence series, with the different resolutions labelled “low”, “med” and “high”. The black holes are surrounded by  $l_1$  refinement levels with  $N$  grid points and an additional number of  $l_2$  levels containing  $2N$  grid points. The central resolution around puncture  $i$  ( $i = 1, 2$ ) with mass  $M_i$  is given by  $h_{\text{min},i}/M_i$  and the coarsest resolution is  $h_{\text{max}}$ , given in terms of the total mass  $M$ . The outer boundary is placed at  $r_{\text{out}}$ .



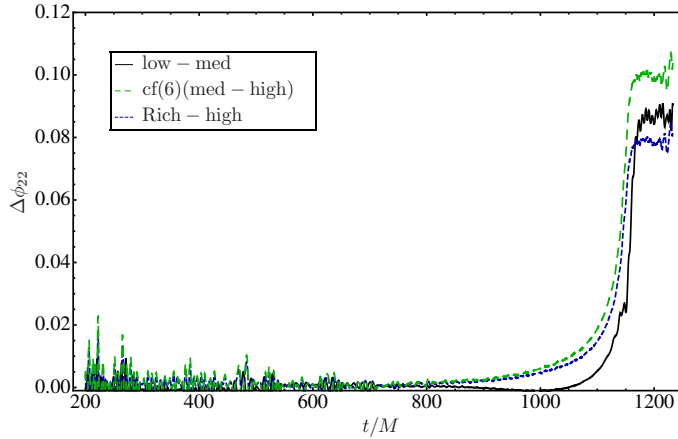


**Figure 5.5:** Phase differences over time for the zero total spin configuration. See Tab. 5.3 for the grid parameters of “low”, “med” and “high”. The black line is the difference between the lowest and medium resolution phase, the green dashed one the difference between medium and high resolution scaled to 6<sup>th</sup> order convergence, showing that the lowest resolution result is not yet in the convergent regime. The blue, dashed line is the phase error between the Richardson extrapolated phase and the highest resolution, which assumes that the medium and high resolution are 4<sup>th</sup> order convergent. The errors are below the NRAR specification of  $\Delta\phi < 0.05\text{rad}$  at  $M\omega = 0.2$  which occurs at  $t_{M\omega} = 1123M$  in this plot.

at a frequency of  $M\omega = 0.2$  (which corresponds to  $t = 1123M$  in Figs. 5.5 and 5.6). Because of this small difference, we can be confident that they lie in the convergent regime. Conservatively assuming 4<sup>th</sup> order convergence of the highest resolved phases, we can produce the Richardson extrapolated phase and use the difference between the highest resolution and the Richardson phase as an error estimate. The accumulated phase error at  $M\omega = 0.2$  turns out to be 0.03 rad which is still inside the NRAR error bounds of 0.05 rad. The relative amplitude error between the highest and medium resolution is below 1% for the whole time of simulation.

The parameters of the final black hole are summarized in Tab. 5.4. The table also includes the values we obtain from a non-spinning binary with otherwise the same parameters. This way we get an idea of the impact of spins which add up to a vanishing total spin in comparison to a system with zero total spin where, however, the individual spins vanish, too. The radiated energy  $E_{\text{rad}}$  has been calculated, as described in Sec. 2.5, by integrating the energy flux, Eq. (2.36), over the time of simulation at all extraction radii for each of the three resolutions. We then extrapolated to  $R_{\text{ex}} \rightarrow \infty$  and performed a Richardson extrapolation assuming 4<sup>th</sup> order convergence. The uncertainty in the radiated energy is about 3%. Hence we obtain



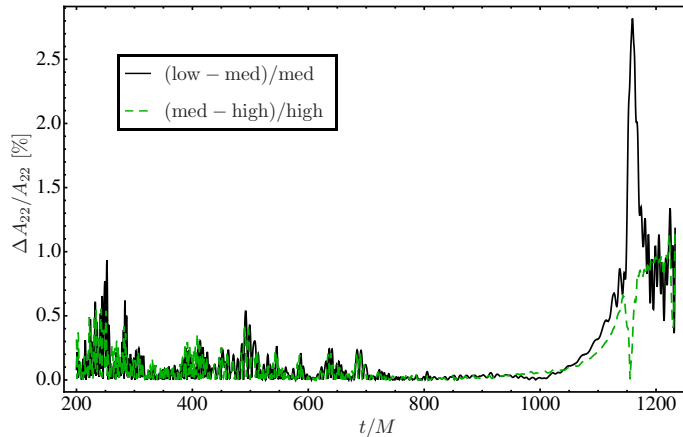


**Figure 5.6:** Relative amplitude differences in percent between the simulations of the zero total spin configuration. The labels “low”, “med” and “high” refer to the resolution and are explained in detail in Tab. 5.3. The black line is the difference between the amplitudes in low and medium resolution, scaled by the medium resolution. The differences between medium and high resolution, scaled by the high resolution, are plotted as green dashed line. The amplitude error between medium and high resolution is below the NRAR request of 1% at  $M\omega = 0.2$  for the whole simulation.

a final mass of  $M_{\text{final}} = 0.961 M$  with an uncertainty based on the uncertainty in the radiated energy. The final spin was determined from the ringdown frequency of the 22–mode computed at  $R_{\text{ex}} = 120 M$  in the highest resolution simulation, using the method described in Sec. 2.5, and we obtain  $S_{\text{final}} = 0.611 M_{\text{final}}^2$ . Additionally, we measured the number of gravitational wave cycles completed after the passage of the junk radiation up to the time where the amplitude of the 22–mode peaks, which is  $N_{\text{GW}} = 13.5$  for our zero total spin configuration. In comparison with the non–spinning case we find that one more GW cycle is completed in the spinning case. The mass of the final black hole agrees for both configurations inside the error ranges. The final spin is a little larger in the non–spinning case, but comparable, and we find the largest difference in the velocity with which the final black hole is recoiled, which will be discussed below.

The recoil velocity is computed from the two extraction radii lying closest to the binary,  $R_{\text{ex}} \in \{62 M, 70 M\}$ . This is because we find that the larger extraction radii are not resolved well enough to allow for an accurate estimate. The same was found in [DM4], where  $R_{\text{ex}} \in \{50 M, 60 M\}$  were used to determine the kick velocity. We perform the extrapolation to infinity assuming a  $1/R_{\text{ex}}$  fall–off in the error. Assuming 4<sup>th</sup> order convergence of the extrapolated values at different resolutions, the Richard-

$(\chi_1, \chi_2)$	$E_{\text{rad}}/M$	$N_{\text{GW}}$	$M_{\text{final}}/M$	$S_{\text{final}}/M_{\text{final}}^2$	$v_{\text{kick}}/(\text{km/s})$
$(0.6, -0.15)$	$0.03 \pm 3\%$	13.5	$0.961 \pm 3\%$	$0.611 \pm 0.006$	$227 \pm 6$
$(0, 0)$		12.5	0.962	0.623	$140 \pm 5$

**Table 5.4:** Final parameters of two configurations with mass ratio  $q = 2$ , initial separation  $D = 10 M$  and the total spin  $\vec{S} = \vec{S}_1 + \vec{S}_2$  vanishing. The first row shows the results where the individual spins are non-zero and pointing along the direction of the orbital angular momentum. In the second row, the black holes (initially) had no spins at all, and the values are taken from [DM4]. The total radiated energy is given by  $E_{\text{rad}}$ , the number of gravitational wave cycles by  $N_{\text{GW}}$ . The final black hole has a mass of  $M_{\text{final}}$  and a spin magnitude  $S_{\text{final}}$ , and its recoil velocity is given by  $v_{\text{kick}}$ . The total mass of the system is  $M$ .

son extrapolated kick velocity is  $v_{\text{kick}} = 227 \text{ km/s}$ , with an error of  $6 \text{ km/s}$  to the result computed at highest resolution.

The authors of [179] provide an analytic formula for the recoil velocity resulting from non-precessing black hole binary inspirals. Such scenarios result in a recoil in the orbital plane, and we therefore call it in-plane kick. The formula contains certain parameters which are fit to a number of numerical relativity simulations. The magnitude of the recoil velocity can thus be computed from

$$v_{\text{kick}} = 32V_0 \frac{q^2}{(1+q)^5} \sqrt{(1-q)^2 + 2(1-q)K \cos\theta + K^2}, \quad (5.1)$$

with  $K = k(q\chi_1 - \chi_2)$ . The fit parameters are  $V_0 = 276 \text{ km/s}$ ,  $\theta = 0.58 \text{ rad}$  and  $k = 0.85$ . For the zero total spin configuration considered in this section, we thus obtain  $v_{\text{kick}} = 246 \text{ km/s}$ . The authors of [179] give an error estimate of 10% on Eq. (5.1). Partially based on Eq. (5.1), refinements of the kick velocity have been proposed e.g. in [94], [182] and [89]. However, the emphasis of these later publication lied on the part of the kick which is in the direction perpendicular to the orbital angular momentum. The fit parameters for the in-plane kick have been corrected slightly, however the value for our configuration fluctuates at maximum by only  $3 \text{ km/s}$  if we use the different formulas proposed in the literature.

Our numerical result of  $v_{\text{kick,num}} = (227 \pm 6) \text{ km/s}$  thus deviates by 8.4% from the analytic value obtained with Eq. (5.1), which is inside the error range of 10% given by the authors of [179]. We have to keep in mind that the simulations they used do not cover the parameters we have here, but treat only smaller mass ratios and smaller spin magnitudes. This may also be a reason for the relatively large error. We will also need higher resolution at the outermost extraction radii in the numerical simulations

in order to more accurately determine the recoil from the numerical data.

Since the value of the kick velocity is only about  $v_{\text{kick}} = 140$  km/s in the non-spinning configuration (compare Tab. 5.4), which is lower than what we found for the zero total spin runs, even when we take into account the errors, we see that it is not the value of the total spin which affects the recoil velocity, but the individual spins.

## 5.3 Hybrid Waveforms and Phenomenological Templates

The improved accuracy of today's available NR waveforms opens the possibility to construct highly accurate GW templates for use in detector pipelines. There are in principal two different routes to template construction. The effective-one-body framework [141, 158, 184] sets up analytical, physically motivated waveforms modeling the compact binary by a single particle moving in an effective potential. There are still some free parameters in the model which have not (yet) been calculated analytically, but which are determined to date by results from numerical relativity. Accurate non-spinning templates were thus obtained in [68, 158, 185–187]. Work is under way to include also spins in the model, which has been done in [188] for binaries with equal masses and spins aligned or anti-aligned with the orbital angular momentum. The waveforms provided by the NR groups in the NRAR project [157] will help to further improve and extend this model.

The second approach, and the one we will consider in more detail here, is a phenomenological one. A number of waveforms serve as data set for the determination of certain phenomenological parameters in a waveform model via fitting. The phenomenological parameters are finally mapped to the physical ones. The first templates of this sort were built for non-spinning binaries in [189–191] including mass ratios up to  $q = 3$ . This approach has been extended to spinning binaries, which up to now are searched for by non-spinning templates, only, for the first time in [DM5] and in [73]. Since both of these constructions use, among others, the highly accurate BAM waveforms presented in [DM4], we briefly review in this chapter how the templates are built.

Since the NR waveforms only start in the late inspiral, especially for low masses,

Set	$q$	Spins ( $\chi_i$ )	Code/Source
1	1	$\pm\{0.25, 0.5, 0.75, 0.85\}$	BAM (“+” [178], “−” [DM4])
2	$\{2, 2.5, 3\}$	$\{\pm 0.5, 0.75\}$	BAM
3	$\{1, 1.5, 2, 2.5, 3, 3.5, 4\}$	0	BAM
4	$\{2, 3\}$	$(\chi_1, \chi_2) = (-0.75, 0.75)$	BAM
5	1	$\chi_1 \in \pm\{0.2, 0.3, 0.4, 0.6\}, \chi_2 = -\chi_1$	CCATIE
6	1	$\vec{S}_1 = (0.42, 0, 0.42), \vec{S}_2 = 0$ $\vec{S}_1 = (0.15, 0, 0), \vec{S}_2 = 0$	LLAMA
7	3	$\vec{S}_1 = (0.75, 0, 0), \vec{S}_2 = 0$	BAM
8	1	0	[192]
9	1.25	$\vec{S}_1 = (-0.09, 0.48, 0.35),$ $\vec{S}_2 = (-0.2, -0.14, 0.32)$	[74]

**Table 5.5:** Parameters of simulations used to build hybrid waveforms (Sets 1–3) and to test the phenomenological template family (Sets 4–9). The second column is the mass ratio,  $q = M_2/M_1$ . The third column gives the magnitude of the spins,  $\chi_i$ , when they are aligned (positive sign) or anti-aligned (negative sign) to the orbital angular momentum, otherwise the full spin vectors are written down explicitly. In the fourth column, the code used to produce the sets or the reference to the according publication is given. See [92] for a description of CCATIE and [193, 194] for LLAMA. The BAM waveforms were computed at extraction radius  $R_{\text{ex}} = 90 M$ , the one computed with CCATIE at  $R_{\text{ex}} = 160 M$ , and the LLAMA waveforms are extracted at null infinity [195].

they describe only part of what could be detected [196]. It is therefore natural to extend the NR waveform with information from PN theory such that we obtain a signal covering a very large part of the inspiral, the merger and the ringdown. The waveform obtained from stitching together PN and NR waveforms is called a hybrid waveform. Since PN models become inaccurate near merger, the NR waveforms need to be long enough to allow for an early matching time. This ensures that the PN part is still a valid approximation in the matching region. It has been studied in [197] how long NR waveforms need to be in order to ensure a certain accuracy of the hybrid waveforms.

In [DM5], hybrid waveforms are constructed in the time domain using NR simulations of different codes and groups. The entity of configurations can be found in Tab. 5.5. In summary, simulations with equal and unequal masses up to  $q = 4$  were used. Most of the configurations have vanishing or non-precessing spins, e.g. spin vectors aligned or anti-aligned with the orbital angular momentum, but there are also some more general, precessing configurations present. All of the waveforms contain at

least eight GW cycles before merger and are thus long enough for matching with PN inspiral waveforms. For the time being, only the  $l = m = 2$  mode is used. In a time interval  $[t_1, t_2]$  during inspiral, where both PN and NR are valid, a smooth transition from one description to the other is modeled. Since PN waveforms are given in terms of the gravitational wave strain  $h$ , but the NR waveforms are computed in terms of  $\Psi_4$  (see Eq. (2.24)), and since the detector outputs the strain, we are interested in a model function for the strain rather than for  $\Psi_4$ . This is why the NR waveforms have to be integrated twice in time before the matching can be performed. An appropriate choice of the two integration constants is necessary, and the procedures which have been discussed in Sec. 2.4.2 are used. In contrast, in [73] this problem is elegantly avoided by matching PN and NR waveforms not in time, but in frequency domain. As discussed in Sec. 2.4.2, too, integrating twice in time means multiplying by the square of the frequency in Fourier domain. The matching is now performed in a frequency interval  $[\omega_1, \omega_2]$  which is valid because for BBH systems, the frequency increases monotonically during inspiral.

The time domain hybrid construction uses the TaylorT1 [198] method to construct the PN phase including the highest available PN orders [199] and spin terms [148, 200]. In comparisons of different Taylor approximants to numerical simulations in [178] and [DM4], it turned out that the TaylorT1 approach gives the best overall performance in the sense that the phase difference to numerical waveforms over a certain amount of GW cycles is small for general configurations (see e.g. Eq. (11) in [DM4] for a definition of “phase difference”). For the frequency domain hybrid construction, the TaylorF2 phase is used [198, 201–203]. The PN amplitude is built from the results of [204, 205], including corrections for (anti-)aligned spins. In the cases of precessing spins, the results of [200, 206] are used to evolve the spins and angular momenta. This amplitude is transformed into Fourier domain for the frequency domain hybrids using the stationary phase approximation

We want to briefly comment on the choice of the TaylorT1 approximation for the PN phase in the time domain hybrids. In non-spinning cases, better agreement with the NR results has actually been found with TaylorT4 (see e.g. [63]) than with T1, see e.g. the comparisons in [63] for equal masses and in [DM4] for unequal ones. However, the results of [DM6] indicate that the agreement with TaylorT1 is better than with T4 provided that the NR waveforms are extrapolated to infinite extraction radius. In this publication, simulations of a non-spinning binary with mass ratio

$q = 4$  and initial separation  $D = 11 M$ , computed using the LEAN code [67], and the  $D = 10 M$  simulation of the BAM code included in the study of [DM4] and employed in the comparison to the results of dynamical damping in Sec. 4.4.1, are used to compare the NR results to TaylorT1 and TaylorT4 at different extraction radii. The comparisons are done for the dominant  $l = m = 2$  mode as well as for several subdominant modes. The waves are extrapolated to infinite extraction radius using a fall-off in the error as  $1/R_{\text{ex}}$  or  $1/R_{\text{ex}} + 1/R_{\text{ex}}^2$ . The error in this extrapolation is  $\Delta\phi \leq 0.15$  up to  $M\omega = 0.1$  for the waveforms considered. PN and NR waveforms are matched using different matching windows during inspiral, as well as the point where the GW frequency reaches  $M\omega = 0.1$ . The qualitative results, however, do not change. At finite extraction radii, the accumulated phase difference measured in the frequency range  $M\omega \simeq 0$  to  $M\omega = 0.1$  is larger between NR and TaylorT1 than between NR and TaylorT4. This agrees with what has been found for the BAM waveform and for a number of other non-spinning waves in [DM4]. For the extrapolated waveforms, however, the phase disagreement is significantly smaller for TaylorT1 than for TaylorT4. This holds for all the modes included in the comparisons. For the BAM waveform, Fig. 5.7 shows these comparisons. In this figure, the  $(l = m = 2)$  and the  $(l = 3, m = 2)$ -modes are included. While the accumulated phase difference for TaylorT1 (left panel) is 0.3 rad at  $M\omega = 0.1$ , we find an accumulated phase difference of 0.4 rad for TaylorT4 (right panel). For the LEAN waveform, this difference is even more pronounced. There, the T1 phase differs by 0.5 rad from the extrapolated phase of the 22-mode, whereas the T4 phase differs by 1 rad. This finding reinforces the earlier belief that the nice agreement of NR and TaylorT4 was coincidental and supports the usage of TaylorT1 in the construction of time domain hybrid waveforms.

Now an appropriate model for amplitude and phase is needed which can be fitted to (part of) the hybrid data just obtained. Since in general, spins add six parameters to a template, which drastically increases the cost of a search algorithm in matched filtering, here the spins are modeled by a single parameter, that is  $\chi \equiv (1 + \delta)\chi_1/2 + (1 - \delta)\chi_2/2$  is used, where  $\delta \equiv (M_1 - M_2)/M$  and  $\chi_i \equiv S_i/M_i^2$  with  $S_i$  the spin magnitude of the  $i^{\text{th}}$  BH. Waveform templates for binaries with equal masses and precessing spins, where the precession is also taken into account in the template construction, are built in [207, 208]. However, the authors of these publications suggest to use their templates as injection waveforms to test the existing

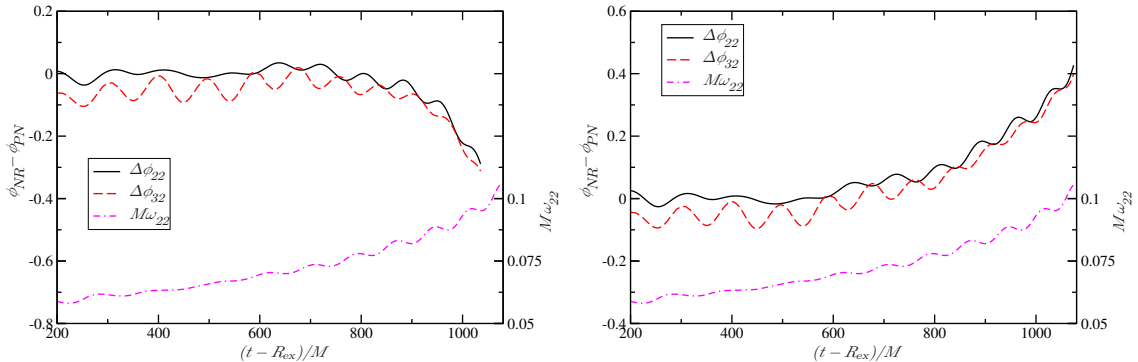


**Figure 5.7:** Phase difference between the numerical waveform for  $q = 4$ ,  $D = 10 M$  obtained with BAM and the TaylorT1 (left panel) and TaylorT4 approximation (right panel). The NR modes are extrapolated to infinite extraction radius. The comparisons for the  $l = m = 2$  mode (black solid line) and the  $l = 3, m = 2$  mode (red dashed line) are shown. PN and NR modes are matched in a time window  $[250 M, 600 M]$ . As a reference only, the GW frequency of the 22–mode,  $M\omega_{22}$ , is shown, too.

data analysis pipelines and not as detection templates because of the just mentioned increase in physical parameters.

The phenomenological model is constructed in the frequency domain such that it can directly be employed in GW searches. The instantaneous GW frequency of a quasi-circular BBH inspiral and coalescence can be used to divide the waveform into parts, depending on its value: inspiral for  $f < f_1$ , merger for  $f_1 \leq f < f_2$  and ringdown for  $f_2 \leq f < f_3$ , with the exact values of  $f_1, f_2$  and  $f_3$  to be determined by the fit to the data. The amplitude model  $A(f)$  of [DM5] is now split into these three regimes and the phase ansatz  $\Psi(f)$  is a polynomial in the GW frequency,

$$A(f) \equiv C f_1^{-7/6} \begin{cases} f'^{-7/6} (1 + \sum_{i=2}^3 \alpha_i v^i) & \text{if } f < f_1, \\ w_m f'^{-2/3} (1 + \sum_{i=1}^2 \epsilon_i v^i) & \text{if } f_1 \leq f < f_2, \\ w_r \mathcal{L}(f, f_2, \sigma) & \text{if } f_2 \leq f < f_3, \end{cases}$$

$$\Psi(f) \equiv 2\pi f t_0 + \varphi_0 + \frac{3}{128\eta v^5} \left(1 + \sum_{k=2}^7 v^k \psi_k\right). \quad (5.2)$$

The transitions from one frequency regime to the next one are made continuous by adjusting the normalization constants  $w_m$  and  $w_r$ . We further have  $f' \equiv f/f_1$ ,  $v \equiv (\pi M f)^{1/3}$ ,  $\epsilon_1 = 1.4547\chi - 1.8897$ ,  $\epsilon_2 = -1.8153\chi + 1.6557$ ,  $C$  is a numerical constant depending on the sky-location, orientation and the masses,  $\alpha_2 = -323/224 + 451\eta/168$  and  $\alpha_3 = (27/8 - 11\eta/6)\chi$ ,  $t_0$  the time of arrival of the signal at the detector



and  $\varphi_0$  the corresponding phase.  $\mathcal{L}(f, f_2, \sigma)$  is a Lorentzian function with width  $\sigma$  centered around the frequency  $f_2$ .

The phenomenological parameters  $\{\psi_k\}_{k=2\dots 7}$  and  $\{f_1, f_2, \sigma, f_3\}$  are calibrated by fitting to the hybrids produced from data sets (1)–(3) in Tab. 5.5, i.e. only non-spinning waveforms and those with spins aligned or anti-aligned with the orbital angular momentum, are used. In addition, information from the test particle limit ( $1/q \rightarrow 0$ ) is used such that the templates can accurately model also waveforms slightly outside the parameters space of the available hybrids (e.g. up to  $q \leq 10$ ). Figure 5.8 shows how well the hybrid waveforms used to construct the phenomenological template are approximated by the latter. Here, we look at two quantities, the match and the fitting factor (FF). The ability of the template family to accurately reproduce a waveform with certain physical parameters is captured by evaluating the (faithfulness) match between the phenomenological and the true waveform,

$$\text{match} = \max_{t_0, \phi_0} \frac{\langle h_1, h_2 \rangle}{\sqrt{\langle h_1, h_1 \rangle \langle h_2, h_2 \rangle}}, \quad (5.3)$$

with

$$\langle h_1, h_2 \rangle = 4\Re \int_{f_{\min}}^{f_{\max}} \frac{h_1(f) \bar{h}_2(f)}{S_n(f)} df \quad (5.4)$$

a noise-weighted inner product between two waveforms  $h_1$  and  $h_2$ , where  $S_n(f)$  is the frequency dependent noise curve of the detector under consideration. Here, the design noise curve of Initial LIGO is used [209]. The maximization in Eq. (5.3) is performed over the time of arrival of the signal,  $t_0$ , and an overall phase shift,  $\phi_0$ . The higher the match, the better the waveform family can reproduce the parameters of a detected signal. If we are only interested in the question whether a template family can capture a certain signal, regardless of the physical parameters, the match has to be maximized over all physical parameters (spins and masses). This gives the fitting factor and expresses whether the template family is useful for detection, e.g. if it is effectual. No more than 10% of signals are missed if  $\text{FF} > 0.97$  [210].

The match and FF of the phenomenological template family of [DM5] with the hybrid waveforms of data sets (1)–(3) in Tab. 5.5 are displayed in the left two plots of Fig. 5.8. The templates are effectual in detection ( $\text{FF} > 0.97$ ) of the waveforms with spins aligned or anti-aligned with the orbital angular momentum and can accurately reproduce the hybrids, e.g. they are also faithful ( $\text{match} > 0.97$ ) for these configu-



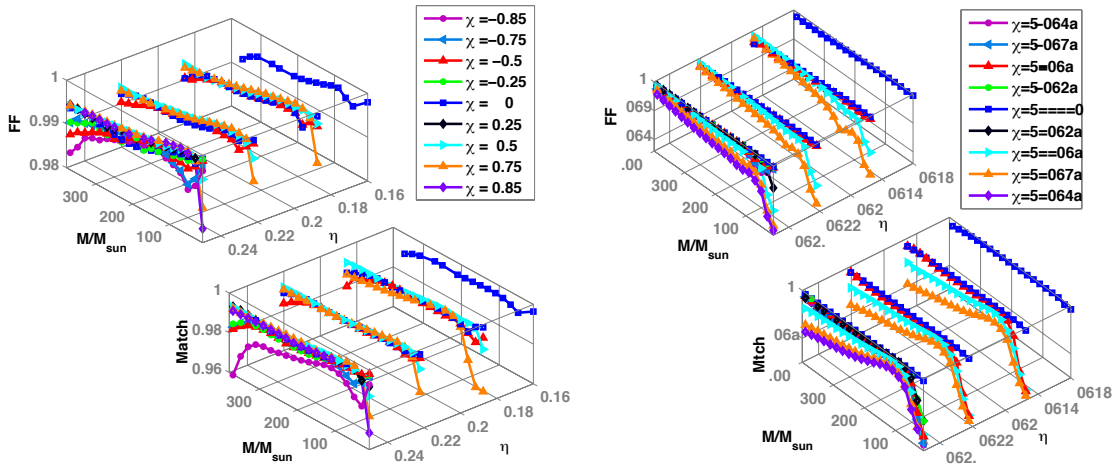


**Figure 5.8:** *Left:* FF and match of the phenomenological templates including spin, Eq. (5.2), with the equal-spin hybrid waveforms of simulation sets (1)–(3), using the Initial LIGO design noise curve [209]. In these plots,  $\eta$  is the symmetric mass ratio,  $\eta = M_1 M_2 / M$ , and  $M/M_{\text{sun}}$  is the total mass of the binary in terms of solar masses. The waveform model is always effectual because of  $\text{FF} > 0.97$  for all cases, and it is faithful ( $\text{Match} > 0.97$ ) in most of the mass range considered here. *Right:* FF and match of the non-spinning phenomenological templates produced in [189, 191] with the spinning waveforms of data sets (1)–(3). The templates are neither faithful nor effectual for detection of signals with non-zero spin. (Plots courtesy of P. Ajith.)

rations, even though the spin only enters the model through a single parameter. In contrast, using the non-spinning templates of [189, 191] to detect these spin waveforms, match and FF are below 0.97, which shows that those templates are neither faithful nor effectual for detection of spinning binaries.

The applicability of the spinning templates in detection of the hybrids produced from data sets (4)–(9) is also evaluated, and matches and FF with these waveforms can be found in Fig. 5.9. Although the templates were constructed using hybrids with equal spins (anti-)aligned with the orbital angular momentum only, they are effectual ( $\text{FF} > 0.97$ ) in detecting the unequal spin configurations (see the upper left panel of Fig. 5.9) and even the precessing waveforms in most of the mass range studied (see the lower panel of Fig. 5.9). When the masses are equal and the spins (anti-)aligned, the template family can accurately reproduce waveforms with unequal spin magnitudes, which can be seen from the yellow curves in the top right panel of Fig. 5.9, where the match is always above 0.97 for this data set. These results strongly suggest that representing spin by a single parameter, as is done in this model, is sufficient for the purpose of GW detection. This even seems to carry over to the case of precessing binaries, in particular when the precession does not involve flipping of the orbital

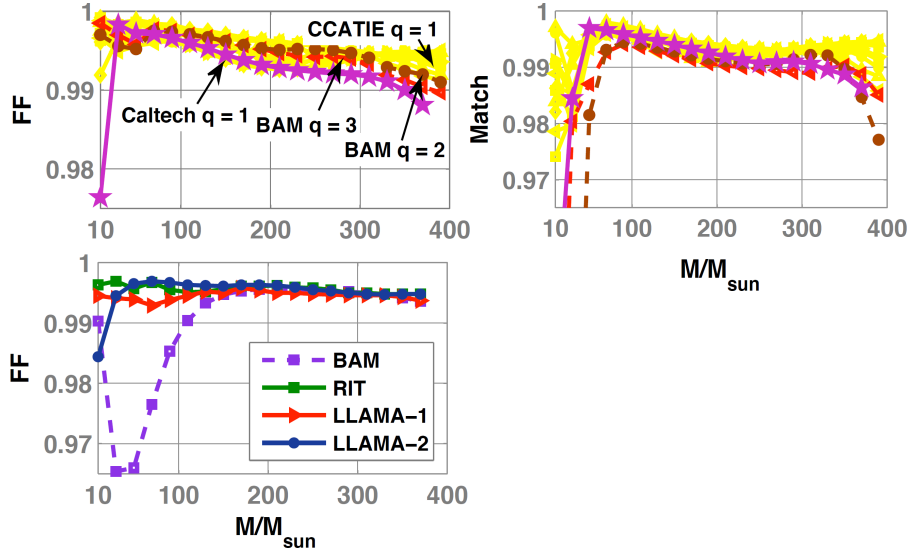


**Figure 5.9:** *Upper plots:* FF (left) and match (right) of the phenomenological templates Eq. (5.2) with unequal spin hybrids, data sets (4) (red and brown) and (5) (yellow), and data set (8) (pink), using the Initial LIGO design noise curve [209]. *Lower left:* FF of the phenomenological templates with precessing spin hybrids, data sets (6) (red and blue), (7) (purple) and (9) (green) (Plots courtesy of P. Ajith.)

plane. This is reassuring and will greatly simplify the search for spinning binaries.

The modeling of inspiral, merger and ringdown stages is slightly different in [73]. In those templates, the phase is divided in inspiral, merger and ringdown parts, too, but the amplitude model does not contain a merger portion. Instead of stitching together the individual waveform regimes at certain frequencies, [73] uses smooth transition windows, and the phenomenological parameters are obtained by fitting to nearly the same data as sets (1)–(3) here (except for  $q = 2.5$  in set (3) which is replaced by  $q = 4$ ), but the extreme mass ratio case is not considered. Using the Advanced LIGO design noise curve, the templates are shown to be effectual as well as faithful in detecting the data sets they were constructed from, and effectual in detection of additional (anti-)aligned NR waveforms which were not used in the template construction. Their performance was, however, not tested for precessing spin waveforms because the main focus of that work was to study the accuracy of the hybrid production procedure. Despite the differences in the construction of hybrids and in the phenomenological description of the waveforms, the spinning template waveforms of [73] agree well with those of [DM5] discussed in greater detail here [211].

The incorporation of the extreme mass ratio limit when building templates allows

---

to use them in a parameter range which is actually larger than the one of the NR waveforms used to construct the templates. Nevertheless, we need to include mass ratios larger than  $q = 4$  in the construction in order to make sure that the intermediate mass ratios are well covered. For this purpose, simulations for e.g.  $q = 10$  with eight to ten GW cycles before merger would greatly enhance the validity of the phenomenological templates.



## 6 Summary and Future Prospects

In this thesis we have presented the implementation of an analytic method to generate low-eccentricity initial parameters for the evolution of binary black holes. This algorithm relies on a Hamiltonian approach. In particular, we compared the use of a Taylor expanded Hamiltonian to the use of an effective-one-body (EOB) Hamiltonian, and used a Taylor expanded flux function as well as its Padé resummation. We investigated which combination results in the lowest eccentricity in numerical simulations. We examined physical systems with equal masses and equal spins aligned to the orbital angular momentum, for which only spin-orbit coupling is included in the analytical model. We compared to the results of the post-Newtonian integration method of [142] and found equally low or lower eccentricities with our method, except for the case where the spin magnitude is highest. Including spin-spin coupling terms for this configuration, we could, however, further reduce the eccentricity to a comparable level. For all these spinning configurations, we found that using the EOB Hamiltonian results in a lower eccentricity than the Taylor expanded Hamiltonian. Additionally, we tested the algorithm for non-spinning binaries with mass ratios from one up to ten. As anticipated, the Taylor Hamiltonian gives lower values of eccentricity for mass ratios close or equal to one, while for higher mass ratios the EOB Hamiltonian performs better for our purposes. In addition, we found that the choice of flux function did not influence the resulting eccentricity in any of the cases studied. Guided by these findings, we used our method with the EOB Hamiltonian to produce initial parameters for a binary with mass ratio two and vanishing total spin, but non-vanishing individual spins, for the Numerical Relativity Analytical Relativity (NRAR) project. The resulting eccentricity was low enough to match the NRAR specification without requiring any further tuning. In the future, it would be interesting to implement the most recently published Hamiltonians in our algorithm, and to extend it such that more general spin configurations can be treated as well.

We then turned to the question of how to stably evolve unequal mass black hole

binaries in numerical relativity. It had been known for some time that the popular Gamma driver condition leads to an instability in the shift vector for certain values of the damping parameter in combination with certain grid setups, which is directly related to instabilities found in binary simulations with a mass ratio significantly different from one. We circumvent this problem by setting up damping which varies over the numerical grid, thereby taking into account variations in the local mass, since the damping term is inversely proportional to the mass scale. We developed a formula for the damping term which uses the conformal factor to track the local mass, and checked in a simulation of a single puncture that the modified gauge condition only introduces coordinate changes. We compared results on the waveforms using this modified gauge to previously available waveforms computed with constant damping, and we found lower errors in amplitude and phase of the 22-mode. Our approach was slightly modified and used to obtain the first simulation with a mass ratio as high as 100:1 in [25]. Since we found that during evolution the damping parameter is contaminated by noise which is amplified as it leaves the grid towards the outer boundary, we set up a second form for the dynamical damping. This second formula does not rely on any of the evolution variables but is purely analytic. We demonstrated the benefits of using this formula in simulations of binaries with mass ratio 4:1. Phase and amplitude error of the 22-mode of the extracted gravitational waves reduced significantly compared to constant damping, which indicates a higher effective resolution of the black holes on the numerical grid. The increased phase accuracy carried over to a more accurate estimate of the kick velocity. An increase in phase and amplitude accuracy without the need to use more numerical resources is particularly beneficial in simulations with high mass ratios, since they are computationally much more expensive than those with equal masses.

Varying the box sizes in the wave zone of the numerical grid we demonstrated how to achieve yet a higher accuracy in the gravitational waves while the growth in computational cost is moderate. We used different setups of a spinning binary for these analyses and showed that also the strongest subdominant mode, the 44-mode in this case, improved considerably. Having very accurate binary black hole simulations at hand, we presented phenomenological waveform templates which for the first time include spin. The templates are shown to be “effectual” in the detection of non-spinning binaries with equal and unequal masses, as well as of equal mass binaries with generic spins. This is remarkable because the templates are constructed from

---

equal spin binaries and binaries without spins (but mass ratios above one), and the spins are modelled by a single parameter only. This is a great improvement since adding only a single parameter for spin allows for the use of these templates in the detection of gravitational waves, and they may replace the non-spinning templates nowadays also used in the search for spinning binaries, which leads to a loss of up to 50% of signals.

In these templates, only binaries with mass ratios up to four were available for the calibration of the phenomenological parameters. We plan to use our method with location-dependent damping term in the Gamma driver shift condition to produce very accurate simulations of binaries with mass ratio 10:1 and higher, covering about ten orbits. Since the higher the mass ratio, the more important subdominant modes become, we will use the insights in the grid structure gained here to allow for a very accurate calculation of these modes, too. Accurately tracking the phase over a very long time of simulation is the challenge to be met in these simulations. Such accurate waveforms with high mass ratio can then be incorporated in the phenomenological templates, which naturally extends the range of their validity.

Concerning dynamical damping, a study of the stability properties of the Baumgarte–Shapiro–Shibata–Nakamura system with 1+log slicing and Gamma driver shift with an extra evolution equation for the damping term would be very interesting. Furthermore, the performance of our formula for location dependent damping can presumably be improved further by incorporating ideas of [168, 176] who make the damping term fall to zero towards the outer boundary. We also plan to eliminate the width parameters from our analytical formula, making it directly applicable to any black hole binary with any grid setup. Finally, the location dependent damping has to be used and tested in simulations of spinning binaries. We want to study unequal mass binaries with non-vanishing individual spins, which has only been done rarely up to the present.





# List of Publications

- [DM1] B. WALTHER, B. BRÜGMANN, and D. MÜLLER. *Numerical black hole initial data with low eccentricity based on post-Newtonian orbital parameters*. Phys. Rev., D79:124040 (2009).
- [DM2] D. MÜLLER and B. BRÜGMANN. *Toward a dynamical shift condition for unequal mass black hole binary simulations*. Class. Quant. Grav., 27:114008 (2010).
- [DM3] D. MÜLLER, J. GRIGSBY, and B. BRÜGMANN. *Dynamical shift condition for unequal mass black hole binaries*. Phys. Rev., D82:064004 (2010).
- [DM4] M. HANNAM, S. HUSA, F. OHME, D. MÜLLER, and B. BRÜGMANN. *Simulations of black-hole binaries with unequal masses or nonprecessing spins: Accuracy, physical properties, and comparison with post-Newtonian results*. Phys. Rev., D82:124008 (2010).
- [DM5] P. AJITH, M. HANNAM, S. HUSA, Y. CHEN, B. BRÜGMANN, N. DORBAND, D. MÜLLER, F. OHME, D. POLLNEY, C. REISSWIG, L. SANTAMARIA, and J. SEILER. *'Complete' gravitational waveforms for black-hole binaries with non-precessing spins*. Phys. Rev. Lett., 106:241101 (2011).
- [DM6] U. SPERHAKE, B. BRÜGMANN, D. MÜLLER, and C. F. SOPUERTA. *Black-hole binaries go to eleven orbits* (2010). Accepted for publication in Class. Quant. Grav., [arXiv:1012.3173\[gr-qc\]](https://arxiv.org/abs/1012.3173).

- [DM7] B. BRÜGMANN, U. SPERHAKE, D. MÜLLER, R. GOLD, P. GALAVIZ, N. LAGES, and M. THIERFELDER. *Dynamics of Binary Black Hole Systems*. S. WAGNER, M. STEINMETZ, A. BODE, and M. MÜLLER, (Eds.) *High Performance Computing in Science and Engineering, Garching/Munich 2009*. Springer, 1st ed. (2010). ISBN 978-3-642-13871-3.

# List of Presentations

- [P1] J. GONZALEZ, U. SPERHAKE, B. BRÜGMANN, and **D. MÜLLER**. *Numerical Simulations of Black Hole Binaries with Mass Ratios from 1:1 to 10:1*. Aug., 2008. Talk at 2008 NRDA meeting, Syracuse University, Syracuse, USA.
- [P2] **D. MÜLLER**, B. WALTHER, and B. BRÜGMANN. *LISA Germany meeting: Update from Jena*. Oct., 2008. Talk at LISA Germany meeting, AEI, Golm, Germany.
- [P3] **D. MÜLLER** and B. BRÜGMANN. *LISA Germany meeting: Update from Jena*. June, 2009. Talk at LISA Germany meeting, ZARM, Bremen, Germany.
- [P4] B. WALTHER, B. BRÜGMANN, and **D. MÜLLER**. *Numerical black hole initial data with low eccentricity based on post-Newtonian orbital parameters*. March, 2009. Talk at DPG spring meeting, LMU, Munich, Germany.
- [P5] **D. MÜLLER** and B. BRÜGMANN. *Dynamical gauge conditions for binary black hole numerical relativity simulations*. June, 2009. Talk at 8th Eduardo Amaldi Conference on Gravitational Waves, Columbia University, New York City, USA.
- [P6] **D. MÜLLER** and B. BRÜGMANN. *Dynamical gauge conditions for binary black hole numerical relativity simulations*. July, 2009. Talk at 2009 NRDA meeting, AEI, Golm, Germany.
- [P7] **D. MÜLLER** and B. BRÜGMANN. *Dynamical gauge conditions for binary black*

- hole numerical relativity simulations*. July, 2009. Talk at 12th Marcel Grossmann Meeting, UNESCO Headquarters, Paris, France.
- [P8] B. BRÜGMANN, **D. MÜLLER**, N. LAGES, and R. GOLD. *Schwarze Löcher und Gravitationswellen – was Einstein nicht sehen konnte*. Nov., 2009. Public talk at Lange Nacht der Wissenschaften, TPI, Jena, Germany.
- [P9] **D. MÜLLER**, J. GRIGSBY, and B. BRÜGMANN. *Dynamical shift condition for unequal mass black hole binary simulations*. March, 2010. Talk at DPG spring meeting, LMU, Munich, Germany.
- [P10] **D. MÜLLER**, J. GRIGSBY, and B. BRÜGMANN. *Dynamical shift condition for unequal mass black hole binary simulations*. June, 2010. Poster presentation at 2010 NRDA meeting, Perimeter Institute, Waterloo, Canada.
- [P11] **D. MÜLLER**, J. GRIGSBY, and B. BRÜGMANN. *Dynamical shift condition for unequal mass black hole binary simulations*. July, 2010. Poster presentation at 8th International LISA Symposium, Stanford University, Palo Alto, USA.

# Bibliography

- [1] A. EINSTEIN. *Zur Allgemeinen Relativitätstheorie*. Preuss. Akad. Wiss. Berlin, Sitzungsber., pp. 778–786 (1915)
- [2] A. EINSTEIN. *Die Feldgleichungen der Gravitation*. Preuss. Akad. Wiss. Berlin, Sitzungsber., pp. 844–847 (1915)
- [3] B. S. SATHYAPRAKASH and B. F. SCHUTZ. *Physics, Astrophysics and Cosmology with Gravitational Waves*. Living Rev. Rel., 12: 2 (2009)
- [4] A. A. ABRAMOVICI, W. ALTHOUSE, R. P. DREVER, *et al.* *LIGO: The Laser Interferometer Gravitational-Wave Observatory*. Science, 256: 325 (1992)
- [5] F. ACERNESE, F. AMICO, M. ALSHOURBAGY, *et al.* *The VIRGO status*. Class. Quantum Grav., 23: S635 (2006)
- [6] S. HILD and THE LIGO SCIENTIFIC COLLABORATION. *The status of GEO 600*. Class. Quantum Grav., 23: S643 (2006)
- [7] B. WILLKE. *GEO600: Status and plans*. Class. Quant. Grav., 24: S389 (2007)
- [8] M. ANDO *et al.* *Current status of the tama300 gravitational wave detector*. Class. Quantum Grav., 22: S881 (2005)
- [9] G. HEINZEL, C. BRAXMAIER, K. DANZMANN, *et al.* *LISA interferometry: recent developments*. Classical and Quantum Gravity, 23 (8): S119 (2006)
- [10] S. KAWAMURA, T. NAKAMURA, M. ANDO, *et al.* *The japanese space gravitational wave antenna — DECIGO*. Classical and Quantum Gravity, 23 (8): S125 (2006)
- [11] L. BLANCHET. *Gravitational Radiation from Post-Newtonian Sources and Inspiralling Compact Binaries*. Living Reviews in Relativity, 9 (4) (2006)
- [12] G. SCHÄFER. chap. Post-Newtonian methods: Analytic results on the binary problem. Springer (2009). ISBN 978-90-481-3014-6
- [13] K. D. KOKKOTAS and B. G. SCHMIDT. *Quasi-normal modes of stars and black holes*. Living Rev. Relativity, 2: 2 (1999). [Http://www.livingreviews.org/lrr-1999-2](http://www.livingreviews.org/lrr-1999-2)
- [14] T. DAMOUR and A. NAGAR. *The Effective One Body description of the Two-Body problem* (2009)
- [15] B. AYLOTT, J. G. BAKER, W. D. BOGGS, *et al.* *Testing gravitational-wave*

- searches with numerical relativity waveforms: Results from the first Numerical INJECTION Analysis (NINJA) project.* *Class. Quant. Grav.*, 26: 165008 (2009)
- [16] B. AYLOTT, J. G. BAKER, W. D. BOGGS, *et al.* *Status of NINJA: the Numerical INJECTION Analysis project.* *Class. Quant. Grav.*, 26: 114008 (2009)
- [17] F. PRETORIUS. *Evolution of binary black hole spacetimes.* *Phys. Rev. Lett.*, 95: 121101 (2005)
- [18] M. CAMPANELLI, C. O. LOUSTO, P. MARRONETTI, *et al.* *Accurate evolutions of orbiting black-hole binaries without excision.* *Phys. Rev. Lett.*, 96: 111101 (2006)
- [19] J. G. BAKER, J. CENTRELLA, D.-I. CHOI, *et al.* *Gravitational wave extraction from an inspiraling configuration of merging black holes.* *Phys. Rev. Lett.*, 96: 111102 (2006)
- [20] A. SESANA, M. VOLONTERI, and F. HAARDT. *The imprint of massive black hole formation models on the LISA data stream.* *Mon. Not. Roy. Astron. Soc.*, 377: 1711 (2007)
- [21] L. A. GERGELY and P. L. BIERMANN. *Supermassive black hole binary mergers.* *Astrophys. J.*, 697: 1621 (2009)
- [22] M. VOLONTERI and P. MADAU. *Off-nuclear AGN as a signature of recoiling massive black holes.* *The Astrophysical Journal Letters*, 687 (2): L57 (2008)
- [23] E. POISSON. *The motion of point particles in curved spacetime.* *Living Reviews in Relativity*, 7 (6) (2004). [Http://www.livingreviews.org/lrr-2004-6](http://www.livingreviews.org/lrr-2004-6)
- [24] M. SASAKI and H. TAGOSHI. *Analytic black hole perturbation approach to gravitational radiation.* *Living Reviews in Relativity*, 6 (6) (2003)
- [25] C. O. LOUSTO and Y. ZLOCHOWER. *Orbital Evolution of Extreme-Mass-Ratio Black-Hole Binaries with Numerical Relativity.* *Phys. Rev. Lett.*, 106: 041101 (2011)
- [26] C. W. MISNER, K. S. THORNE, and J. A. WHEELER. *Gravitation.* W. H. Freeman, New York (1973)
- [27] J. W. YORK, JR. *Kinematics and dynamics of general relativity.* L. SMARR (Ed.), *Sources of Gravitational Radiation*, pp. 83–126. Cambridge University Press, Cambridge (1979)
- [28] T. W. BAUMGARTE and S. L. SHAPIRO. *On the Numerical integration of Einstein's field equations.* *Phys. Rev. D*, 59: 024007 (1998)
- [29] M. SHIBATA and T. NAKAMURA. *Evolution of three-dimensional gravitational waves: Harmonic slicing case.* *Phys. Rev. D*, 52: 5428 (1995)
- [30] M. ALCUBIERRE, G. ALLEN, B. BRÜGMANN, *et al.* *Towards an understanding of the stability properties of the 3+1 evolution equations in general relativity.*

- Phys. Rev. D, 62: 124011 (2000). Gr-qc/9908079
- [31] O. SARBACH, G. CALABRESE, J. PULLIN, *et al.* *Hyperbolicity of the BSSN system of Einstein evolution equations.* Phys. Rev. D, 66: 064002 (2002)
- [32] C. BONA, J. MASSÓ, E. SEIDEL, *et al.* *A New Formalism for Numerical Relativity.* Phys. Rev. Lett., 75: 600 (1995)
- [33] C. BONA, J. MASSÓ, E. SEIDEL, *et al.* *First order hyperbolic formalism for numerical relativity.* Phys. Rev. D, 56: 3405 (1997). Gr-qc/9709016
- [34] C. BONA, T. LEDVINKA, C. PALENZUELA, *et al.* *General-covariant evolution formalism for numerical relativity.* Phys. Rev. D, 67: 104005 (2003)
- [35] C. BONA and C. PALENZUELA. *Dynamical shift conditions for the  $Z_4$  and BSSN hyperbolic formalisms.* Phys. Rev. D, 69: 104003 (2004)
- [36] C. GUNDLACH, J. M. MARTIN-GARCIA, G. CALABRESE, *et al.* *Constraint damping in the  $Z_4$  formulation and harmonic gauge.* Class. Quantum Grav., 22: 3767 (2005)
- [37] S. BERNUZZI and D. HILDITCH. *Constraint violation in free evolution schemes: Comparing BSSNOK with a conformal decomposition of  $Z_4$ .* Phys.Rev., D81: 084003 (2010)
- [38] M. ALCUBIERRE. *Introduction to 3+1 Numerical Relativity (International Series of Monographs on Physics).* Oxford University Press, USA (2008). ISBN 0199205671
- [39] H. FRIEDRICH. *On the hyperbolicity of Einstein's and other gauge field equations.* Comm. Math. Phys., 100: 525 (1985)
- [40] D. GARFINKLE. *Harmonic coordinate method for simulating generic singularities.* Phys. Rev. D, 65: 044029 (2002)
- [41] F. PRETORIUS. *Numerical relativity using a generalized harmonic decomposition.* Class.Quant.Grav., 22: 425 (2005)
- [42] S. G. HAHN and R. W. LINDQUIST. *The two body problem in geometrodynamics.* Ann. Phys., 29: 304 (1964)
- [43] A. LICHNEROWICZ. *L'intégration des équations de la gravitation relativiste et le problème des  $n$  corps.* J. Math. Pures et Appl., 23: 37 (1944)
- [44] M. ALCUBIERRE, B. BRÜGMANN, D. POLLNEY, *et al.* *Black hole excision for dynamic black holes.* Phys. Rev. D, 64: 061501(R) (2001)
- [45] M. ALCUBIERRE, B. BRÜGMANN, P. DIENER, *et al.* *Gauge conditions for long-term numerical black hole evolutions without excision.* Phys. Rev. D, 67: 084023 (2003)
- [46] B. REIMANN. *Slice stretching at the event horizon when geodesically slicing the*

- Schwarzschild spacetime with excision.* Class. Quantum Grav., 21: 4297 (2004)
- [47] B. REIMANN. *How slice stretching arises when maximally slicing the Schwarzschild spacetime with vanishing shift.* Class. Quantum Grav., 22: 4563 (2005)
- [48] E. SEIDEL and W.-M. SUEN. *Towards a singularity-proof scheme in numerical relativity.* Phys. Rev. Lett., 69 (13): 1845 (1992)
- [49] J. THORNBURG. *Coordinates and boundary conditions for the general relativistic initial data problem.* Class. Quantum Grav., 4: 1119 (1987)
- [50] P. ANNINOS, G. DAUES, J. MASSÓ, *et al.* *Horizon boundary condition for black hole spacetimes.* Phys. Rev. D, 51: 5562 (1995)
- [51] L. SMARR and J. W. YORK. *Kinematical conditions in the construction of spacetime.* Phys. Rev. D, 17 (10): 2529 (1978)
- [52] L. L. SMARR and J. W. YORK, JR. *Radiation gauge in general relativity.* Physical Review D, 17 (8): 1945 (1978)
- [53] M. ALCUBIERRE and B. BRÜGMANN. *Simple excision of a black hole in 3+1 numerical relativity.* Phys. Rev. D, 63: 104006 (2001)
- [54] J. BALAKRISHNA, G. DAUES, E. SEIDEL, *et al.* *Coordinate conditions in three-dimensional numerical relativity.* Class. Quantum Grav., 13: L135 (1996)
- [55] L. LINDBLOM and M. A. SCHEEL. *Dynamical gauge conditions for the Einstein evolution equations.* Phys. Rev. D, 67: 124005 (2003)
- [56] L. LINDBLOM and B. SZILÁGYI. *An Improved Gauge Driver for the GH Einstein System.* Phys. Rev., D80: 084019 (2009)
- [57] J. R. VAN METER, J. G. BAKER, M. KOPPITZ, *et al.* *How to move a black hole without excision: gauge conditions for the numerical evolution of a moving puncture.* Phys. Rev. D, 73: 124011 (2006)
- [58] H. BEYER and O. SARBACH. *On the well posedness of the Baumgarte-Shapiro-Shibata-Nakamura formulation of Einstein's field equations.* Phys. Rev. D, 70: 104004 (2004)
- [59] C. GUNDLACH and J. M. MARTIN-GARCIA. *Well-posedness of formulations of the Einstein equations with dynamical lapse and shift conditions.* Phys. Rev. D, 74: 024016 (2006)
- [60] B. F. SCHUTZ. *A first course in general relativity.* Cambridge University Press (1985)
- [61] B. BRÜGMANN, J. A. GONZÁLEZ, M. HANNAM, *et al.* *Calibration of Moving Puncture Simulations.* Phys. Rev., D77: 024027 (2008)
- [62] E. T. NEWMAN and R. PENROSE. *An approach to gravitational radiation by*



- a method of spin coefficients.* J. Math. Phys., 3 (3): 566 (1962). Erratum in J. Math. Phys. 4, 998 (1963)
- [63] M. BOYLE, D. A. BROWN, L. E. KIDDER, *et al.* *High-accuracy comparison of numerical relativity simulations with post-Newtonian expansions.* Phys. Rev., D76: 124038 (2007)
- [64] M. HANNAM, S. HUSA, J. A. GONZÁLEZ, *et al.* *Where post-Newtonian and numerical-relativity waveforms meet.* Phys. Rev. D, 77: 044020 (2008)
- [65] E. T. NEWMAN and R. PENROSE. *Note on the Bondi-Metzner-Sachs group.* J. Math. Phys., 7 (5): 863 (1966)
- [66] C. REISSWIG and D. POLLNEY. *Notes on the integration of numerical relativity waveforms* (2010)
- [67] U. SPERHAKE. *Binary black-hole evolutions of excision and puncture data.* Phys. Rev., D76: 104015 (2007)
- [68] T. DAMOUR, A. NAGAR, M. HANNAM, *et al.* *Accurate Effective-One-Body waveforms of inspiralling and coalescing black-hole binaries.* Phys. Rev., D78: 044039 (2008)
- [69] E. BERTI, V. CARDOSO, J. A. GONZÁLEZ, *et al.* *Inspiral, merger and ringdown of unequal mass black hole binaries: A multipolar analysis.* Phys. Rev., D76: 064034 (2007)
- [70] L. BAIOTTI, S. BERNUZZI, G. CORVINO, *et al.* *Gravitational-Wave Extraction from Neutron Stars Oscillations: comparing linear and nonlinear techniques.* Phys. Rev., D79: 024002 (2009)
- [71] S. BERNUZZI, L. BAIOTTI, G. CORVINO, *et al.* *Gravitational-wave extraction from neutron-star oscillations* (2009)
- [72] B. VAISHNAV, I. HINDER, F. HERRMANN, *et al.* *Matched filtering of numerical relativity templates of spinning binary black holes.* Phys. Rev., D76: 084020 (2007)
- [73] L. SANTAMARIA, F. OHME, P. AJITH, *et al.* *Matching post-Newtonian and numerical relativity waveforms: systematic errors and a new phenomenological model for non-precessing black hole binaries.* Phys. Rev., D82: 064016 (2010)
- [74] M. CAMPANELLI, C. O. LOUSTO, H. NAKANO, *et al.* *Comparison of Numerical and Post-Newtonian Waveforms for Generic Precessing Black-Hole Binaries.* Phys. Rev., D79: 084010 (2009)
- [75] R. ARNOWITT, S. DESER, and C. W. MISNER. *The dynamics of general relativity.* L. WITTEN (Ed.), *Gravitation: An introduction to current research*, pp. 227–265. John Wiley, New York (1962)
- [76] J. W. YORK. *Energy and momentum of the gravitational field.* F. J. TIPLER

- (Ed.), *Essays in General Relativity: A Festschrift for Abraham Taub*, pp. 39–58. Academic Press, New York (1980). ISBN 0-12-691380-3
- [77] N. O’MURCHADHA and J. W. YORK. *Gravitational energy*. Phys. Rev. D, 10 (8): 2345 (1974)
- [78] J. A. GONZÁLEZ, U. SPERHAKE, and B. BRÜGMANN. *Black-hole binary simulations: the mass ratio 10:1*. Phys. Rev., D79: 124006 (2009)
- [79] O. DREYER, B. KRISHNAN, D. SHOEMAKER, *et al.* *Introduction to Isolated Horizons in Numerical Relativity*. Phys. Rev. D, 67: 024018 (2003)
- [80] E. BERTI, V. CARDOSO, and C. M. WILL. *On gravitational-wave spectroscopy of massive black holes with the space interferometer LISA*. Phys. Rev. D, 73: 064030 (2006)
- [81] M. CAMPANELLI, C. O. LOUSTO, Y. ZLOCHOWER, *et al.* *Spin flips and precession in black-hole-binary mergers*. Phys. Rev., D75: 064030 (2007)
- [82] L. REZZOLLA, E. N. DORBAND, C. REISSWIG, *et al.* *Spin Diagrams for Equal-Mass Black-Hole Binaries with Aligned Spins*. Astrophysics, J679: 1422 (2008)
- [83] L. REZZOLLA, P. DIENER, E. N. DORBAND, *et al.* *The final spin from the coalescence of aligned-spin black-hole binaries*. Astrophys. J., 674: L29 (2008)
- [84] W. TICHY and P. MARRONETTI. *The final mass and spin of black hole mergers*. Phys. Rev., D78: 081501 (2008)
- [85] L. REZZOLLA, E. BARAUSSE, E. N. DORBAND, *et al.* *On the final spin from the coalescence of two black holes*. Phys. Rev., D78: 044002 (2008)
- [86] E. BARAUSSE and L. REZZOLLA. *Predicting the direction of the final spin from the coalescence of two black holes*. Astrophys. J. Lett., 704: L40 (2009)
- [87] L. BOYLE and M. KESDEN. *The spin expansion for binary black hole merger: new predictions and future directions*. Phys. Rev., D78: 024017 (2008)
- [88] M. KESDEN. *Can binary mergers produce maximally spinning black holes?* Phys.Rev., D78: 084030 (2008)
- [89] C. O. LOUSTO, M. CAMPANELLI, and Y. ZLOCHOWER. *Remnant Masses, Spins and Recoils from the Merger of Generic Black-Hole Binaries*. Class. Quant. Grav., 27: 114006 (2010)
- [90] J. A. GONZÁLEZ, U. SPERHAKE, B. BRÜGMANN, *et al.* *Total recoil: the maximum kick from nonspinning black-hole binary inspiral*. Phys. Rev. Lett., 98: 091101 (2007)
- [91] M. CAMPANELLI, C. O. LOUSTO, Y. ZLOCHOWER, *et al.* *Maximum gravitational recoil*. Phys. Rev. Lett., 98: 231102 (2007)
- [92] D. POLLNEY, C. REISSWIG, L. REZZOLLA, *et al.* *Recoil velocities from equal-*

- mass binary black-hole mergers: a systematic investigation of spin-orbit aligned configurations.* Phys. Rev., D76: 124002 (2007)
- [93] M. CAMPANELLI and C. O. LOUSTO. *Second order gauge invariant gravitational perturbations of a Kerr black hole.* Phys. Rev. D, 59: 124022 (1999). Gr-qc/9811019
- [94] J. G. BAKER, W. D. BOGGS, J. CENTRELLA, *et al.* *Modeling kicks from the merger of generic black-hole binaries.* Astrophys. J., 682: L29 (2008)
- [95] M. J. FITCHETT. *The influence of gravitational wave momentum losses on the centre of mass motion of a newtonian binary system.* MNRAS, 203: 1049 (1983)
- [96] A. BUONANNO, L. E. KIDDER, and L. LEHNER. *Estimating the final spin of a binary black hole coalescence.* Phys. Rev., D77: 026004 (2008)
- [97] L. BOYLE, M. KESDEN, and S. NISSANKE. *Binary black hole merger: symmetry and the spin expansion.* Phys. Rev. Lett., 100: 151101 (2008)
- [98] L. REZZOLLA, R. P. MACEDO, and J. L. JARAMILLO. *Understanding the 'anti-kick' in the merger of binary black holes.* Phys. Rev. Lett., 104: 221101 (2010)
- [99] L. REZZOLLA. *Modelling the final state from binary black-hole coalescences.* Class. Quant. Grav., 26: 094023 (2009)
- [100] M. CAMPANELLI, C. O. LOUSTO, and Y. ZLOCHOWER. *Last orbit of binary black holes.* Phys. Rev. D, 73: 061501(R) (2006). Gr-qc/0601091
- [101] S. HUSA, J. A. GONZÁLEZ, M. HANNAM, *et al.* *Reducing phase error in long numerical binary black hole evolutions with sixth order finite differencing.* Class. Quantum Grav., 25: 105006 (2008)
- [102] B. BRÜGMANN, W. TICHY, and N. JANSEN. *Numerical simulation of orbiting black holes.* Phys. Rev. Lett., 92: 211101 (2004)
- [103] R. COURANT, K. O. FRIEDRICHS, and H. LEWY. *On the partial difference equations of mathematical physics.* IBM journal of Research and Development, 11: 215 (1967)
- [104] G. B. COOK. *Initial data for numerical relativity.* Living Rev. Relativity, 3: 5 (2000)
- [105] J. W. YORK. *Gravitational degrees of freedom and the initial-value problem.* Phys. Rev. Lett., 26: 1656 (1971)
- [106] J. W. YORK. *Role of conformal three-geometry in the dynamics of gravitation.* Phys. Rev. Lett., 28: 1082 (1972)
- [107] J. W. YORK, JR. *Initial Data for Collisions of Black Holes and Other Gravitational Miscellany.* C. R. EVANS, L. S. FINN, and D. W. HOBILL (Eds.), Frontiers in Numerical Relativity. Cambridge University Press, Cambridge (1989)

- [108] J. M. BOWEN and J. W. YORK, JR. *Time-asymmetric initial data for black holes and black-hole collisions*. Phys. Rev. D, 21: 2047 (1980)
- [109] C. W. MISNER. *The method of images in geometrostatics*. Ann. Phys., 24: 102 (1963)
- [110] S. BRANDT and B. BRÜGMANN. *A simple construction of initial data for multiple black holes*. Phys. Rev. Lett., 78 (19): 3606 (1997)
- [111] C. MISNER and J. WHEELER. *Classical physics as geometry*. Ann. Phys. (N.Y.), 2: 525 (1957)
- [112] D. R. BRILL and R. W. LINDQUIST. *Interaction energy in geometrostatics*. Phys. Rev., 131: 471 (1963)
- [113] M. ANSORG, B. BRÜGMANN, and W. TICHY. *A single-domain spectral method for black hole puncture data*. Phys. Rev. D, 70: 064011 (2004)
- [114] B. J. KELLY, W. TICHY, M. CAMPANELLI, *et al.* *Black hole puncture initial data with realistic gravitational wave content*. Phys. Rev., D76: 024008 (2007)
- [115] B. J. KELLY, W. TICHY, Y. ZLOCHOWER, *et al.* *Post-Newtonian Initial Data with Waves: Progress in Evolution*. Class. Quant. Grav., 27: 114005 (2010)
- [116] G. LOVELACE. *Reducing spurious gravitational radiation in binary-black-hole simulations by using conformally curved initial data*. Class. Quant. Grav., 26: 114002 (2009)
- [117] M. HANNAM, S. HUSA, D. POLLNEY, *et al.* *Geometry and regularity of moving punctures*. Phys. Rev. Lett., 99: 241102 (2007)
- [118] M. HANNAM, S. HUSA, F. OHME, *et al.* *Wormholes and trumpets: the Schwarzschild spacetime for the moving-puncture generation*. Phys. Rev., D78: 064020 (2008)
- [119] J. D. IMMERMANN and T. W. BAUMGARTE. *Trumpet-puncture initial data for black holes*. Phys. Rev., D80: 061501 (2009)
- [120] M. HANNAM, S. HUSA, and N. O. MURCHADHA. *Bowen-York trumpet data and black-hole simulations*. Phys. Rev., D80: 124007 (2009)
- [121] J. GUNDERMANN. *The Hamiltonian Constraint for Puncture Initial Data*. Master's thesis, Friedrich-Schiller-Universität Jena, Theoretisch-Physikalisches Institut (2010)
- [122] P. C. PETERS. *Gravitational radiation and the motion of two point masses*. Phys. Rev., 136: B1224 (1964)
- [123] A. P. LIGHTMAN, W. H. PRESS, R. H. PRICE, *et al.* *Problem Book in Relativity and Gravitation*. Princeton University Press, Princeton, NJ (1975)
- [124] M. MAGGIORE. *Gravitational Waves. Vol. 1: Theory and Experiments*. Oxford

- University Press, Oxford (2007). ISBN ISBN-13: 978-0-19-857074-5
- [125] F. PRETORIUS and D. KHURANA. *Black hole mergers and unstable circular orbits*. *Class. Quant. Grav.*, 24: S83 (2007)
- [126] U. SPERHAKE, E. BERTI, V. CARDOSO, *et al.* *Eccentric binary black-hole mergers: The transition from inspiral to plunge in general relativity*. *Phys. Rev.*, D78: 064069 (2008)
- [127] I. HINDER, B. VAISHNAV, F. HERRMANN, *et al.* *Circularization and Final Spin in Eccentric Binary Black Hole Inspirals*. *Phys. Rev.*, D77: 081502 (2008)
- [128] J. HEALY, J. LEVIN, and D. SHOEMAKER. *Zoom-Whirl Orbits in Black Hole Binaries*. *Phys. Rev. Lett.*, 103: 131101 (2009)
- [129] R. GOLD and B. BRÜGMANN. *Radiation from low-momentum zoom-whirl orbits*. *Class. Quantum Grav.*, 27 (084035) (2009)
- [130] M. HANNAM, S. HUSA, J. G. BAKER, *et al.* *The Samurai Project: verifying the consistency of black-hole-binary waveforms for gravitational-wave detection*. *Phys. Rev. D*, 79: 084025 (2009)
- [131] E. K. PORTER and A. SESANA. *Eccentric Massive Black Hole Binaries in LISA I : The Detection Capabilities of Circular Templates* (2010)
- [132] J. S. KEY and N. J. CORNISH. *Characterizing Spinning Black Hole Binaries in Eccentric Orbits with LISA* (2010)
- [133] G. B. COOK. *Three-dimensional initial data for the collision of two black holes. II. Quasicircular orbits for equal-mass black holes*. *Phys. Rev. D*, 50: 5025 (1994). Gr-qc/9404043
- [134] T. W. BAUMGARTE. *Innermost stable circular orbit of binary black holes*. *Phys. Rev. D*, 62: 024018 (2000)
- [135] J. BAKER, M. CAMPANELLI, C. O. LOUSTO, *et al.* *Modeling gravitational radiation from coalescing binary black holes*. *Phys. Rev. D*, 65: 124012 (2002). Astro-ph/0202469
- [136] E. GOURGOULHON, P. GRANDCLÉMENT, and S. BONAZZOLA. *Binary black holes in circular orbits. I. A global spacetime approach*. *Phys. Rev. D*, 65: 044020 (2002)
- [137] P. GRANDCLÉMENT, E. GOURGOULHON, and S. BONAZZOLA. *Binary black holes in circular orbits. II. Numerical methods and first results*. *Phys. Rev. D*, 65: 044021 (2002)
- [138] W. TICHY, B. BRÜGMANN, and P. LAGUNA. *Gauge conditions for binary black hole puncture data based on an approximate helical Killing vector*. *Phys. Rev. D*, 68: 064008 (2003)
- [139] W. TICHY and B. BRÜGMANN. *Quasi-equilibrium binary black hole sequences*



- for puncture data derived from helical killing vector conditions. *Phys. Rev. D*, 69: 024006 (2004)
- [140] H. P. PFEIFFER, D. A. BROWN, L. E. KIDDER, *et al.* *Reducing orbital eccentricity in binary black hole simulations.* *Class. Quant. Grav.*, 24: S59 (2007)
- [141] A. BUONANNO, G. B. COOK, and F. PRETORIUS. *Inspiral, merger and ring-down of equal-mass black-hole binaries.* *Phys. Rev.*, D75: 124018 (2007)
- [142] S. HUSA, M. HANNAM, J. A. GONZÁLEZ, *et al.* *Reducing eccentricity in black-hole binary evolutions with initial parameters from post-Newtonian inspiral.* *Phys. Rev.*, D77: 044037 (2008)
- [143] J. G. BAKER, J. R. VAN METER, S. T. MCWILLIAMS, *et al.* *Consistency of post-Newtonian waveforms with numerical relativity.* *Phys. Rev. Lett.*, 99: 181101 (2007)
- [144] W. TICHY and P. MARRONETTI. *A Simple method to set up low eccentricity initial data for moving puncture simulations.* *Phys. Rev.*, D83: 024012 (2011)
- [145] B. BRÜGMANN, J. A. GONZÁLEZ, M. HANNAM, *et al.* *Exploring black hole superkicks.* *Phys. Rev.*, D77: 124047 (2008)
- [146] L. E. KIDDER. *Coalescing binary systems of compact objects to post<sup>5/2</sup>-Newtonian order. V. Spin effects.* *Phys. Rev. D*, 52: 821 (1995)
- [147] G. FAYE, L. BLANCHET, and A. BUONANNO. *Higher-order spin effects in the dynamics of compact binaries. I: Equations of motion.* *Phys. Rev.*, D74: 104033 (2006)
- [148] L. BLANCHET, A. BUONANNO, and G. FAYE. *Higher-order spin effects in the dynamics of compact binaries. II: Radiation field.* *Phys. Rev.*, D74: 104034 (2006)
- [149] T. DAMOUR, P. JARANOWSKI, and G. SCHAEFER. *Hamiltonian of two spinning compact bodies with next-to-leading order gravitational spin-orbit coupling.* *Phys. Rev.*, D77: 064032 (2008)
- [150] A. BUONANNO, Y. CHEN, and T. DAMOUR. *Transition from inspiral to plunge in precessing binaries of spinning black holes.* *Phys. Rev.*, D74: 104005 (2006)
- [151] G. SCHÄFER. *The gravitational quadrupole radiation-reaction force and the canonical formalism of ADM.* *Annals of Physics*, 161: 81 (1985)
- [152] T. BOGDANOVIC, C. S. REYNOLDS, and M. C. MILLER. *Alignment of the spins of supermassive black holes prior to coalescence.* *The Astrophysical Journal Letters*, 661 (2): L147 (2007)
- [153] V. KALOGERA. *Binary compact object inspiral: Detection expectations.* *pramana*, 64 (4): 673 (2004)
- [154] S. DAIN, C. O. LOUSTO, and Y. ZLOCHOWER. *Extra-Large Remnant Recoil*

- Velocities and Spins from Near- Extremal-Bowen-York-Spin Black-Hole Binaries.* Phys. Rev., D78: 024039 (2008)
- [155] G. LOVELACE, R. OWEN, H. P. PFEIFFER, *et al.* *Binary-black-hole initial data with nearly-extremal spins.* Phys. Rev., D78: 084017 (2008)
- [156] T. DAMOUR. *Coalescence of two spinning black holes: An effective one- body approach.* Phys. Rev. D, 64: 124013 (2001)
- [157] Numerical Relativity and Analytical Relativity collaboration, <https://www.ninja-project.org/doku.php?id=nrar:home>
- [158] T. DAMOUR and A. NAGAR. *Improved analytical description of inspiralling and coalescing black-hole binaries.* Phys. Rev. D, 79 (8): 081503 (2009)
- [159] A. BUONANNO, L. E. KIDDER, A. H. MROUE, *et al.* *Reducing orbital eccentricity in quasi-circular binary black-hole evolutions in presence of spins* (2010)
- [160] P. AMARO-SEOANE and L. SANTAMARIA. *Detection of IMBHs with ground-based gravitational wave observatories: A biography of a binary of black holes, from birth to death.* Astrophys. J., 722: 1197 (2010)
- [161] M. G. HAEHNELT. *Hierarchical build-up of galactic bulges and the merging rate of supermassive binary black holes.* Class. Quant. Grav., 20: S31 (2003)
- [162] P. AMARO-SEOANE, J. R. GAIR, M. FREITAG, *et al.* *Astrophysics, detection and science applications of intermediate- and extreme mass-ratio inspirals.* Class. Quant. Grav., 24: R113 (2007)
- [163] S. A. TEUKOLSKY. *Rotating black holes - separable wave equations for gravitational and electromagnetic perturbations.* Phys. Rev. Lett., 29: 1114 (1972)
- [164] S. A. TEUKOLSKY. *Perturbations of a rotating black hole. I. Fundamental equations for gravitational, electromagnetic, and neutrino-field perturbations.* Astrophys. J., 185: 635 (1973)
- [165] M. P. RYAN. *Teukolsky equation and Penrose wave equation.* Phys. Rev., D10: 1736 (1974)
- [166] C. O. LOUSTO, H. NAKANO, Y. ZLOCHOWER, *et al.* *Intermediate Mass Ratio Black Hole Binaries: Numerical Relativity meets Perturbation Theory.* Phys. Rev. Lett., 104: 211101 (2010)
- [167] F. HERRMANN, D. SHOEMAKER, and P. LAGUNA. *Unequal-mass binary black hole inspirals.* Classical and Quantum Gravity, 24: 33 (2006)
- [168] E. SCHNETTER. *Time Step Size Limitation Introduced by the BSSN Gamma Driver.* Class. Quant. Grav., 27: 167001 (2010)
- [169] M. ALCUBIERRE, B. BRÜGMANN, P. DIENER, *et al.* *Testing excision techniques for dynamical 3D black hole evolutions* (2004). gr-qc/0411137

- [170] Y. ZLOCHOWER, J. G. BAKER, M. CAMPANELLI, *et al.* *Accurate black hole evolutions by fourth-order numerical relativity.* Phys. Rev. D, 72: 024021 (2005)
- [171] P. DIENER, F. HERRMANN, D. POLLNEY, *et al.* *Accurate evolution of orbiting binary black holes.* Phys. Rev. Lett., 96 (12): 121101 (2006)
- [172] M. HANKE-BOURGEOIS. *Grundlagen der Numerischen Mathematik und des Wissenschaftlichen Rechnens.* Teubner Verlag, Wiesbaden (2006). ISBN 978-3835100909
- [173] B. BRÜGMANN. *Schwarzschild black hole as moving puncture in isotropic coordinates.* Gen. Rel. Grav., 41: 2131 (2009)
- [174] C. O. LOUSTO, H. NAKANO, Y. ZLOCHOWER, *et al.* *Intermediate-mass-ratio black hole binaries: Interweaving numerical and perturbative techniques.* Phys. Rev., D82: 104057 (2010)
- [175] C. O. LOUSTO and Y. ZLOCHOWER. *Modeling maximum astrophysical gravitational recoil velocities.* Phys. Rev., D83: 024003 (2011)
- [176] D. ALIC, L. REZZOLLA, I. HINDER, *et al.* *Dynamical damping terms for symmetry-seeking shift conditions.* Class. Quant. Grav., 27: 245023 (2010)
- [177] M. CAMPANELLI, C. O. LOUSTO, and Y. ZLOCHOWER. *Gravitational radiation from spinning-black-hole binaries: The orbital hang up.* Phys. Rev. D, 74: 041501 (2006). Gr-qc/0604012
- [178] M. HANNAM, S. HUSA, B. BRÜGMANN, *et al.* *Comparison between numerical-relativity and post-Newtonian waveforms from spinning binaries: the orbital hang-up case.* Phys. Rev., D78: 104007 (2008)
- [179] J. G. BAKER, W. D. BOGGS, J. CENTRELLA, *et al.* *Modeling kicks from the merger of non-precessing black-hole binaries.* Astrophys.J., 668: 1140 (2007)
- [180] P. MARRONETTI, W. TICHY, B. BRÜGMANN, *et al.* *High-spin binary black hole mergers.* Phys. Rev. D, 77: 064010 (2008)
- [181] J. A. GONZÁLEZ, M. D. HANNAM, U. SPERHAKE, *et al.* *Supermassive recoil velocities for binary black-hole mergers with antialigned spins.* Phys. Rev. Lett., 98 (23): 231101 (2007)
- [182] M. CAMPANELLI, C. O. LOUSTO, Y. ZLOCHOWER, *et al.* *Large merger recoils and spin flips from generic black-hole binaries.* Astrophys. J., 659: L5 (2007)
- [183] Y. ZLOCHOWER, M. CAMPANELLI, and C. O. LOUSTO. *Modeling Gravitational Recoil Using Numerical Relativity* (2010)
- [184] A. BUONANNO and T. DAMOUR. *Effective one-body approach to general relativistic two-body dynamics.* Phys. Rev. D, 59: 084006 (1999)
- [185] A. BUONANNO, Y. PAN, J. G. BAKER, *et al.* *Toward faithful templates for non-spinning binary black holes using the effective-one-body approach.* Phys.



- Rev., D76: 104049 (2007)
- [186] T. DAMOUR, A. NAGAR, E. N. DORBAND, *et al.* *Faithful Effective-One-Body waveforms of equal-mass coalescing black-hole binaries*. Phys. Rev., D77: 084017 (2008)
- [187] A. BUONANNO, Y. PAN, H. P. PFEIFFER, *et al.* *Effective-one-body waveforms calibrated to numerical relativity simulations: coalescence of non-spinning, equal-mass black holes*. Phys. Rev., D79: 124028 (2009)
- [188] Y. PAN, A. BUONANNO, L. T. BUCHMAN, *et al.* *Effective-one-body waveforms calibrated to numerical relativity simulations: coalescence of non-precessing, spinning, equal-mass black holes*. Phys. Rev., D81: 084041 (2010)
- [189] P. AJITH, S. BABAK, Y. CHEN, *et al.* *Phenomenological template family for black-hole coalescence waveforms*. Class. Quantum Grav., 24: S689 (2007)
- [190] P. AJITH. *Gravitational-wave data analysis using binary black-hole waveforms*. Class.Quant.Grav., 25: 114033 (2008)
- [191] P. AJITH, S. BABAK, Y. CHEN, *et al.* *A template bank for gravitational waveforms from coalescing binary black holes: I. non-spinning binaries*. Phys. Rev., D77: 104017 (2008)
- [192] M. A. SCHEEL, M. BOYLE, T. CHU, *et al.* *High-accuracy waveforms for binary black hole inspiral, merger, and ringdown*. Phys. Rev., D79: 024003 (2009)
- [193] D. POLLNEY, C. REISSWIG, E. SCHNETTER, *et al.* *High accuracy binary black hole simulations with an extended wave zone* (2009)
- [194] D. POLLNEY, C. REISSWIG, N. DORBAND, *et al.* *The Asymptotic Falloff of Local Waveform Measurements in Numerical Relativity*. Phys.Rev., D80: 121502 (2009)
- [195] C. REISSWIG, N. T. BISHOP, D. POLLNEY, *et al.* *Unambiguous determination of gravitational waveforms from binary black hole mergers*. Phys. Rev. Lett., 103: 221101 (2009)
- [196] M. HANNAM. *Status of black-hole-binary simulations for gravitational-wave detection*. Class. Quant. Grav., 26: 114001 (2009)
- [197] M. HANNAM, S. HUSA, F. OHME, *et al.* *Length requirements for numerical-relativity waveforms*. Phys. Rev., D82: 124052 (2010)
- [198] T. DAMOUR, B. R. IYER, and B. S. SATHYAPRAKASH. *A comparison of search templates for gravitational waves from binary inspiral*. Phys. Rev. D, 63: 044023 (2001). Erratum Phys. Rev. D72, 029902 (2005).
- [199] L. BLANCHET, T. DAMOUR, G. ESPOSITO-FARESE, *et al.* *Gravitational radiation from inspiralling compact binaries completed at the third post-Newtonian order*. Phys. Rev. Lett., 93: 091101 (2004)

- [200] E. RACINE, A. BUONANNO, and L. E. KIDDER. *Recoil velocity at 2PN order for spinning black hole binaries*. Phys.Rev., D80: 044010 (2009)
- [201] T. DAMOUR, B. R. IYER, and B. S. SATHYAPRAKASH. *A comparison of search templates for gravitational waves from binary inspiral: 3.5-pn update*. Phys. Rev., D66: 027502 (2002). Erratum Phys. Rev. D**72**, 029901 (2005).
- [202] T. DAMOUR, B. R. IYER, and B. S. SATHYAPRAKASH. *Erratum: Comparison of search templates for gravitational waves from binary inspiral: 3.5pn update*. Phys. Rev. D, 72 (2): 029901 (2005)
- [203] K. G. ARUN, B. R. IYER, B. S. SATHYAPRAKASH, *et al.* *Parameter estimation of inspiralling compact binaries using 3.5 post-Newtonian gravitational wave phasing: The non-spinning case*. Phys. Rev., D71: 084008 (2005)
- [204] L. BLANCHET, G. FAYE, B. R. IYER, *et al.* *The Third post-Newtonian gravitational wave polarisations and associated spherical harmonic modes for inspiralling compact binaries in quasi-circular orbits*. Class.Quant.Grav., 25: 165003 (2008)
- [205] K. ARUN, A. BUONANNO, G. FAYE, *et al.* *Higher-order spin effects in the amplitude and phase of gravitational waveforms emitted by inspiraling compact binaries: Ready-to-use gravitational waveforms*. Phys.Rev., D79: 104023 (2009)
- [206] A. BUONANNO, Y. CHEN, and M. VALLISNERI. *Detecting gravitational waves from precessing binaries of spinning compact objects: Adiabatic limit*. Phys. Rev. D, 67 (10): 104025 (2003)
- [207] R. STURANI, S. FISCHETTI, L. CADONATI, *et al.* *Complete phenomenological gravitational waveforms from spinning coalescing binaries*. J. Phys. Conf. Ser., 243: 012007 (2010)
- [208] R. STURANI, S. FISCHETTI, L. CADONATI, *et al.* *Phenomenological gravitational waveforms from spinning coalescing binaries* (2010)
- [209] [http://www.ligo.caltech.edu/~jzweizig/distribution/LSC\\_Data](http://www.ligo.caltech.edu/~jzweizig/distribution/LSC_Data)
- [210] T. A. APOSTOLATOS. *Search templates for gravitational waves from precessing, inspiraling binaries*. Phys. Rev. D, 52 (2): 605 (1995)
- [211] F. OHME. Private communication.
- [212] T. DAMOUR, P. JARANOWSKI, and G. SCHÄFER. *Dynamical invariants for general relativistic two-body systems at the third post-Newtonian approximation*. Phys. Rev. D, 62: 044024 (2000)
- [213] T. DAMOUR, P. JARANOWSKI, and G. SCHÄFER. *On the determination of the last stable orbit for circular general relativistic binaries at the third post-Newtonian approximation*. Phys. Rev. D, 62: 084011 (2000)
- [214] T. DAMOUR, P. JARANOWSKI, and G. SCHÄFER. *Poincaré invariance in the*

- ADM Hamiltonian approach to the general relativistic two-body problem.* Phys. Rev., D62: 021501 (2000). Erratum-ibid. 63, 029903, (2000)
- [215] T. DAMOUR, P. JARANOWSKI, and G. SCHÄFER. *Dimensional regularization of the gravitational interaction of point masses.* Phys. Lett. B, 513: 147 (2001)
- [216] A. BUONANNO and T. DAMOUR. *Transition from inspiral to plunge in binary black hole coalescences.* Phys. Rev. D, 62: 064015 (2000)
- [217] T. DAMOUR and G. SCHÄFER. *Higher-order relativistic periastron advances and binary pulsars.* Nuovo Cimento B, 101: 127 (1988)
- [218] L. BLANCHET and G. SCHÄFER. *Higher order gravitational radiation losses in binary systems.* Monthly Notices of the Royal Astronomical Society, 239: 845 (1989)
- [219] W. JUNKER and G. SCHÄFER. *Binary systems: higher order gravitational radiation damping and wave emission.* Monthly Notices of the Royal Astronomical Society, 254: 146 (1992)
- [220] M. CAMPANELLI, B. J. KELLY, and C. O. LOUSTO. *The Lazarus project II: Space-like extraction with the quasi-Kinnersley tetrad.* Phys. Rev. D, 73: 064005 (2006)
- [221] A. NEROZZI and O. ELBRACHT. *Using curvature invariants for wave extraction in numerical relativity* (2008). arXiv: 0811.1600 [gr-qc]



# Abbreviations and Notation

ADM	Arnowitt–Deser–Misner
BAM	Bi–functional Adaptive Mesh (name of the computer code)
BBH	binary black hole
BSSN	Baumgarte–Shapiro–Shibata–Nakamura
CFL	Courant–Friedrichs–Lewy
(C)TT	(conformal) transverse traceless
EH	EOB Hamiltonian
EOB	effective–one–body
FD	finite differencing
FF	fitting factor
FFI	fixed frequency integration
GW	gravitational wave(s)
LIGO	Laser Interferometer Gravitational Wave Observatory
LISA	Laser Interferometer Space Antenna
NLO	next–to–leading order
NINJA	Numerical Injection Analysis
NR	numerical relativity
NRAR	Numerical Relativity Analytical Relativity (collaboration)
PF	Padé resummed flux
PN	post–Newtonian
RHS	right hand side
RK4	fourth order Runge–Kutta
SO	spin–orbit
SS	spin–spin
TF	Taylor expanded flux
TH	Taylor Hamiltonian

$\bar{z}$	complex conjugate of a complex number $z$
$\Re(z)$	real part of a complex number $z$
$\Im(z)$	imaginary part of a complex number $z$
$\mu, \nu, \rho, \dots$	Greek indices take values $0 \dots 3$ .
$i, j, k, \dots$	Latin indices take values $1 \dots 3$ .
$T^{\alpha_1 \dots \alpha_k}_{\beta_1 \dots \beta_l}$	tensor of rank $\binom{k}{l}$
$T^{\alpha\beta}_{\gamma\rho} Q^{\rho\delta}_{\mu\nu} = \sum_{\rho} T^{\alpha\beta}_{\gamma\rho} Q^{\rho\delta}_{\mu\nu}$	Einstein summation convention: sum over repeated indices
$\partial_{\mu} T^{\alpha_1 \dots \alpha_k}_{\beta_1 \dots \beta_l}$	partial derivative along the coordinate $x^{\mu}$
$\nabla_{\mu} T^{\alpha_1 \dots \alpha_k}_{\beta_1 \dots \beta_l}$	covariant derivative along the coordinate $x^{\mu}$
$\mathcal{L}_{\vec{u}} T^{\alpha_1 \dots \alpha_k}_{\beta_1 \dots \beta_l}$	Lie derivative along the vector $\vec{u}$

# A Hamiltonian and Flux Function for Initial Data

In this appendix, the equations needed in the algorithm for producing initial data, which is presented in Sec. 3.5, are recalled. In the following formulas, the gravitational constant and the velocity of light are set to one, which is consistent with the system of units used for numerical simulations in BAM.

Here, we assume two point particles with masses  $M_1$  and  $M_2$ , possessing spins  $\vec{S}_1$  and  $\vec{S}_2$  and located at positions  $\vec{X}_1$  and  $\vec{X}_2$ , respectively. The analysis is restricted to the center-of-mass frame with zero total momentum, such that the individual momenta are pointing in opposite directions but have equal magnitude,  $\vec{P}_1 = -\vec{P}_2 =: \vec{P}$ , and we use  $\vec{X} = (\vec{X}_1 - \vec{X}_2)$ . The system's equations of motion in a Hamiltonian formulation read

$$\frac{d\vec{X}}{dt} = \left\{ \vec{X}, H \right\} = \frac{\partial H}{\partial \vec{P}}, \quad (\text{A.1})$$

$$\frac{d\vec{P}}{dt} = \left\{ \vec{P}, H \right\} + \vec{F} = -\frac{\partial H}{\partial \vec{X}} + \vec{F}, \quad (\text{A.2})$$

$$\frac{d\vec{S}_a}{dt} = \left\{ \vec{S}_a, H \right\} = \frac{\partial H}{\partial \vec{S}_a} \times \vec{S}_a \quad (a = 1, 2). \quad (\text{A.3})$$

$\vec{F}$  is a non-conservative force added in order to describe radiation reaction effects in the system.

We introduce reduced coordinates  $\vec{q} = \vec{X}/M$  and  $\vec{p} = \vec{P}/\mu$ , where  $M = M_1 + M_2$  and  $\mu = M_1 M_2 / M$ . Additionally, we have  $q = |\vec{q}|$ ,  $\vec{n} = \vec{q}/q$  and  $\nu = \mu/M$ .

Then the Taylor expanded orbital Hamiltonian reads [212–215]

$$H_{\text{Taylor}}^0(\vec{q}, \vec{p}) = M + \mu \left[ \hat{H}_{\text{N}}(\vec{q}, \vec{p}) + \hat{H}_{1\text{PN}}(\vec{q}, \vec{p}) + \hat{H}_{2\text{PN}}(\vec{q}, \vec{p}) + \hat{H}_{3\text{PN}}(\vec{q}, \vec{p}) \right], \quad (\text{A.4})$$

with

$$\hat{H}_N(\vec{q}, \vec{p}) = \frac{(\vec{p})^2}{2} - \frac{1}{q}, \quad (\text{A.5})$$

$$\hat{H}_{1\text{PN}}(\vec{q}, \vec{p}) = \frac{1}{8}(3\nu - 1)(\vec{p})^4 - \frac{1}{2q} \left[ (3 + \nu)(\vec{p})^2 + \nu(\vec{n}\vec{p})^2 \right] + \frac{1}{2q^2}, \quad (\text{A.6})$$

$$\begin{aligned} \hat{H}_{2\text{PN}}(\vec{q}, \vec{p}) &= \frac{1}{16} (1 - 5\nu + 5\nu^2) (\vec{p})^6 \\ &+ \frac{1}{8q} \left[ (5 - 20\nu - 3\nu^2) (\vec{p})^4 - 2\nu^2(\vec{n}\vec{p})^2(\vec{p})^2 - 3\nu^2(\vec{n}\vec{p})^4 \right] \\ &+ \frac{1}{2q^2} \left[ 3\nu(\vec{n}\vec{p})^2 + (5 + 8\nu)(\vec{p})^2 \right] - \frac{1}{4q^3} (1 + 3\nu), \end{aligned} \quad (\text{A.7})$$

$$\begin{aligned} \hat{H}_{3\text{PN}}(\vec{q}, \vec{p}) &= \frac{1}{128} (-5 + 35\nu - 70\nu^2 + 35\nu^3) (\vec{p})^8 \\ &+ \frac{1}{16q} \left[ (-7 + 42\nu - 53\nu^2 - 5\nu^3)(\vec{p})^6 \right. \\ &\left. + (2 - 3\nu)\nu^2(\vec{n}\vec{p})^2(\vec{p})^4 + 3(1 - \nu)\nu^2(\vec{n}\vec{p})^4(\vec{p})^2 - 5\nu^3(\vec{n}\vec{p})^6 \right] \\ &+ \frac{1}{q^2} \left[ \frac{1}{16}(-27 + 136\nu + 109\nu^2)(\vec{p})^4 + \frac{1}{16}(17 + 30\nu)\nu(\vec{n}\vec{p})^2(\vec{p})^2 \right. \\ &\left. + \frac{1}{12}(5 + 43\nu)\nu(\vec{n}\vec{p})^4 \right] \\ &+ \frac{1}{q^3} \left\{ \left[ -\frac{25}{8} + \left( \frac{1}{64}\pi^2 - \frac{335}{48} \right) \nu - \frac{23}{8}\nu^2 \right] (\vec{p})^2 \right. \\ &\left. + \left( -\frac{85}{16} - \frac{3}{64}\pi^2 - \frac{7}{4}\nu \right) \nu(\vec{n}\vec{p})^2 \right\} + \frac{1}{q^4} \left[ \frac{1}{8} + \left( \frac{109}{12} - \frac{21}{32}\pi^2 \right) \nu \right]. \end{aligned} \quad (\text{A.8})$$

The EOB formalism works with different coordinates and therefore, primed variables will be used in the EOB Hamiltonian. It is then given by the expression [213, 216]

$$H_{\text{EOB}}^0(\vec{q}', \vec{p}') = M \sqrt{1 + 2\nu \left( \frac{H_{\text{eff}}(\vec{q}', \vec{p}') - \mu}{\mu} \right)}, \quad (\text{A.9})$$



with

$$H_{\text{eff}}(\vec{q}', \vec{p}') = \mu \sqrt{A(q') \left[ 1 + (\vec{p}')^2 + \left( \frac{A(q')}{D(q')} - 1 \right) (\vec{n}' \vec{p}')^2 + \frac{z_3}{q'} (\vec{n}' \vec{p}')^4 \right]}, \quad (\text{A.10})$$

where  $A(q')$  is the Padé-resummed function

$$A(q') = \frac{q'^3(8 - 2\nu) + q'^2(a_4 + 8\nu - 16)}{q'^3(8 - 2\nu) + q'^2(a_4 + 4\nu) + q'(2a_4 + 8\nu) + 4(a_4 + \nu^2)}, \quad (\text{A.11})$$

and the remaining quantities are

$$\begin{aligned} a_4 &= \left( \frac{94}{3} - \frac{41}{32} \pi^2 \right) \nu, \\ D(q') &= 1 - \frac{6\nu}{q'^2} + (3\nu - 26) \frac{\nu}{q'^3}, \\ z_3 &= \frac{3}{4} (4 - \nu) \nu. \end{aligned} \quad (\text{A.12})$$

As before we made use of reduced variables  $\vec{q}'$  and  $\vec{p}'$  which are constructed similarly to  $\vec{q}$  and  $\vec{p}$  above.

The spin part is considered to leading order only. These terms can be separated into spin-orbit (SO) and spin-spin (SS) interactions, see for example [150, 217]. The expressions are

$$H_{\text{SO}} = 2 \frac{\vec{S}_{\text{eff}} \cdot \vec{L}}{R^3}, \quad (\text{A.13})$$

$$\vec{S}_{\text{eff}} = \left( 1 + \frac{3 M_2}{4 M_1} \right) \vec{S}_1 + \left( 1 + \frac{3 M_1}{4 M_2} \right) \vec{S}_2,$$

$$H_{\text{SS}} = H_{S_1 S_1} + H_{S_1 S_2} + H_{S_2 S_2}, \quad (\text{A.14})$$

$$H_{S_1 S_2} = \frac{1}{R^3} \left[ 3 \left( \vec{S}_1 \cdot \vec{n} \right) \left( \vec{S}_2 \cdot \vec{n} \right) - \left( \vec{S}_1 \cdot \vec{S}_2 \right) \right],$$

$$H_{S_1 S_1} = \frac{1}{2R^3} \left[ 3 \left( \vec{S}_1 \cdot \vec{n} \right) \left( \vec{S}_1 \cdot \vec{n} \right) - \left( \vec{S}_1 \cdot \vec{S}_1 \right) \right] \frac{M_2}{M_1},$$

$$H_{S_2 S_2} = H_{S_1 S_1} (1 \rightleftharpoons 2).$$

Here,  $\vec{L} = \vec{X} \times \vec{P}$  is the orbital angular momentum. The Newton-Wigner spin

supplementary condition is assumed, which provides the notion of the spin vector.

We do not perform a canonical transformation of the coordinates in the spin parts, but assume Eqns. (A.13)–(A.14) to hold in ADMTT as well as EOB coordinates.

What is left to be specified is the non-conservative force,

$$\vec{F} = \frac{1}{\omega |\vec{L}|} \frac{dE}{dt} \vec{P} + \frac{8}{15} \nu^2 \frac{v_\omega^8}{\vec{L}^2 R} \left\{ \left( 61 + 48 \frac{M_2}{M_1} \right) \vec{P} \cdot \vec{S}_1 + \left( 61 + 48 \frac{M_1}{M_2} \right) \vec{P} \cdot \vec{S}_2 \right\} \vec{L}, \quad (\text{A.15})$$

with invariant velocity parameter  $v_\omega = (M\omega)^{1/3}$  using the orbital frequency  $\omega$ .  $dE/dt$  is the energy–flux function of circularly orbiting masses [150, 218, 219], which is why Eq. (A.15) is valid for (quasi-)circular orbits, only. In particular, its standard form (up to 3.5PN order) does not account for any eccentricity parameter, and we have

$$\begin{aligned} \frac{dE}{dt} = & -\frac{32}{5} \nu^2 v_\omega^{10} \left\{ 1 + f_2(\nu) v_\omega^2 + [f_3(\nu) + f_{3\text{SO}}] v_\omega^3 \right. \\ & \left. + [f_4(\nu) + f_{4\text{SS}}] v_\omega^4 + f_5(\nu) v_\omega^5 + f_6(\nu) v_\omega^6 + f_{l6} v_\omega^6 \ln(4v_\omega) + f_7(\nu) v_\omega^7 \right\}. \quad (\text{A.16}) \end{aligned}$$

The expansion coefficients read

$$\begin{aligned} f_2(\nu) &= -\frac{1247}{336} - \frac{35}{12} \nu, & f_3(\nu) &= 4\pi, \\ f_4(\nu) &= -\frac{44\,711}{9072} + \frac{9271}{504} \nu + \frac{65}{18} \nu^2, & f_5(\nu) &= -\left( \frac{8191}{672} + \frac{583}{24} \nu \right) \pi, \\ f_6(\nu) &= \frac{6\,643\,739\,519}{69\,854\,400} + \frac{16}{3} \pi^2 - \frac{1712}{105} \gamma_{\text{E}} + \left( -\frac{134\,543}{7776} + \frac{41}{48} \pi^2 \right) \nu - \frac{94\,403}{3024} \nu^2 - \frac{775}{324} \nu^3, \\ f_{l6} &= -\frac{1712}{105}, & f_7(\nu) &= \left( -\frac{16\,285}{504} + \frac{214\,745}{1728} \nu + \frac{193\,385}{3024} \nu^2 \right) \pi, \\ f_{3\text{SO}} &= -\left( \frac{11}{4} + \frac{5 M_2}{4 M_1} \right) \frac{\hat{\vec{L}} \cdot \vec{S}_1}{M^2} - \left( \frac{11}{4} + \frac{5 M_1}{4 M_2} \right) \frac{\hat{\vec{L}} \cdot \vec{S}_2}{M^2}, \\ f_{4\text{SS}} &= \frac{\nu}{48 M_1^2 M_2^2} \left[ 289 (\hat{\vec{L}} \cdot \vec{S}_1) (\hat{\vec{L}} \cdot \vec{S}_2) - 103 (\vec{S}_1 \cdot \vec{S}_2) \right] + \mathcal{O}(\vec{S}_1^2) + \mathcal{O}(\vec{S}_2^2), \quad (\text{A.17}) \end{aligned}$$

where  $\gamma_E = 0.577215\dots$  is Euler's gamma and  $\hat{L}$  is the unit vector in the direction of  $\vec{L}$ .

The energy difference between neighboring spherical orbits can be approximated by [150]

$$\left[ \left( \frac{dE}{dR} \right)_{\text{sph}} \right]_0 \approx - \frac{[(\frac{\partial H}{\partial L})]_0 [(\frac{\partial^2 H}{\partial R^2})]_0}{[(\frac{\partial^2 H}{\partial R \partial L})]_0}. \quad (\text{A.18})$$

The primed and unprimed variables used above are related to each other by a canonical transformation. The generating function is known explicitly to 3PN order and is given by [184, 213]

$$\tilde{G}(\vec{q}, \vec{p}') = q^i p'_i + G(\vec{q}, \vec{p}'), \quad (\text{A.19})$$

$$G(\vec{q}, \vec{p}') = \frac{1}{c^2} G_{1\text{PN}}(\vec{q}, \vec{p}') + \frac{1}{c^4} G_{2\text{PN}}(\vec{q}, \vec{p}') + \frac{1}{c^6} G_{3\text{PN}}(\vec{q}, \vec{p}'), \quad (\text{A.20})$$

and the different PN orders read

$$G_{1\text{PN}}(\vec{q}, \vec{p}') = (\vec{q} \cdot \vec{p}') \left( a_1 \vec{p}'^2 + \frac{a_2}{q} \right), \quad (\text{A.21})$$

$$G_{2\text{PN}}(\vec{q}, \vec{p}') = (\vec{q} \cdot \vec{p}') \left[ b_1 \vec{p}'^4 + \frac{1}{q} (b_2 \vec{p}'^2 + b_3 (\vec{n} \cdot \vec{p}')^2) + \frac{b_4}{q^2} \right], \quad (\text{A.22})$$

$$G_{3\text{PN}}(\vec{q}, \vec{p}') = (\vec{q} \cdot \vec{p}') \left[ c_1 \vec{p}'^6 + \frac{1}{q} (c_2 \vec{p}'^4 + c_3 \vec{p}'^2 (\vec{n} \cdot \vec{p}')^2 + c_4 (\vec{n} \cdot \vec{p}')^4) \right. \\ \left. + \frac{1}{q^2} (c_5 \vec{p}'^2 + c_6 (\vec{n} \cdot \vec{p}')^2) + \frac{c_7}{q^3} \right]. \quad (\text{A.23})$$

The coefficients are

$$\begin{aligned}
a_1 &= -\frac{\nu}{2}, & c_1 &= -\frac{1}{16}(1 + 3\nu + 5\nu^2)\nu, \\
a_2 &= 1 + \frac{\nu}{2}, & c_2 &= -\frac{1}{16}(1 + 2\nu - 11\nu^2)\nu, \\
b_1 &= \frac{1}{8}(\nu + 3\nu^2), & c_3 &= -\frac{1}{24}(12 + 48\nu + 23\nu^2)\nu, \\
b_2 &= \frac{1}{8}(2\nu - 5\nu^2), & c_4 &= \frac{1}{16}(24 + 7\nu)\nu^2, \\
b_3 &= \frac{1}{8}(8\nu + 3\nu^2), & c_5 &= -\frac{1}{16}(13 - 16\nu + 6\nu^2)\nu, \\
b_4 &= \frac{1}{4}(1 - 7\nu + \nu^2), & c_6 &= -\frac{1}{48}(115 + 116\nu - 26\nu^2)\nu, \\
& & c_7 &= -\left(\frac{1}{64}\pi^2 + \frac{155}{24}\right)\nu + \frac{3}{8}\nu^2 + \frac{1}{8}\nu^3.
\end{aligned} \tag{A.24}$$

The transformation EOB $\rightarrow$ ADMTT is

$$q^i = q'^i - \frac{\partial G(\vec{q}, \vec{p}')}{\partial p'_i} \quad p_i = p'_i + \frac{\partial G(\vec{q}, \vec{p}')}{\partial q^i}. \tag{A.25}$$

This implicit rule can be solved numerically. The backward transformation ADMTT $\rightarrow$ EOB can be obtained by a rearrangement of Eq. (A.25).

# B Tetrad Construction for Gravitational Wave Extraction

In the TT gauge and far away from the gravitational sources so that we are approximately in flat space, the Weyl scalar  $\Psi_4$  corresponds to outgoing plane waves. It is therefore used to calculate the amount of radiation in a numerical simulation. Its definition, Eq. (2.23), involves the Weyl tensor  $C_{\alpha\beta\gamma\delta}$  and a null tetrad composed of the vectors  $\{l^\mu, k^\mu, m^\mu, \bar{m}^\mu\}$  where  $\bar{m}^\mu$  is the complex conjugate of  $m^\mu$ . The null tetrad can be obtained from an orthonormal tetrad  $\vec{e}_{(a)}$  (here,  $a$  counts the vectors in the tetrad) by setting

$$\begin{aligned} l^\mu &= \frac{1}{\sqrt{2}} \left( e_{(0)}^\mu + e_{(1)}^\mu \right), & k^\mu &= \frac{1}{\sqrt{2}} \left( e_{(0)}^\mu - e_{(1)}^\mu \right), \\ m^\mu &= \frac{1}{\sqrt{2}} \left( e_{(2)}^\mu + ie_{(3)}^\mu \right), & \bar{m}^\mu &= \frac{1}{\sqrt{2}} \left( e_{(2)}^\mu - ie_{(3)}^\mu \right). \end{aligned}$$

The BAM code uses  $e_{(0)}^\mu = n^\mu$  (the unit normal vector to the spatial hypersurfaces,  $n^\mu = (1/\alpha, -\beta^i/\alpha)$  in the coordinate system of Sec. 2.1),  $e_{(1)}^\mu = (0, v^i)$ ,  $e_{(2)}^\mu = (0, u^i)$  and  $e_{(3)}^\mu = (0, w^i)$ . The spatial vectors  $v^i, u^i$  and  $w^i$  are obtained by a Gram–Schmidt orthonormalization of the vectors  $v^{i1} = (x, y, z)$ ,  $u^{i1} = (-y, x, 0)$  and  $w^{i1} = \gamma^{ia}\epsilon_{abc}u^av^b$  with  $\gamma^{ia}$  the spatial 3–metric. The tetrad then takes the explicit form

$$l^0 = \frac{1}{\sqrt{2}\alpha}, \quad l^i = \frac{1}{\sqrt{2}} \left( \frac{-\beta^i}{\alpha} + v^i \right), \quad (\text{B.1})$$

$$k^0 = \frac{1}{\sqrt{2}\alpha}, \quad k^i = \frac{1}{\sqrt{2}} \left( \frac{-\beta^i}{\alpha} - v^i \right), \quad (\text{B.2})$$

$$m^0 = 0, \quad m^i = \frac{1}{\sqrt{2}} (u^i + iw^i), \quad (\text{B.3})$$

$$\bar{m}^0 = 0, \quad \bar{m}^i = \frac{1}{\sqrt{2}} (u^i - iw^i). \quad (\text{B.4})$$

In flat space, the three vectors  $v'^i, u'^i$  and  $w'^i$  are the standard spherical basis vectors  $e_r, e_\phi$  and  $e_\theta$ . Therefore, the null tetrad reduces to the standard flat space tetrad asymptotically far away from the sources. An alternative choice is the quasi-Kinnersley tetrad [220, 221].

# C Gravitational Wave Modes in Bitant Symmetry

Because of the symmetries of  $\Psi_4$  and the spin-weighted spherical harmonics used as basis functions it is possible to derive a relation between the multipoles  $\Psi_4^{lm}$  and  $\Psi_4^{l,-m}$ . We will assume that the (initial) orbital plane is the plane  $z = 0$ , and we use standard spherical coordinates  $r, \theta, \phi$  with  $r \geq 0, \theta \in [0, \pi]$  and  $\phi \in [0, 2\pi)$ . The argument is the same as the one given in Sec. IIIA of [61] where they derive how to compute the  $l = 2, m = 2$  mode in bitant symmetry (that is, reflection symmetry across the orbital plane).

The multipole  $\Psi_4^{lm}$  is computed using Eq. (2.26),

$$\begin{aligned} \Psi_4^{lm} &= ({}_{-2}Y_{lm}, \Psi_4) = \int_0^{2\pi} \int_0^\pi \sin \theta \, d\theta \, d\varphi \, \overline{{}_{-2}Y_{lm}(\theta, \phi)} \Psi_4(\theta, \phi) \\ &= \int_0^{2\pi} \int_0^{\pi/2} \sin \theta \, d\theta \, d\varphi \, \overline{{}_{-2}Y_{lm}(\theta, \phi)} \Psi_4(\theta, \phi) + \underbrace{\int_0^{2\pi} \int_{\pi/2}^\pi \sin \theta \, d\theta \, d\varphi \, \overline{{}_{-2}Y_{lm}(\theta, \phi)} \Psi_4(\theta, \phi)}_{(*)}. \end{aligned} \tag{C.1}$$

The second summand can be further transformed by setting  $\theta = \pi - \theta'$ ,

$$(*) = \int_0^{2\pi} \int_0^{\pi/2} \sin \theta' \, d\theta' \, d\varphi \, \overline{{}_{-2}Y_{lm}(\pi - \theta', \phi)} \Psi_4(\pi - \theta', \phi). \tag{C.2}$$

$\Psi_4$  is a pseudo scalar and transforms into its complex conjugate under reflections at  $z = 0$ ,  $\Psi_4(\pi - \theta', \phi) = \overline{\Psi_4(\theta', \phi)}$ . From the definition of the spin-weighted spherical harmonics we see that  ${}_{-2}Y_{lm}$  under a reflection transforms as  $\overline{{}_{-2}Y_{lm}(\pi - \theta', \phi)} =$

$(-1)^l {}_{-2}Y_{l,-m}(\theta', \phi)$ . Plugging this relation into Eq. (C.2), we obtain

$$(*) = \int_0^{2\pi} \int_0^{\pi/2} \sin \theta' d\theta' d\varphi (-1)^l {}_{-2}Y_{l,-m}(\theta', \phi) \overline{\Psi_4(\theta', \phi)}, \quad (\text{C.3})$$

and Eq. (C.1) can be written as

$$\Psi_4^{lm} = \int_0^{2\pi} \int_0^{\pi/2} \sin \theta d\theta d\varphi \left[ \overline{{}_{-2}Y_{lm}(\theta, \phi)} \Psi_4(\theta, \phi) + (-1)^l {}_{-2}Y_{l,-m}(\theta, \phi) \overline{\Psi_4(\theta, \phi)} \right]. \quad (\text{C.4})$$

Following the same argument, we find

$$\begin{aligned} \Psi_4^{l,-m} &= \int_0^{2\pi} \int_0^{\pi/2} \sin \theta d\theta d\varphi \left[ \overline{{}_{-2}Y_{2,-m}(\theta, \phi)} \Psi_4(\theta, \phi) + (-1)^l {}_{-2}Y_{2,m}(\theta, \phi) \overline{\Psi_4(\theta, \phi)} \right] \\ &= \int_0^{2\pi} \int_0^{\pi/2} \sin \theta d\theta d\varphi \left[ \overline{(-1)^l {}_{-2}Y_{2,m}(\theta, \phi) \Psi_4(\theta, \phi) + {}_{-2}Y_{2,-m}(\theta, \phi) \overline{\Psi_4(\theta, \phi)}} \right] \\ &= (-1)^l \int_0^{2\pi} \int_0^{\pi/2} \sin \theta d\theta d\varphi \left[ \overline{{}_{-2}Y_{2,m}(\theta, \phi) \Psi_4(\theta, \phi) + (-1)^l {}_{-2}Y_{2,-m}(\theta, \phi) \overline{\Psi_4(\theta, \phi)}} \right] \end{aligned} \quad (\text{C.5})$$

and comparing the last line of Eq. (C.5) to Eq. (C.4) we find

$$\Psi_4^{l,-m} = (-1)^l \overline{\Psi_4^{l,m}}. \quad (\text{C.6})$$

Therefore, properties of the modes with negative values of  $m$  can be completely derived from those with  $m$  sign reversed and the same value of  $l$ .



# Ehrenwörtliche Erklärung

Ich erkläre hiermit ehrenwörtlich, dass ich die vorliegende Arbeit selbständig, ohne unzulässige Hilfe Dritter und ohne Benutzung anderer als der angegebenen Hilfsmittel und Literatur angefertigt habe. Die aus anderen Quellen direkt oder indirekt übernommenen Daten und Konzepte sind unter Angabe der Quelle gekennzeichnet. Bei der Auswahl und Auswertung haben mir die nachstehend aufgeführten Personen in der jeweils beschriebenen Weise unentgeltlich geholfen:

1. Prof. Brüggemann — beratend.

Weitere Personen waren an der inhaltlich-materiellen Erstellung der vorliegenden Arbeit nicht beteiligt. Insbesondere habe ich hierfür nicht die entgeltliche Hilfe von Vermittlungs- bzw. Beratungsdiensten (Promotionsberater oder andere Personen) in Anspruch genommen. Niemand hat von mir unmittelbar oder mittelbar geldwerte Leistungen für Arbeiten erhalten, die im Zusammenhang mit dem Inhalt der vorgelegten Dissertation stehen.

Die Arbeit wurde bisher weder im In- noch im Ausland in gleicher oder ähnlicher Form einer anderen Prüfungsbehörde vorgelegt.

Die geltende Promotionsordnung der Physikalisch-Astronomischen Fakultät ist mir bekannt.

Ich versichere ehrenwörtlich, dass ich nach bestem Wissen die reine Wahrheit gesagt und nichts verschwiegen habe.

Jena, den 10.04.2011

Doreen Müller



# Zusammenfassung

In dieser Arbeit wurde eine Methode vorgestellt, mit der Anfangsparameter, die zu quasi-zirkulären Orbits mit sehr kleinen Exzentrizitäten führen, erzeugt werden können. Dieser analytische Algorithmus wurde für Systeme mit gleichen und ungleichen Massen, jedoch ohne Spins getestet, sowie auch für Systeme mit gleichen Massen und nicht-verschwindenden Spins, die entlang des Orbitaldrehimpulses zeigen. Für Massenverhältnisse, die in der Nähe von eins liegen, wurden erwartungsgemäß geringere Exzentrizitäten bei Verwendung eines taylorentwickelten Hamiltonoperators erzielt, für alle anderen Konfigurationen lieferte der verwendete EOB-Hamiltonoperator kleinere Werte der Exzentrizität. Für ein Binärsystem mit dem Massenverhältnis 2:1 und verschwindendem Gesamtspin, jedoch nicht verschwindenden Einzelspins, für das NRAR-Projekt konnte mit dieser Methode eine Exzentrizität erreicht werden, die ohne weiteres Regeln den NRAR-Spezifikationen entsprach.

Des Weiteren wurde untersucht, wie Binärsysteme mit ungleichen Massen in der numerischen Relativitätstheorie stabil evolviert werden können. Seit einiger Zeit schon war bekannt, dass die beliebte “Gamma driver”-Bedingung für den Shiftvektor für bestimmte numerische Gitter in Kombination mit bestimmten Werten des Dämpfungsp Parameters zu Instabilitäten führt. Dies steht in direktem Zusammenhang mit Instabilitäten, die bei Simulationen mit Massenverhältnissen, die wesentlich von eins abweichen, auftreten. Dies ist u. a. dem Umstand geschuldet, dass der Dämpfungsp Parameter in der verwendeten Shiftbedingung invers proportional zur (lokalen) Masse auf dem Gitter ist. Eine Methode wurde vorgestellt, die durch die Verwendung eines auf dem numerischen Gitter variierenden Dämpfungsp Parameters das Stabilitätsproblem löst. Mit dieser Methode traten wesentlich kleinere Phasen- und Amplitudenfehler in den extrahierten Gravitationswellen auf, was gerade für die Evolution von Systemen mit hohem Massenverhältnis von großem Vorteil ist, da solche Simulationen naturgemäß einen hohen Verbrauch an numerischen Ressourcen haben.

Es wurde außerdem untersucht, wie die Genauigkeit extrahierter Wellen erhöht wer-

den kann, obwohl die numerische Rechenleistung kaum steigt. Dies wurde durch Variationen des numerischen Gitters erreicht. Die gewonnenen hochgenauen Gravitationswellen können für die Kalibrierung von Gravitationswellentemplates benutzt werden. Es wurde kurz vorgestellt, wie phänomenologische Templates erstellt werden, die erstmals auch Spin modellieren, und dass diese Templates für die Detektion von Systemen mit allgemeinen Spins oder ungleichen Massen geeignet sind.